Available online at www.sciencedirect.com
ScienceDirect
Progress in Materials Science 53 (2008) 323–420
Progress in Materials Science
www.elsevier.com/locate/pmatsci

Giant magnetoimpedance materials: Fundamentals and applications

Manh-Huong Phan *, Hua-Xin Peng *

Advanced Composites Centre for Innovation and Science (ACCIS), University of Bristol,
Queen's Building, University Walk, Bristol BS8 1TR, United Kingdom

Received 1 April 2007; accepted 1 May 2007

Abstract

Since the discovery of the magnetoimpedance (MI) effect just over a decade ago, international research interest into the giant magnetoimpedance (GMI) effect has been growing. This article aims to provide a comprehensive summary of the GMI topic, encompassing fundamental understanding of the GMI phenomena, the processing and properties of GMI materials and the design and application of GMI-based magnetic sensors. The paper starts with the definition of GMI and an assessment of the current theoretical understanding of the frequency dependence of GMI. Then a detailed description of processing methods for the production of amorphous and nanocrystalline GMI materials in the form of wires, ribbons and thin films is given, with an examination of the advantages and disadvantages of each technique. Properties of existing GMI materials including magnetic, mechanical, electrical and chemical properties are described, and a correlation between domain structures and magnetic properties is established. The influences of measuring and processing parameters on the GMI effect are systematically analysed and the underlying physical origins of hysteretic and asymmetric phenomena of GMI are explained. This enables the selection of optimal conditions to design high-performance GMI-based sensors. After discussing the material selection criteria, a range of candidate materials are evaluated and nominated for the design of GMI-based sensors. Finally, a variety of potential applications of GMI-based magnetic sensors are presented with an outlook of future research development in this field.

© 2007 Elsevier Ltd. All rights reserved.

---

* Corresponding authors. Tel.: +44 (0) 117 92 87697; fax: +44 (0) 117 92 72771.
E-mail addresses: M.H.Phan@bristol.ac.uk (M.-H. Phan), H.X.Peng@bristol.ac.uk (H.-X. Peng).

0079-6425/$ - see front matter © 2007 Elsevier Ltd. All rights reserved.
doi:10.1016/j.pmatsci.2007.05.003

Contents

1. Introduction

Magnetic sensors play an essential role in modern technology. They are widely used in nearly all engineering and industrial sectors, such as high-density magnetic recording, navigation, military and security, target detection and tracking, antitheft systems, non-destructive testing, magnetic marking and labelling, geomagnetic measurements, space research, measurements of magnetic fields onboard spacecraft and biomagnetic measurements in the human body [1–3].

A wide range of magnetic sensors, such as induction sensors, fluxgate sensors, Hall-effect magnetic sensors, magneto-optical sensors, giant magnetoresistive (GMR) sensors, resonance magnetometers, and superconducting quantum interference device (SQUID) gradiometers, are now available [3]. A magnetic sensor directly converts the magnetic field into a voltage or resistance with, at most, a dc current supply, and the field sensitivity of a magnetic sensor plays a key role in determining its operating regime and potential applications. For instance, SQUID gradiometers with a high sensitivity of 10^{-10}–10^{-4} Oe have been used for measuring field gradients or differences due to permanent dipole magnets in major applications of brain function mapping and magnetic anomaly detection. Induction, fluxgate and GMR sensors with a medium sensitivity of 10^{-6}–10^{2} Oe have been used for measuring perturbations in the magnitudes and/or direction of Earth's field due to induced or permanent dipoles in major applications of magnetic compasses, munitions fuzing and mineral prospecting. Hall-effect sensors with a low sensitivity of 1–10^{6} Oe have been used for applications of non-contact switching, magnetic memory readout and current measurements. In addition to the sensitivity requirement, other factors affecting the practical uses of magnetic sensors include the processing cost and power consumption. When comparing the processing cost and power consumption of existing magnetic sensors, the GMR sensor shows the lowest cost and power consumption. However, the field sensitivity of the GMR sensor is rather low (~1%/Oe).

Recently, the development of high-performance magnetic sensors has benefited from the discovery of a new magnetic phenomenon, giant magnetoimpedance (GMI) (i.e., a large change in the ac impedance of a magnetic conductor with an ac current when subjected to an applied dc magnetic field), in metal-based amorphous alloys [4,5]. It has been demonstrated that magnetic sensors based upon the giant magnetoimpedance (GMI) effect offer several advantages over conventional magnetic sensors. The decisive factor is the ultra-high sensitivity of GMI sensors. When compared with a GMR sensor that has a sensitivity of ~1%/Oe, the field sensitivity of a typical GMI sensor can reach a value as high as 500%/Oe [3]. Though the development of GMI sensors is still at an early stage, it is likely that their low prices and high flexibility will warrant wide-ranging application in the near future.

Historically, GMI has attracted particular interest in the scientific community only since Panina and Mohri for the first time announced their discovery of the so-called GMI effect in Co-based amorphous wires in 1994 [4]. In actual ferromagnetic materials, the maximum value of GMI effect experimentally obtained to date is much smaller than the theoretically predicted value [3]. Consequently, the research in this field has been focused mainly on special thermal treatments and/or on the development of new materials for properties improvement [6–12]. In order to design and produce novel GMI sensors, a thorough understanding of the GMI phenomena and the properties of GMI materials with an emphasis on how a magnetic sensor utilising the GMI effect can be best designed for technological applications is indispensable.

The present paper serves such a purpose and aims to provide a systematic and comprehensive analysis of the fundamental aspects of GMI and its potential applications. Section 1 provides a definition of GMI before the theoretical models developed for explaining the frequency dependence of GMI are examined in Section 2. Sections 3 and 4 review the processing techniques, properties and domain structures of GMI materials, and a correlation between the domain structures and magnetic properties is established. Analyses of the effects of measuring and processing parameters on GMI are provided in Sections 5 and 6, and the underlying physical origins of hysteretic and asymmetric GMI phenomena are examined in Section 7. The materials selection criteria for the design of GMI sensors are discussed in Section 8. Finally, the authors summarise GMI sensors and their applications with an outlook of future research and development in this field.

2. Fundamental aspects of GMI

2.1. What is “giant magnetoimpedance – GMI”?

When a soft ferromagnetic conductor is subjected to a small alternating current (ac), a large change in the ac complex impedance of the conductor can be achieved upon applying a magnetic field (see Fig. 1a). This is known as the giant magnetoimpedance (GMI) effect. A typical example of the GMI effect is displayed in Fig. 1b.

The relative change of the impedance (Z) with applied field (H), which is defined as the giant magneto-impedance (GMI) effect, is expressed by

$$\Delta Z/Z(\%) = 100\% \times \frac{Z(H) - Z(H_{\max})}{Z(H_{\max})}, \tag{2.1}$$

where $H_{\max}$ is usually the external magnetic field sufficient to saturate the impedance. In practice, the value of $H_{\max}$ is available for given experimental equipment. Some researchers use $H_{\max} = 0$ in Eq. (2.1), although this definition may not be appropriate, because the value of $Z(0)$ depends on the remanent magnetic state of the material.

2.2. Impedance of a magnetic conductor

According to the definition (Section 2.1), the complex impedance, $Z = R + j\omega L$ (R and L are resistance and inductance, respectively) of a magnetic conductor is given by the ratio V_{ac}/I_{ac}, where I_{ac} is the amplitude of a sinusoidal current $I = I_{ac}\exp(-j\omega t)$ passing through the conductor and V_{ac} is the voltage measured between the ends of the conductor. Fig. 2 shows a schematic illustration of the impedance definition.

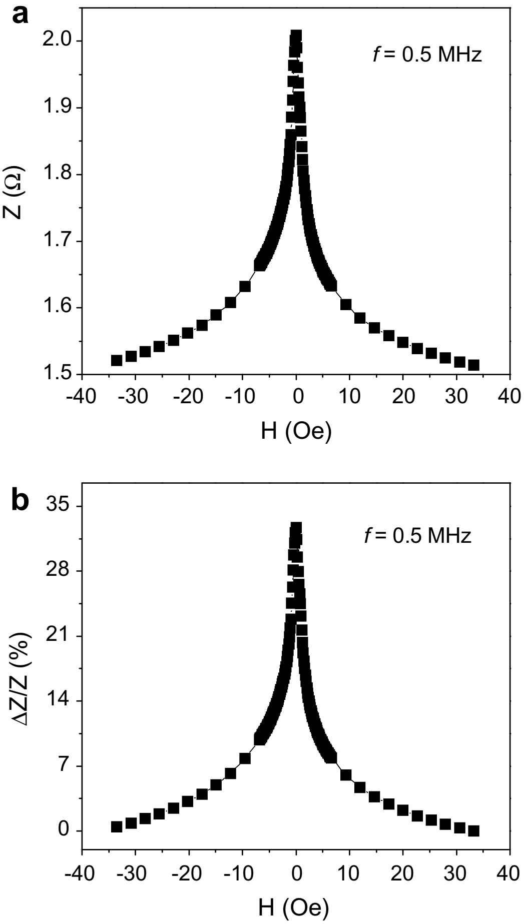

Fig. 1. (a) The impedance (Z) and (b) GMI ratio [i.e., $\Delta Z/Z(\%)$] change as a function of external magnetic field (H) for a $Fe_{71}Al_2Si_{14}B_{8.5}Cu_1Nb_{3.5}$ nanocrystalline ribbon.

Note that this definition is valid only for a uniform magnetic conductor [11]. Nonetheless, for a metallic ferromagnet with a length L and cross-sectional area q, assuming a linear approximation, its impedance can be expressed as follows:

$$Z = \frac{V_{\mathrm{ac}}}{I_{\mathrm{ac}}} = \frac{LE_z(S)}{q\langle j_z \rangle_q} = R_{\mathrm{dc}} \frac{j_z(S)}{\langle j_z \rangle_q}, \tag{2.2}$$

where E_z and j_z are the longitudinal components of an electric field and current density, respectively, and R_{dc} is the dc electrical resistance. S is the value at the surface, and $\langle\ \rangle_q$ is the average value over the cross section q. Alternatively, the expression for Z can be given in terms of the surface impedance tensor $\hat{\xi}$:

$$Z = R_{\mathrm{dc}} \frac{q}{\rho l} \left(\xi_{zz} - \xi_{z\phi} \frac{h_z(S)}{h_\phi(S)} \right), \tag{2.3}$$

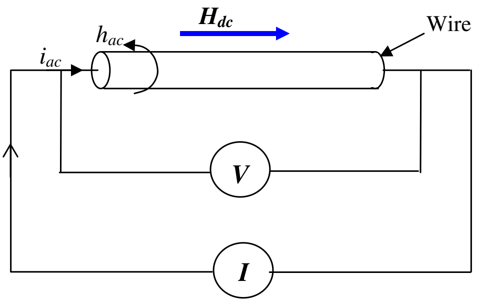

Fig. 2. The definition of impedance.

where ρ is the resistivity, l the length of the conductor and h_z and h_ϕ are the axial and circumferential components of the ac magnetic field, respectively.

The current density $j(r)$ in Eq. (2.2) or the magnetic field h in Eq. (2.3) of the conductor can generally be obtained within the framework of classical electrodynamics of continuous media, by solving simultaneously the reduced Maxwell equation

$$\nabla^2 \boldsymbol{H} - \frac{\mu_0}{\rho}\dot{\boldsymbol{H}} = \frac{\mu}{\rho}\dot{\boldsymbol{M}} - \text{grad div } \boldsymbol{M} \tag{2.4}$$

and the Landau–Lifshitz equation for the motion of the magnetisation vector

$$\boldsymbol{M} = \gamma \boldsymbol{M} \times \boldsymbol{H}_{\text{eff}} - \frac{\alpha}{M_s}\boldsymbol{M} \times \dot{\boldsymbol{M}} - \frac{1}{\tau}(\boldsymbol{M} - \boldsymbol{M}_0), \tag{2.5}$$

where γ is the gyromagnetic ratio, M_s the saturation magnetisation, M_0 the static magnetisation, H_{eff} the effective magnetic field, and α the damping parameter [13–15].

It is difficult to obtain the exact solution of the problem by solving simultaneously the Maxwell equation (2.4) and the Landau–Lifshitz equation of motion Eq. (2.5). Instead, one often assumes the material relationship between the induction and magnetic field is linear ($B = \mu H$ and μ is constant) and uses this relationship to solve the Maxwell equation while ignoring the Landau–Lifshitz equation of motion Eq. (2.5). For instance, as the classical skin effect solution of Eq. (2.4) is obtained [4,5,13], the calculated impedance Z of a cylindrical magnetic conductor and an infinite planar film are, respectively,

$$Z = R_{\text{dc}} kt J_0(kt)/2J_1(kt) \tag{2.6}$$

and

$$Z = R_{\text{dc}} \cdot \text{j}ka \coth(\text{j}ka), \tag{2.7}$$

where J_0 and J_1 are the Bessel functions of the first kind, t is the radius of the wire, $2a$ is the thickness of the ribbon, R_{dc} is the electrical resistance for a dc and $k = (1 + \text{j})/\delta_m$ with imaginary unit j. δ_m is the penetration depth in a magnetic medium, with circumferential permeability (μ_ϕ) for the case of the wire [4],

$$\delta_m = \frac{c}{\sqrt{4\pi^2 f \sigma \mu_\phi}}, \tag{2.8}$$

and with transverse permeability (μ_T) for the case of the film [5],

$$\delta_m = \frac{c}{\sqrt{4\pi^2 f \sigma \mu_T}}, \tag{2.9}$$

where c is the speed of light, σ the electrical conductivity, and $f = \omega/2\pi$ is the frequency of the ac (I_{ac}) flowing along the sample.

According to Eqs. (2.6) and (2.8), or Eqs. (2.7) and (2.9), GMI can be understood as a consequence of the increase of the skin depth until it reaches the radius of the wire (t) through the decrease of the circumferential permeability in Eq. (2.8), or until it reaches the half thickness of the ribbon (a) through the decrease of the transverse permeability in Eq. (2.9) under an applied dc magnetic field. In order to obtain large GMI values, it is necessary to reduce skin depth by choosing magnetic materials that have large μ_ϕ (or μ_T) and small δ_m and R_{dc}. It is clear that a large permeability reduces the skin depth that is later increased by the applied field as shown in Fig. 3.

In fact, the real and imaginary components of Z change with the dc applied field, H_{dc}. In a first order approximation, the in-plane component or resistance, R, can be expressed as [13]:

$$R = (\rho l)/2\pi(a - \delta_m)\delta_m. \tag{2.10}$$

This means that such changes in δ_m caused by H_{dc} via μ_ϕ (or μ_T) will modify R and hence Z. Therefore, the skin depth can be evaluated as a function of H_{dc} through the measurement of R. The inductance L can be expressed as [16]:

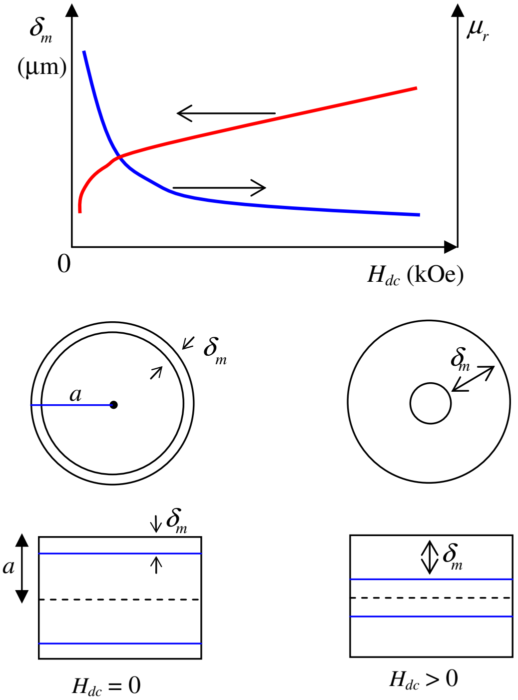

Fig. 3. Upper panel: dc applied magnetic field (H_{dc}) dependences of skin depth (δ_m) and reversible permeability (μ_r). Lower panel: a schematic view of the change of δ_m with H_{dc} for a wire and a film/ribbon, respectively.

$$L = 0.175\mu_0 lf\langle\mu_r\rangle/\omega, \tag{2.11}$$

where μ_0 and $\langle\mu_r\rangle$ are the vacuum permeability and the average relative circumferential permeability, respectively. It is pointed out that changes in $\langle\mu_r\rangle$ caused by H_{dc} will alter L and hence Z. Consequently, changes in both R and L contribute to those in Z and therefore to GMI [17].

2.3. Theoretical models

Based on the frequency (f) of the driving ac, the giant magnetoimpedance can generally be classified into the following frequency regimes:

(i) *Low-frequency regime* (up to a few kHz), where the changes in voltage at the sample's ends are mainly due the so-called magnetoinductive effect [18]. The skin effect is very weak in this case. The change in the impedance of the sample upon application of the applied field (H_{dc}) results mainly from the contribution of inductance (L), which is proportional to the circumferential permeability (μ_ϕ) for a cylindrical magnetic conductor (i.e., a magnetic wire) or the transverse permeability (μ_T) for a planar magnetic film (i.e., a magnetic ribbon) [5].

(ii) *Intermediate frequency regime* (between ~100 kHz and a few MHz), where GMI originates mainly from the variation of the skin depth due to strong changes of the effective magnetic permeability caused by the applied dc magnetic field. It is noted here that depending on sample geometry, the GMI profile can reach its peak in the intermediate frequency range (e.g., 100 kHz to 10 MHz), as a consequence of the contribution of the permeability from both domain wall motion and magnetisation rotation to GMI. Reduction in GMI at higher frequencies is related to the domain walls becoming strongly damped by eddy currents and only magnetisation rotation contributes to GMI.

(iii) *High-frequency regime* (several MHz up to GHz), where the origin of GMI is believed to be related to the gyromagnetic effect and ferromagnetic relaxation. The maxima in GMI profiles are shifted towards higher fields, where the samples are already saturated magnetically [14,19]. Strong changes in skin depth are caused by the same mechanism as in the ferromagnetic resonance.

The theoretical models of GMI representing each of the above-mentioned frequency ranges are examined and discussed below.

2.3.1. Quasistatic model

The quasistatic model has been proposed based on an assumption that the measuring frequency is small enough for an equilibrium state of the system to be reached at every moment [12,20,21]. Using this hypothesis, it is possible to use Eqs. (2.6) and (2.7) with the effective magnetic permeability or susceptibility calculated from Eq. (2.5), where $f = 0$. It has been theoretically shown that when the easy direction is perpendicular to the sample axis, the contribution of the circumferential/transverse permeability to GMI is mainly due to domain wall displacements if the domain walls are easy movable [12]. Otherwise, the contribution of the circumferential/transverse permeability to GMI results mainly from magnetisation rotation when the easy direction is parallel to the conductor axis. In general, the quasistatic model can describe basic features of GMI at relatively low frequencies, but cannot interpret the frequency dependence of GMI in the intermediate and high frequency ranges. The reason for this lies in the original assumptions made in the models.

2.3.2. Eddy current model

The quasistatic model can deal with the problem of GMI only at very low frequencies, where the so-called skin effect is very weak. However, at higher frequencies, when the skin effect becomes dominant, one must take into account the contribution of the circumferential/transverse permeability to GMI in addition to the important role played by the skin effect [4,5,22]. In this context, Panina et al. [5] have proposed the eddy current model that calculates the circumferential permeability for a periodic bamboo-like domain structure in cylindrical wires. It is worth mentioning that these authors extended, in an effective medium approximation, the validity of Eqs. (2.6) and (2.7) to the case of an inhomogeneous magnetisation arising from the domain wall structure. Herein, the microscopic eddy currents created by moving walls are averaged on the domain wall scale, thereby resulting in the frequency dependence of complex permeability in Eq. (2.8) that describes damped domain wall motion as characterised by a relaxation frequency, ω_{dw}. In fact, the magnetisation processes can occur due to not only domain wall motion but also spin rotation. Meanwhile, the losses accompanying spin rotation arise, and these are therefore described by another relaxation parameter ω_{rot}. In general, the relaxation from rotational magnetisation is much faster than that from domain wall motion, and consequently, $\omega_{\mathrm{rot}} \gg \omega_{\mathrm{dw}}$. At relatively low frequencies, $\omega < \omega_{\mathrm{dw}}$, the decrease of the permeability with frequency is related to damped domain wall motion due to eddy currents.

It has been shown that, at low frequencies, the external magnetic field dependence of the impedance is associated with the internal part of the inductance L, which is proportional to the static circumferential permeability, μ_{ϕ}. It has also been highlighted that the eddy current loss is much less in a wire-shaped sample with a circular domain structure than that with a striped domain structure [4,5]. This explains why the permeability retains its value at higher frequencies. In the high frequency case ($a \gg \delta_{\mathrm{m}}$ and $\omega_{\mathrm{dw}} < \omega \leqslant \omega_{\mathrm{rot}}$), both R and L depend on μ_{ϕ} and therefore contribute to the GMI behavior. The skin effect is dominant in this case and the impedance is proportional to the square root of frequency and circular permeability, $Z \propto (\omega \cdot \mu_{\phi})^{1/2}$. As frequency is further increased ($\omega > \omega_{\mathrm{rot}}$), the resistive term becomes greater and contributes to the total impedance Z. In this instance, the impedance is independent of the external magnetic field (H_{dc}), because the permeability is magnetic field independent [21]. In general, the eddy current model has explained successfully the basic GMI features and most experimental results in the frequency range of 100 kHz to 30 MHz.

2.3.3. Domain model

The domain model is considered a more rigorous treatment of the GMI problem of a metallic soft magnetic wire with periodic circular domains than the eddy current models. It was initially proposed by Chen et al. [23,24] and has allowed one to interpret qualitatively the single and double-peak GMI curves and several experimental results for studying GMI of amorphous wires. Although theoretical calculations for impedance (Z) were quite consistent with experimental data, a poor agreement between the theoretical predictions and experimental results of the circumferential permeability was found. This has recently been resolved by Betancourt et al. [25] by modifying the proposed domain models [23], in which only complex inductance formalism (L) was used to calculate the circumferential permeability instead of using Z equations. The correlation between the inductance and permeability was established, allowing the evaluation of the circumferential permeability as a function of frequency and hence resolving its dispersion law. However, the domain models could not explain satisfactorily the underlying mechanism of relaxation dispersions of permeability spectra in amorphous magnetic materials [26–30]. In this context, Kim et al. [27,28] have proposed a phenomenological model that allows one to separate the reversible domain wall motion and magnetisation rotation components in permeability (or susceptibility) spectra of amorphous magnetic wires and ribbons. These studies have provided a basic physical understanding of the realistic contribution of domain wall motion and rotational magnetisation processes to GMI for a small driving field.

In general, the eddy current and domain models have explained successfully several basic features of GMI at frequencies below 100 MHz. When a high frequency leads to a skin depth comparable with the exchange length, both models are inaccurate [14]. This is because ferromagnetic resonance occurs at high frequencies $f \sim 1$ GHz and becomes the main effect responsible for GMI behavior [14,19]. In this context, the high-frequency models, including the electromagnetic and exchange-conductivity models, should be considered.

2.3.4. Electromagnetic model

In the high-frequency regime, contribution of domain wall motion to the circumferential/transverse permeability and hence to GMI can be neglected and only magnetisation rotations considered. The electromagnetic model has approached the solution of Eqs. (2.4) and (2.5) using the theoretical procedures of ferromagnetic resonance (FMR), without considering the exchange interactions in the effective field [15,19,31,32]. The relationship between GMI and FMR have been reported by Yelon et al. [19,32] for magnetically saturated samples. The absorption of energy is understood as an increase of impedance to the electromagnetic radiation that occurs at the resonance frequency,

$$\omega_r = \gamma\mu[(H + M_s)(H + 2K/\mu M_s)]^{1/2} \tag{2.12}$$

with γ and K being the gyromagnetic ratio and the anisotropy constant, respectively. Here, the circumferential/transverse permeability shows a typically resonant behavior with the maximum of the imaginary part and the change of sign of the real part at the resonance field determined by the FMR resonance condition [33]. At the resonance field, the effective permeability increases drastically and the skin depth is very small. At a given frequency, increase of the dc magnetic field (H_{dc}) leads to a shift of the resonance frequency, thereby reducing the permeability and resulting in a remarkable GMI effect. The theoretical skin depth reaches its minimum value ($\sim$0.1 μm)

$$\delta_{\min} = \sqrt{\frac{\alpha\rho}{\gamma\mu M_s}} \tag{2.13}$$

and the GMI reaches its maximum value. The maximum GMI value calculated from Eq. (2.13) is independent of frequency, and its magnitude (i.e., of the order of $\sim 10^3$) is much larger than that experimentally obtained [10]. This arises from the fact that GMI measurements are usually conducted at frequencies less than 100 MHz, where such FMR condition cannot be satisfied [19]. Furthermore, the magnitude of GMI calculated by the electromagnetic models can be obtained only in uniaxial magnetic materials with easy direction of the anisotropy exactly perpendicular to the sample axis and the dc applied magnetic field. However, in real materials there always exists a deviation of easy axis from the perpendicular direction of the anisotropy [12]. It is for this reason that a substantial deficiency between the experimentally observed and theoretically calculated GMI values has been found [10,19,32]. It is worth mentioning that in the GHz region the experimentally observed GMI data exhibits close agreement with the theoretical prediction [19,32], since the FMR condition can be satisfied in this frequency regime [33].

In general, the electromagnetic model can qualitatively interpret the basic features of GMI and most of the experimental data in the high-frequency regime. However, some aspects of GMI cannot be completely resolved using this model, because the role of the exchange interactions in the effective field is neglected [14,34].

2.3.5. Exchange-conductivity model

In addition to the role played by the exchange interactions in the electromagnetic model, the exchange-conductivity model accounts for the exchange stiffness [35]. As a result, when the exchange term is included in the effective magnetic field H_{eff}, Eqs. (2.4) and (2.5) must be solved simultaneously [10,14,34–36]. In reality, the exchange-conductivity effect is caused by the interplay between the skin effect and the exchange interaction. Due to the skin effect, the ac component of magnetisation induced by an ac flowing along the conductor axis decreases in magnitude from the surface to center. Consequently, the magnetisation is inhomogeneous and exchange energy arises accordingly. Such an increase of the exchange energy (or exchange interaction) weakens the skin effect and the skin depth is consequently increased [10]. Herein, it is the inhomogeneous ac magnetic field that excites spin waves with wavelengths of the order of the skin depth, which enhances the energy dissipation by eddy currents. This can be understood as an apparent increase of resistivity in ferromagnetic materials [36].

Using the simplified solution to Eqs. (2.4) and (2.5), the exchange-conductivity models have shown that, when the damping is neglected ($\alpha = 0$), the skin depth reaches its minimum value [14]

$$\delta_{\min} = \left(\frac{A\rho}{\omega\mu^2 M_s^2}\right)^{1/4}, \tag{2.14}$$

when ω is less than the characteristic frequency

$$\omega_c = \frac{4\alpha^2\gamma^2 A M_s}{\rho}, \tag{2.15}$$

where A is the exchange stiffness constant. ω_c is evaluated as approximately 100 MHz for soft magnetic amorphous materials. At low and intermediate frequencies ($\omega < \omega_c$), the calculated maximum GMI scales as $\omega^{1/4}$. Above the characteristic frequency ($\omega \geqslant \omega_c$), the GMI is calculated using Eq. (2.13).

The exchange-conductivity model allows one to qualitatively interpret the frequency and magnetic field dependences of GMI in a wider range of frequencies than the electromagnetic models. However, neither model deal satisfactorily with the problem of GMI as a whole, due to the complex domain structures of actual magnetic materials [4,5,7] and the given approximate assumptions [10,12,14].

2.3.6. Other theoretical models

Although the previously mentioned models can qualitatively interpret basic GMI features for cylindrical and planar magnetic conductors over a broad frequency range, some controversies still remain in the theory of GMI for ferromagnetic materials [37–40]. For instance, a controversy arises regarding the energy conservation of the GMI effect. To resolve these issues, a simple model of the GMI effect in amorphous thin films has been proposed by Dong et al. [38] whereby the expressions of effective permeability and impedance are derived in the framework of classical electrodynamics and ferromagnetism. Using the existing model [38], Phan et al. [39] modelled the magnetic field and frequency dependences of GMI in film-type materials as displayed in Fig. 4. As one can see from Fig. 4, the model [38] can interpret a shift of the impedance peak towards a higher value of the dc magnetic field (H_{dc}) with increasing frequency (f), which is in agreement with experimental results for relatively high frequencies ($f > 1$ MHz). However, it cannot explain the evident single-peak behavior of the GMI profile in the low-frequency range ($f \leqslant 1$ MHz).

Considering the magnetoresistance (MR) contribution to the magnetoimpedance (MI) effect in thin films, a simple model has been proposed by Barandiaran et al. [40]. It has been revealed that such MR and MI phenomena are similar, but there is a divergence in the origin of these phenomena. The MR effect, reflecting a change in resistance of a magnetic material subjected to a magnetic field is connected to spin dependent electron scattering in magnetically non-uniform systems for dc or low-frequency current. In contrast, the MI effect consists of the change in the total impedance (including both resistance and inductance) of a magnetic conductor under a dc applied magnetic field, when a high-frequency ac follows through it. The theoretical calculations show that the contribution of MR to the MI effect is dominant in the low frequency regime but can be neglected for the

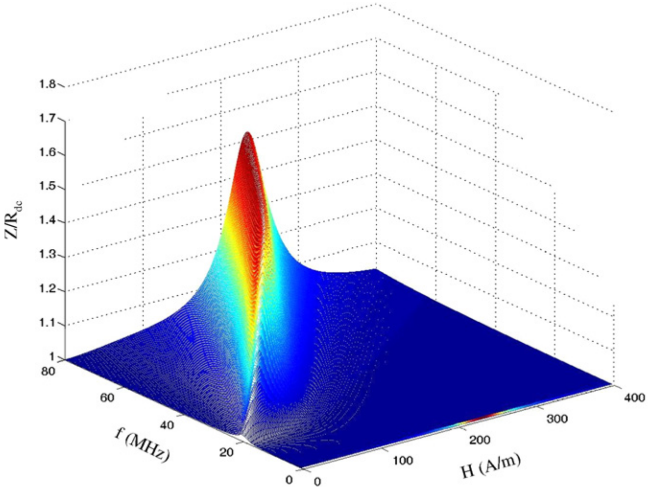

Fig. 4. The magnetic field (H) and frequency (f) dependences of the relative impedance (Z/R_{dc}), simulated using the model proposed for amorphous thin films.

high-frequency range [40]. This has been experimentally verified by Kurlyandskaya et al. [41] when investigating the magnetoresistance and magnetoimpedance effects in Fe–Ni thin films.

3. Processing techniques for the production of GMI materials

3.1. Amorphous metallic wires

3.1.1. Melt spinning

Amorphous metallic alloys can be produced by a variety of rapid solidification processing techniques, including splat quenching, melt spinning, gas atomisation and condensation from the gas phase. Among the existing techniques, the melt spinning technique has been most widely used to produce amorphous metallic alloys at cooling rates of 10^4–10^6 K/s [42]. Metallic amorphous wires are also prepared by the melt spinning method that has been used to yield amorphous ribbons [43,44]. Diameters of the produced wires range from 1 to 300 μm [44,45]. The central element of this process is the pressure ejection of melt stream through an outlet into a cooling fluid followed by rapid solidification of this stream before it breaks into droplets. It has been highlighted that the following important conditions need to be satisfied to allow the production of metallic wires directly by the rapid solidification from the melt: (i) solidification of the metallic melt stream at high cooling rates and within the “stability” distance from the ejection point; (ii) use of a cooling fluid with low viscosity and surface tension; and (iii) stable and non-turbulent flow of the cooling liquid at high velocities. In reality, because of the difficulty of simultaneously maintaining high supercooling capacity of the metallic melt stream without the precipitation of crystalline phases in a temperature range between the melting temperature and glass transition temperature, the melt spinning method is limited to produce metallic alloy wires with high glass-forming ability. To overcome this problem, Ohnaka et al. [46] developed this method into the so-called in-rotating water spinning method.

3.1.2. In-rotating water spinning

This technique is modified from the melt spinning technique in that, instead of allowing the melt stream to impinge on the interior of a rotating drum, the melt stream is directly ejected into rotating water [46–48]. A cross-sectional view of an in-rotating water spinning device for producing magnetic wires is illustrated in Fig. 5. It has been shown that during the in-rotating water spinning process, a jet of molten metal is ejected through a quartz nozzle of 80–200 mm diameter into a liquid cooling layer formed by a centrifugal force on the inner surface of a rotating drum of about 400–600 mm diameter. The speeds of the rotating coolant and the melt jet can be controlled by the rotation of the drum and the ejection gas pressure, respectively [47]. Depending upon the alloy being cast, it is necessary to adjust the distance between the nozzle tip and the coolant surface, the ejection angle, the depth of the coolant layer and the coolant temperature. The in-rotating water spinning technique allows production of continuous wires of round cross section. In these wires a dendritic structure forms along the wire direction, whereas for melt-spun ribbons, this structure tends to grow transverse to the casting direction. The cooling rate is often around 10^5 K/s. A wide variety of ferrous and non-ferrous alloys have been cast into amorphous or microcrystalline wires. Amorphous metallic wires with diameters ranging from 80 to 160 μm were obtained by the in-rotating water spinning method [46]. Wires

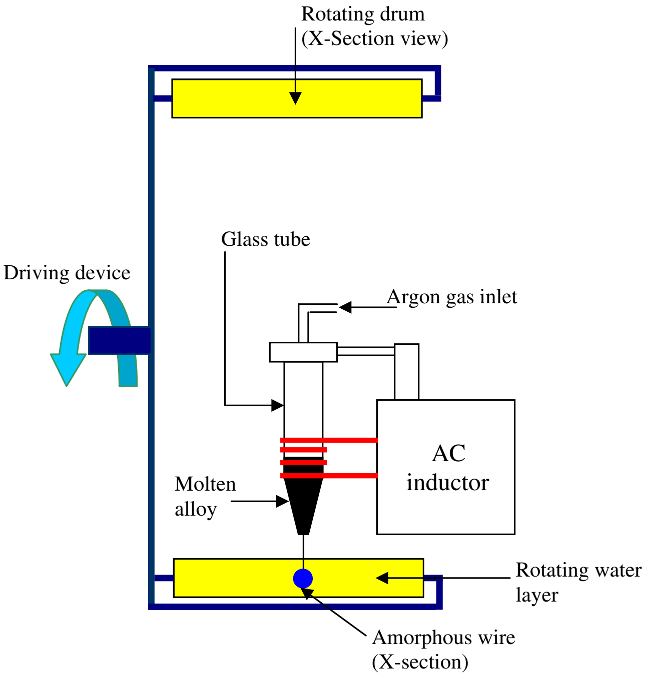

Fig. 5. Cross-sectional view of the in-rotating water spinning device for producing magnetic wires.

with thicker diameters of up to ~300 μm [49], or with thinner diameters down to 30 μm [50], have also been reported. One of the main advantages of the in-rotating water spinning method is that it can be used to produce wires with alloy compositions that are difficult to obtain using the conventional methods.

3.1.3. Taylor-wire process

In 1924, Taylor [51,52] first introduced a technique that allows production of fine wires of uniform cross section. A schematic illustration of the Taylor-wire process can be found in [51]. In this process, a metallic charge is put in a glass tube and this material is melted by induction heating. As a result, the glass tube is softened due to its contact with the molten metal and it can then be drawn. While acting as a continuous mold crucible during solidification of the metal, it ensures a regular surface and uniform diameter of the wire. The final product consists of a metallic wire in a glass sheath and is collected on a rotating drum at speeds of around 5 m/s. The cooling rate of this process might vary in the range of 10^4–10^6 K/s for producing wires of 50 μm down to 2 μm diameter [52,53]. A wide range of metallic wires has been produced by the Taylor method including steels, coppers, and noble metals as well as low-melting point metals [53]. One of the main challenges of this technique is to find sheath materials that possess a sufficient chemical inertness towards the molten metal used, as well as having a softening temperature consistent with the melting temperature of the metal. However, one problem arising in this technique is the contamination of the material by the glass sheath. To avoid this problem, it is necessary to choose a glass compatible with the material in terms of its chemical properties, viscosity and melting temperature. A number of recent works have evaluated the microstructure, as well as the mechanical, electrical and magnetic properties of several microcrystalline and amorphous alloys [54].

3.1.4. Glass-coated melt spinning

This is a modification of the Taylor-wire technique, which allows alloy systems with low wire forming capacity to be easily produced. The ability of a metallic melt stream to break into droplets before solidification is drastically reduced by the presence of the glass cover, which prevents a direct contact between the molten metal and the cooling liquid [55–60]. The glass cover ensures a smooth cylindrical shape for the melt stream. Compared with the in-rotating water spinning method, the glass-coated melt spinning method ensures higher cooling rates, thus producing amorphous wires more easily, even in the presence of the glass cover [59,60].

This technique was originally proposed by Wiesner and Schneider [55] and later developed by Ulitovsky [56,57]. A schematic illustration of the glass-coated melt spinning method is presented in Fig. 6 [59]. In this process, the molten metal is captured as soon as the rapid drawing of a softened glass capillary takes place. The capillary is drawn from the end of a glass tube containing the molten metal. Alloy pieces are first put into the glass tube and are then melted by a high-frequency furnace using an inductive coil. There is a softened glass cover around the molten metal drop and this allows the drawing of the capillary to take place. To avoid any occurrence of metal oxidation, it is usual to apply a low level of vacuum of about 50–200 Pa, or an inert gas atmosphere (e.g., argon) within the glass tube. In order for the drawing process to be continuous, Chiriac [58] proposed that the glass tube be displaced with a uniform speed of 0.5–7 mm/min. The as-formed wire is cooled by a water jet at approximately 1 cm under the high-frequency induction heating. Depending upon the drawing velocity, it is likely that the cooling rate varies from 10^4 to 10^7 K/s. Detailed analyses on external parameters affecting the preparation routes of wires can be found in Refs. [58–60]. Using this method, Chiriac [58] produced metallic amor-

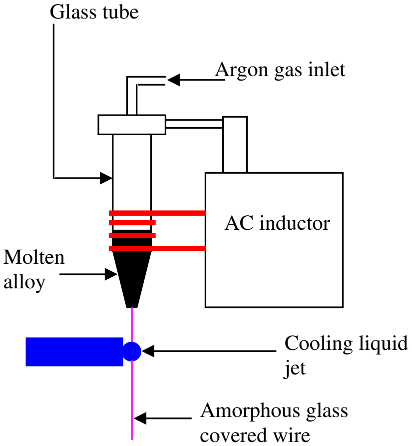

Fig. 6. Schematic illustration of amorphous wires/microwires fabrication process by the glass-coated melt spinning method.

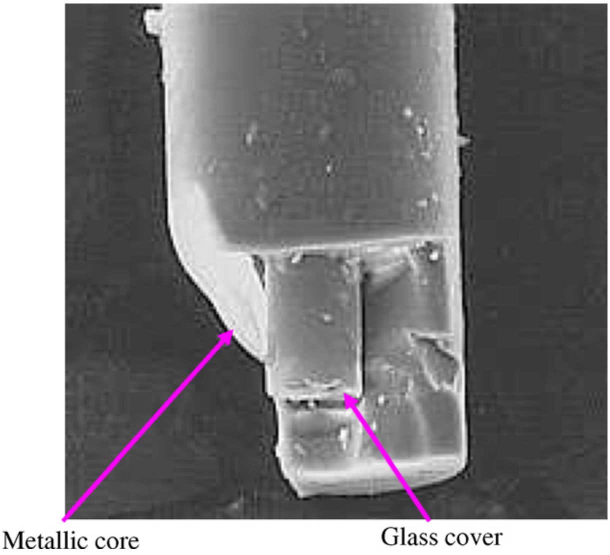

Fig. 7. SEM image of a glass-coated amorphous microwire (courtesy A. Zhukov).

phous glass-covered wires with metallic core diameters of 3–25 μm and glass thicknesses of 2–15 μm. In the case of microwires, metallic core diameter is typically between 0.8 and 30 μm, while the thickness of the coating is in the range of 2–15 μm [59,60]. For example, an SEM image of a Fe–Si–B–Cu–Nb glass-coated amorphous microwire is displayed in Fig. 7. Final wire dimensions such as the metallic core diameter and glass cover thickness can be accurately determined with the help of a high-resolution optical microscope engaged with a video camera and both controlled by a computer [58–60]. The glass-coated melt spinning method of wire/microwire fabrication provides several advantages over the other methods, such as (i) repeatability of wire properties at mass production and (ii) a wide range of variation in parameters (geometrical and physical), possible fabrication of continuous long wires up to 10 km and possible control and adjustment of geometrical parameters during the preparation process. Therefore, amorphous wires/microwires (Co-based and Fe-based alloys) have usually been produced by this method.

3.1.5. Electrodeposition

Electrodeposition is a method that has been used recently to produce uniform wires consisting of non-magnetic conducting inter core (e.g., Cu, BeCu, and W), and magnetic outer shell layers (e.g., FeNi, FeNi–Al_2O_3, and CoP) [61–77]. This method is used for coating a metallic wire with a similar or dissimilar metallic plating layer having the desired uniform thickness and a compact metallic structure by passing the wire through electrolytic baths and through surface smoothing stations. Fig. 8 shows a diagram of the electrodeposition process. In this process, the wire is passed through an electrolytic bath to coat the wire with a plating layer, then pressed against the peripheral surfaces of rotating rollers to smooth the surface of the plating layer over the entire periphery. Finally, the wire is coated with a secondary electrolytic plating layer. The non-magnetic conducting inter cores are often wires with diameters of around 20 μm [62–65]. The magnetic layer is often

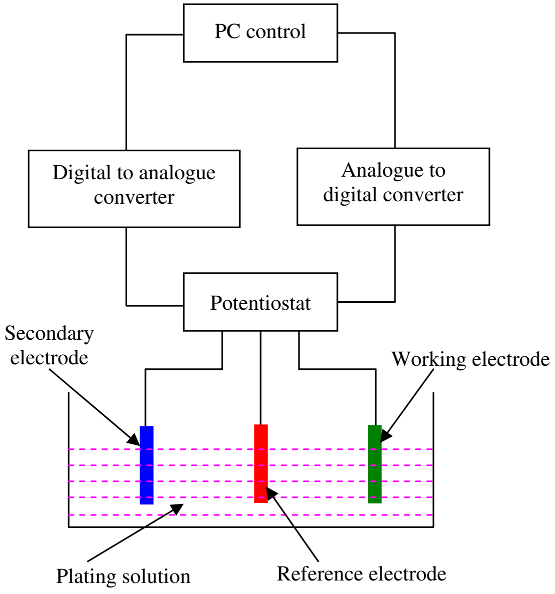

Fig. 8. Schematic diagram of the electrodeposition process.

thin and ranging between 2 and 7 μm. For instance, Fig. 9 displays an optical image of a Cu wire with and without a CoP layer; the inset shows a SEM image of a CoP/Cu wire cross section. In the electrodeposition process, the thin magnetic layer is formed over the inter wire using a constant electrolytic current density. By keeping the current density constant, the layer thickness can be controlled by the deposition time. The main difficulty of this method is controlling the desired composition ratio [62–67]. This problem can be overcome by applying a longitudinal magnetic field during the deposition process, which is currently known as the magnetically controlled electroplating method [68,69]. In addi-

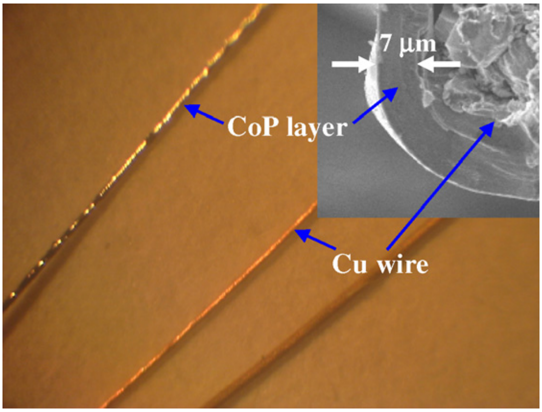

Fig. 9. Optical image of a Cu wire with and without CoP layer. The inset shows a SEM image of a CoP/Cu wire cross section.

tion, the application of a longitudinal magnetic field during electrodeposition results in an improvement of the uniform surface properties of the wires, which is beneficial for sensor applications [69]. In general, the electrodeposition method has the following advantages: (i) a wide range of materials (metals, alloys, and composites) that can be processed by electrodeposition is available; (ii) both continuous and batch processing are possible; (iii) materials with different grain size and shape can be produced; (iv) materials with full density (i.e., negligible porosity) can be produced; and (v) the final product can be in the form of a coating or bulk material.

3.2. Amorphous metallic ribbons

Due to ease of manufacture, single-roller melt spinning is the most widely used method for producing long and continuous ribbons of metallic glasses. Chen and Miller [78] designed the single-roller device by using a metallic (Cu–Be) wheel spinning at 300–1800 rpm. In this process, a liquid stream impinges on the inside of the wheel's torus-like convex surface. The quenched ribbons slip out of the wheel under the action of the centrifugal force. Ribbons produced by this method are usually of 0.5 mm width, 20 μm thickness, and up to 100 m length. A further improvement in the single rotating copper wheel technique has been made allowing one to quench the melt on the outside of the spinning wheel [42,79]. A schematic illustration of this method is displayed in Fig. 10. The liquid is spread in the form of a continuous ribbon with quenching rates of 10^6–10^8 K/s. With currently available devices, it is possible to produce ribbons with a width of up to several decimeters. A wide variety of materials (e.g., Fe, Co, Ni, and their alloys) can be produced using the single rotating copper wheel technique. It has been shown that the melt temperature influences the ribbon thickness and therefore affects the size distribution of the final nanocrystals throughout the transformed ribbon after nanocrystallisation [79]. The influence of the processing parameters on the properties of ribbons has been extensively studied [42,79].

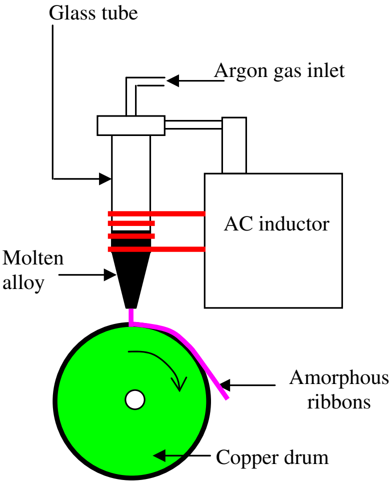

Fig. 10. Schematic illustration of the single roller melt-spinning apparatus used to produce amorphous metallic ribbons.

3.3. Magnetic thin films

A number of methods for the fabrication of film-type materials, such as evaporation, sputtering, chemical vapor deposition, electrolytic deposition, and atomic layer epitaxy, are currently available. Among them, the sputtering method has been most widely used to produce single and multilayer metallic films. An illustration of the sputtering process is displayed in Fig. 11. In this process, atoms are removed from a surface as a result of the impact of energetic ions. An inert gas, pressure of 0.1–10 Pa is maintained in the deposition chamber and the target is the cathode of a gas diode. A detailed illustration of this system can be found in the work by Feldman and Mayer [80]. It is worth noting that the planar magnetron source is the most widely used because of its reliability, efficiency and reproducibility. A high deposition rate of 0.1–10 nm/s may be achieved with this system depending upon the target material and the capacity for target cooling. However, slower rates are preferred for precise deposition of multilayers. In order to achieve a uniform deposition rate, accurate controls of power and pressure are required.

Among the metallic films of interest, the multilayered thin films have been extensively studied with respect to GMI [81–84]. In this instance, films with a sandwich structure have proven to be superior to single-layer thin films [62]. In principle, this typical multilayer (F/M/F) has two soft ferromagnetic layers (F = CoFeSiB, FeNiCrSiB, FeSiB, etc.) sandwiching a non-magnetic highly conductive layer (M = Cu, CuBe, Ag, Ti, etc.). The thickness of the ferromagnetic layer (d) is in the range of 0.1–4 μm, while the thickness (D) of the conductive layer is often around 2 μm. The thickness of ferromagnetic layers (F) and conductive layers (M) can be controlled during the fabrication process and the excellent magnetic properties of the films can be optimised accordingly [83]. The influences of thickness on the magnetic and magnetoimpedance properties in multilayered films have been investigated [82–84].

3.4. Nanocrystalline magnetic alloys

Since the physical properties of metallic materials (e.g., mechanical, magnetic, and electrical properties) are sensitive to their microstructure, several methods of controlling the

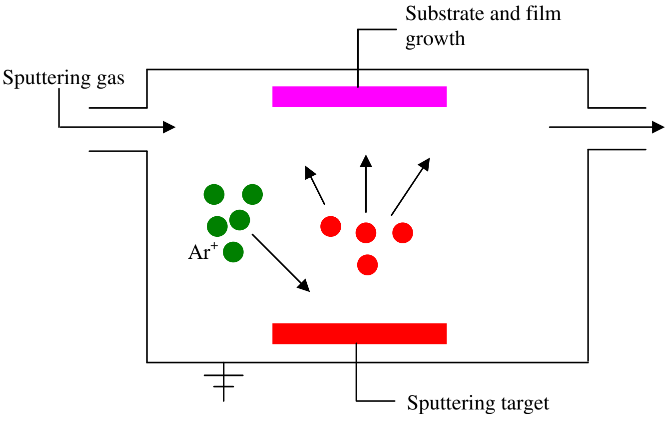

Fig. 11. Schematic illustration of the sputtering process for producing thin films.

microstructure (e.g., thermal treatment, thermomechanical treatment, and plastic deformation) have been effectively used for improving the material properties. It has been shown that when the scale of the structure of metallic materials reaches a nanometer scale, the material properties change drastically and are different from those of conventional materials on a macro scale [79].

Nanocrystallisation itself has been known for a long time, but Yoshizawa et al. [85] first reported that a Fe–Si–B–Nb–Cu amorphous alloy exhibited the excellent soft magnetic properties when subjected to proper thermal treatments. It is the reduction of the crystal grain size (α-Fe(Si)) to a nanometer scale that results in the superior soft magnetic properties of the material. A comprehensive description of the main routes to obtaining Fe–Si–B–Nb–Cu nanocrystalline materials by crystallising their amorphous precursors is illustrated in Fig. 12. This nanocrystalline microstructure evolution process in the Fe–Si–B–Nb–Cu alloy has been proposed based on the three-dimensional atom probe (3DAP) studies [86]. The initial amorphous phase is a chemically uniform amorphous solid solution. Upon annealing, Cu clusters appear in the fully amorphous matrix, which has the short-range structure. The concentration of Cu in the clusters appears to be much lower than 100 at.% during the first stage, but gradually increases and the clusters eventually evolve to face-centered-cubic (fcc)-Cu. These Cu particles act as heterogeneous nucleation sites for α-Fe primary crystals, from which Nb and B atoms are rejected. The rejected solutes are enriched in the remaining amorphous phase, which results in stabilisation of the remaining amorphous phase. This in turn retards further growth of the α-Fe nanocrystals. Si partitions grow in the α-Fe phase, ending up with Fe–20Si with the DO_3 structure. Because the grain size is small (~10 nm), the α-Fe(Si) grains are exchange coupled; this exchange coupling occurs through the thin intergranular ferromagnetic amorphous phase.

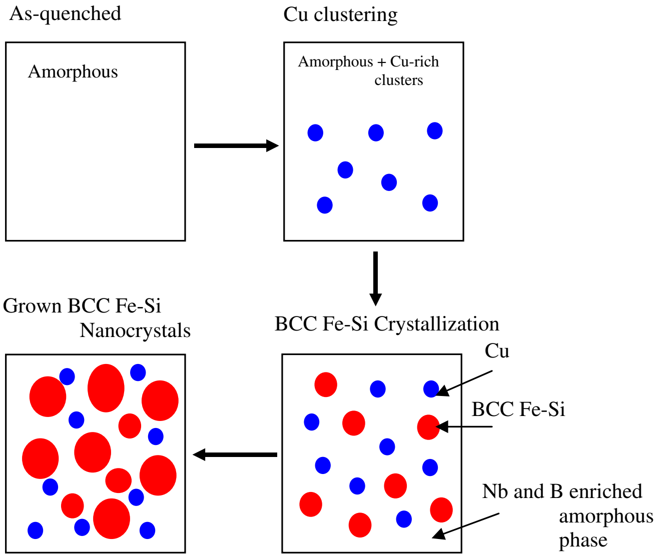

Fig. 12. Schematic illustration of the microstructural evolution of melt-spun Fe–Si–B–Nb–Cu amorphous alloy by primary crystallisation (after Hono et al. [86], reproduced with permission from Elsevier).

The presence of the remaining amorphous phase is not required to reduce the net magnetocrystalline anisotropy, but the co-existence of the two phases gives a good balance of positive and negative magnetostriction (λ), resulting in very low net magnetostriction [79]. Consequently, the ultrasoft magnetic properties of the nanocrystalline material are achieved. A wide variety of nanocrystalline materials with superior soft magnetic properties, including nanocrystalline wires, ribbons and thin films, are synthesised by crystallising their amorphous precursors utilising the annealing method. Regarding the heat treatment procedures, it should be noted that the choice of annealing conditions (e.g., annealing temperature and time), depends upon prepared alloy compositions, and is extremely important for obtaining such optimised nanocrystalline materials [87]. Heat treatment can be conducted, based on DSC, X-ray diffraction, and TEM analyses. In order to further improve some desired properties (e.g., magnetic anisotropy) of a magnetic material, application of a magnetic field or a tensile stress on the sample during the annealing process is often recommended. They are, respectively, the field – and stress-annealing methods.

3.5. Comparison of fabrication technologies

Table 1 summarises the fabrication technologies and their product parameters. It is worth noting from Table 1 that the information about cooling rates can help to evaluate the relative efficiencies of the different quenching techniques. The first two methods (melt spinning and in-rotating water spinning) allow the production of metallic amorphous wires without a glass cover, which are preferred as conventional amorphous wires (CAW), while the glass-coated melt spinning method (or the modified Taylor-wire method) produces thin amorphous glass-covered wires (AGCW). From an engineering point of view, AGCW is more promising for technological applications when compared with CAW. In particular, amorphous microwires are ideal for sensing applications in micro-systems [6,7,58–60]. The magnetic wires with glass cover are particularly useful for electrical applications in industry. Electrodeposited wires are very interesting owing to their uniform magnetic properties. However, it is quite difficult to produce very long wires using the electrodeposition technique. Magnetic amorphous ribbons and films, which have been produced by the melt spinning and sputtering techniques, respectively, are becoming competitive with amorphous wires, since they also exhibit excellent magnetic properties which are appropriate for sensor applications.

Table 1
Fabrication technologies and their product parameters

Technique	Product type	Typical dimensions (μm)	Typical cooling rate (K/s)
Melt spinning	Circular section wire	1–300 diameter	10^4–10^6
In-rotating water spinning	Circular section wire	30–300 diameter	10^5–10^6
Taylor-wire process	Circular section wire	2–100 diameter	10^3–10^6
Glass-coated melt spinning	Wire/microwire with glass cover	3–50 diameter	10^4–10^7
Electrodeposition	Wire with magnetic layer	20–1000 diameter	–
Single roller melt spinning	Amorphous ribbons	15–25 thickness	10^6–10^8
Sputtering	Thin films	0.1–10 thickness	–

The synthesis of nanocrystalline materials through crystallising their amorphous precursors has been a popular method for improving the soft magnetic properties of the materials, while retaining the same dimension of the sample. A variety of annealing methods (e.g., current annealing, field annealing, stress annealing, laser annealing, etc.) have been proposed and used to produce such nanocrystalline materials. For some technological applications (e.g., transformer cores), nanocrystalline magnetic materials have been found to exhibit superior properties to their amorphous counterparts.

To this end, it is worth mentioning that, in the case of glass-covered wires, the removal of the glass-cover may be of interest in developing specific sensing devices. The technique of glass removal is described in the next section.

3.6. Techniques for glass-cover removal

Magnetic amorphous glass-covered wires (AGCW) and microwires are ideal for specific applications, particularly in electrical industries, owing to the presence of the insulating glass-covered layer. In some cases, however, the removal of the glass-covered layer of AGCW may be of significant interest in fundamental research, as well as in practical uses, because this process can lead to considerable variation in the mechanical and magnetic properties of the wire [7,60].

In practice, glass removal can be conducted either by the conventional mechanical method or by chemical etching with a hydrofluoric acid (HFA) solution. The former usually leads to a degradation of the material properties (e.g., mechanical, electrical, and magnetic) and therefore is not recommended. The latter has been shown to be a useful tool for glass removal of AGCW, and this process results in less damage to the wire. However, in the chemical etching method, the concentration of HFA solution must be gradually diminished in order to avoid etching to the metallic core, and so the last glass pieces are finally washed with water for this reason. This entire process can be monitored by permanent optic control.

4. Domain structure and properties of GMI materials

4.1. Domain structure

Different domain structures are observed in different types of materials. The domain structure of a rapidly quenched material is often determined by coupling between magnetostriction and internal stresses frozen in during the fabrication process. Such knowledge of the domain structure of an actual material is extremely important in controlling and tailoring the magnetic properties of the material. This section is devoted to describing the formation of the domain structures in materials (e.g., wires, ribbons, and thin films) that is then reflected by their magnetisation processes and their magnetic characteristics.

4.1.1. Magnetic wires

In a rapidly quenched wire, a complex radial distribution of internal stress with axial, radial and circular components is often generated due to different quenching rates between the surface layer and the central region of the wire [88,89]. Here, the sign and magnitude of magnetostriction constant (λ) determines the type of domain structure in the wires.

For amorphous wires with positive magnetostriction (e.g., Fe-based wires), the quenched-in stress distribution may result in a longitudinal easy axis in the cylindrical core and radial easy axes in the tubular shell. The inner core usually occupies about 70% of the total volume of the wire [7]. A schematic illustration of the simplified domain configuration of this commonly used wire is presented in Fig. 13. There exists an inner cylindrical domain with longitudinal magnetisation and a basic radial domain with complicated closure domains. Such a domain structure is responsible for an axial large Barkhausen effect (LBE) in the wire, which is desirable for several technical applications [6,7]. The closure domain structure has been realised by domain pattern observation and by magnetisation and susceptibility profiles [89]. For a low magnetostrictive wire with a normal length (~4 mm), the core of the wire actually has a multi-domain structure [90].

For amorphous wires with negative magnetostriction (e.g., Co–Si–B wires), the quenched-in stresses may cause the surface anisotropy to be circular and the inner anisotropy to be perpendicular to the wire axis, thereby leading to the formation of a specific domain structure, which consists of outer shell circular domains and inner core axial domains as illustrated in Fig. 14. It is the coupling between the compressive stress and the negative magnetostriction that leads to an alignment of the magnetic moments in a circumferential direction. The minimal demagnetising energy favors the circumferential orientation which was observed experimentally [6,7]. It can be seen that the inner core domain structure of negative-magnetostrictive CAWs (Fig. 14) is the same as that of positive-magnetostrictive CAWs (Fig. 13), and this results in the negative-magnetostrictive CAWs also exhibiting an axial LBE. It should be noted, however, that there actually exists a different inner core domain structure between negative-magnetostrictive CAW and AGCW. The easy axis of the inner core domains of CAW is axial while it is radial for AGCW. The reason for this is that the presence of the glass-cover layer in AGCW is leading to a specific distribution of internal stresses in the inner core of the wire. In the case of amorphous glass-covered microwires with large and negative magnetostriction, the shell with circular domains practically occupies the entire volume of the wire as a consequence of the strong circular magneto-elastic anisotropy. The main difference in the domain structure between typical positive- and negative-magnetostrictive amorphous wires (Figs. 13 and 14) is that the easy magnetisation direction in the shell is radial in the case of positive magnetostriction (Fe-based) wires, whereas for negative magnetostriction (Co-based) wires it becomes circular. This is understood to be the main reason for the difference in the magnetic behaviors between the Fe-based and Co-based wires.

For amorphous wires with negative and nearly zero magnetostriction (or vanishing magnetostrictive wires, Co–Fe–Si–B, for example), other kinds of anisotropies may over-

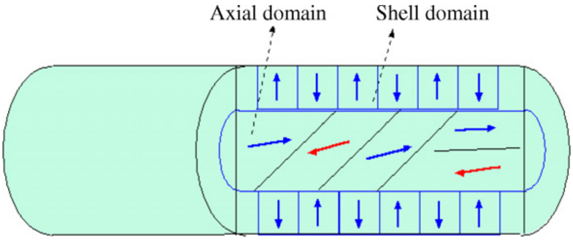

Fig. 13. Simplified domain configuration of a typical conventional amorphous wire (CAW) with positive magnetostriction.

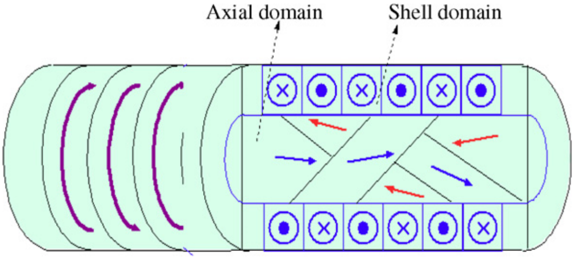

Fig. 14. Simplified domain configuration of a typical conventional amorphous wire (CAW) with negative magnetostriction.

come the stress anisotropy, and consequently, the domain structure is not well defined. In practice, the domain structure of these wires is often considered to be similar to that of the negative-magnetostrictive amorphous wires. It is noted that thermal and mechanical treatments may significantly modify the domain structures of these rapidly quenched wires. A typical example of the domain structure modification caused by changes of internal stresses is the case of removing the glass-cover layer from a typical amorphous glass-covered wire (AGCW) as illustrated in Figs. 15 and 16. It can be seen that for the case of the positive-magnetostrictive AGCWs, the glass removal leads to an increase in the outer shell domains' volume, but a decrease in the inner core domains' volume. As a result, the domain configuration remains unchanged for the positive-magnetostrictive AGCWs after glass removal (see Fig. 15a and b). It is estimated that the maximum value of the axial tensile stress for glass-removed wires is approximately 50% smaller than for glass-covered ones [7]. This may result in a further improvement in the magnetic softness as well as the GMI effect of such positive-magnetostrictive AGCWs after glass removal.

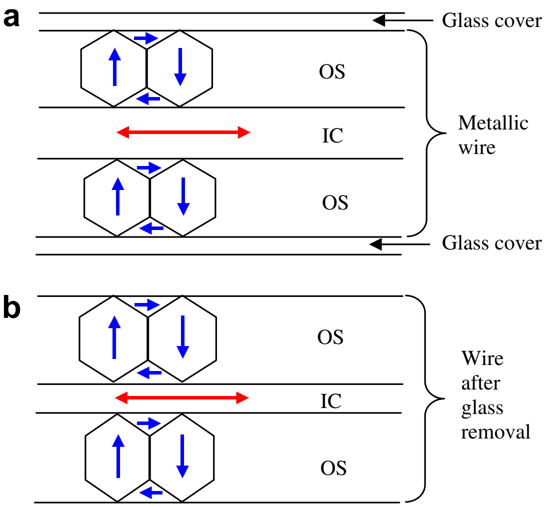

Fig. 15. Schematic illustration of the domain structure in a typical positive-magnetostrictive amorphous glass-covered wire (AGCW): (a) as-cast glass-covered wire and (b) wire after glass removal. OS: Outer Shell; IC: Inter Core (courtesy of H. Chiriac, reproduced with permission from Elsevier [7]).

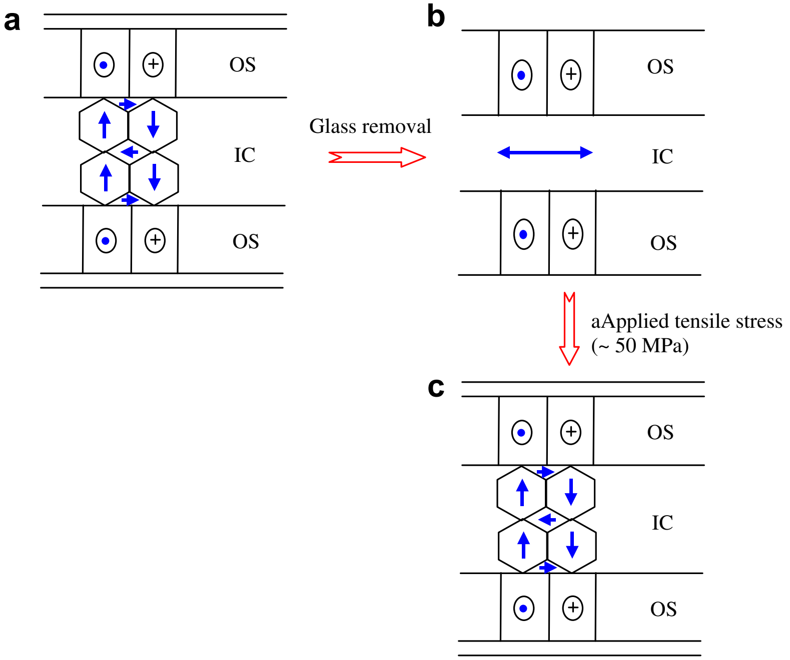

Fig. 16. Schematic illustration of the domain structure in a typical negative-magnetostrictive amorphous glass-covered wire (AGCW): (a) as-cast glass-covered wire; (b) wire after glass removal; and (c) the sample without glass is subjected to an external tensile stress. OS: Outer Shell; IC: Inter Core (courtesy of H. Chiriac, reproduced with permission from Elsevier [7]).

For negative-magnetostrictive AGCWs, the glass removal causes a change in the easy axis of the inner core domains from radial to axial (see Fig. 16a and b), but does not change the outer shell domain configuration, except for an increase in the domain volume. The domain structure of the negative-magnetostrictive AGCWs after glass removal (see Fig. 16b) is similar to that of the negative-magnetostrictive CAWs (Fig. 14). However, the application of a tensile stress (~50 MPa) on the glass-removed wire may cause the return of the original inner core domain structure (see Fig. 16a and c).

Influences of annealing and external stresses on the domain structure and properties of the amorphous wires have been extensively studied [6,7,60,88]. In these studies, annealing under mechanical stresses or magnetic fields has been shown to induce magnetic anisotropies with the corresponding modification of the domain structure.

Finally, for a typical electrodeposited magnetic wire, the domain structure also consists of a radically or circularly magnetised outer shell, but here the inner core is a common non-magnetic conductor, unlike in the case of a rapidly quenched magnetic wire [61–75].

4.1.2. Magnetic ribbons and films

The domain structures of magnetic ribbons and thin films can be characterised similarly to that of the previously discussed magnetic wires. As illustrated in Fig. 17a and b, the domain structure of positive-magnetostrictive amorphous ribbons (e.g., Fe-based alloys) is rather different from that of negative-magnetostrictive amorphous ribbons (e.g.,

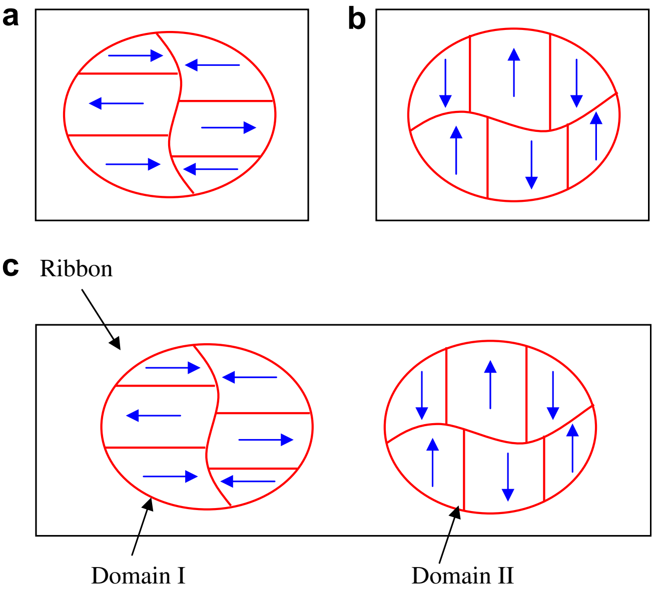

Fig. 17. Schematic illustrations of the domain configurations of (a) positive-magnetostrictive amorphous ribbons, (b) negative-magnetostrictive amorphous ribbons, and (c) annealed amorphous ribbons with positive and nearly zero magnetostriction.

Co-based alloys). The positive-magnetostrictive amorphous ribbons possess a longitudinally oriented domain structure (see Fig. 17a), which may be favorable for an axial LBE [91,92]. On the other hand, negative-magnetostrictive amorphous ribbons such as Co-based alloy ribbons favor a transversely oriented domain structure (see Fig. 17b). This transverse domain structure is favorable for the GMI effect and can be improved by annealing under a transverse magnetic field [93]. No axial LBE is observed in this case.

Annealing treatment of positive-magnetostrictive amorphous ribbons (Fe-based alloys) may lead to the formation of transversely oriented domains (Domain II) in addition to the pre-existing longitudinally oriented domains (Domain I), as illustrated in Fig. 17c, which was observed experimentally [94]. This explains why the soft magnetic properties of Fe-based amorphous ribbons can be significantly improved by proper heat treatments. Further improvement of the magnetic softness can be achieved by annealing in the presence of a transverse magnetic field. It was found that the axial LBE disappeared in the annealed Fe-based amorphous ribbons [92] due to a lack of longitudinally oriented domains (Domain I). The domain structure of a typical sputtered magnetic thin film is understood to be similar to that of a magnetic ribbon. It should be noted that, for a typical sandwich or multilayered film, the domain structure is formed in the ferromagnetic layers, while the non-magnetic conductive layer acts as a conductor only.

4.2. Magnetic properties

4.2.1. Hysteresis loops

Hysteresis loops are one of the key magnetic properties and provide useful information on the magnetic properties of materials. As a result of the different coupling between the internal stress and magnetostriction, different hysteresis behaviors have been observed in materials (e.g., wires, ribbons, and thin films) with positive, negative and nearly zero but negative magnetostriction.

4.2.1.1. Magnetic wires. Magnetic hysteresis behavior of wires can be investigated by measuring either longitudinal or circular hysteresis loops with the application of a longitudinal magnetic field or a circular magnetic field, respectively. However, the change in the interior circumferential magnetisation for wire-shaped samples cannot be measured by conventional magnetometry. It can be observed, however, by filtering out and integrating an inductive voltage signal which appears across the wire due to its magnetisation by a low-frequency current [95]. Due to a simplified experimental setup, the longitudinal hysteresis loop measurement has mainly been employed [6,7,58–60,96]. Fig. 18 displays the typical hysteresis loops of amorphous glass-covered microwires with (a) positive, (b) negative, and (c) nearly zero but negative magnetostriction [59].

For the positive-magnetostrictive AGCWs (e.g., Fe-based wires), the magnetoelastic anisotropies result in axial easy axes, which enhance the shape anisotropy. Consequently, the rectangular hysteresis loop – which exhibits a large axial LBE due to the presence of the inner core axial domain structure in the wire (see Fig. 15a) – is observed (Fig. 18a). When the glass cover is removed, this rectangular hysteresis loop becomes smaller, reducing the LBE effect due to the decrease of the inner core axial domain volume of the wire (see Fig. 15b). This has been experimentally verified [6,88]. Such an LBE effect may be observed even in positive-magnetostrictive AGCWs with a very short length of about 1–2 mm, due to the reduced demagnetising factor resulting from the very small wire diameter to length ratio. This is useful for the development of miniature sensing devices [6]. It was also found that, when an Fe-based AGCW became nanocrystalline under heat treatments, the shape of the hysteresis loop could change from rectangular to flat, with the LBE effect disappearing. In these findings, the coercivity decreased drastically due to the presence of the nanosized α-Fe(Si) grains [60].

For the negative-magnetostrictive AGCWs (e.g., Co–Si–B wires), the mechanical stress gives rise to an easy axis direction perpendicular to the wire axis, therefore leading to an alignment of the magnetic moments in the direction which is perpendicular (circumferential) to the wire axis. As a result, only small hysteresis is observed when an axial magnetic field is applied (see Fig. 18b). It has been shown that these wires do not show LBE, due to the absence of the inner core axial domain structure (see Fig. 16a). It appears that, in the case of the negative-magnetostrictive AGCWs, the glass removal resulted in the LBE [6,7]. This was a direct consequence of the appearance of the inner core axial domain structure due to the increased axial anisotropy (see Fig. 16b). Applying an external tensile stress (~50 MPa) onto the glass-removed amorphous wire could also lead to the suppression of the LBE [7], because of the reappearance of the inner core radial domain structure as in the case of the glass-covered amorphous wire without an applied tensile stress (see Fig. 16c). However, the difference in the magnitude of the internal stresses between AGCWs and CAWs with negative magnetostriction ($\lambda < 0$), which is reflected by the existence of the different inner core domain structures (radial versus axial), can help interpret the different magnetic hysteresis behaviors of these wires.

For the nearly zero and negative-magnetostrictive AGCWs (e.g., Co–Fe–Si–B wires), there is a compensation of induced anisotropies resulting from the balance between the magnetoelastic and magnetostatic energies. Consequently, the hysteresis loop exhibits a

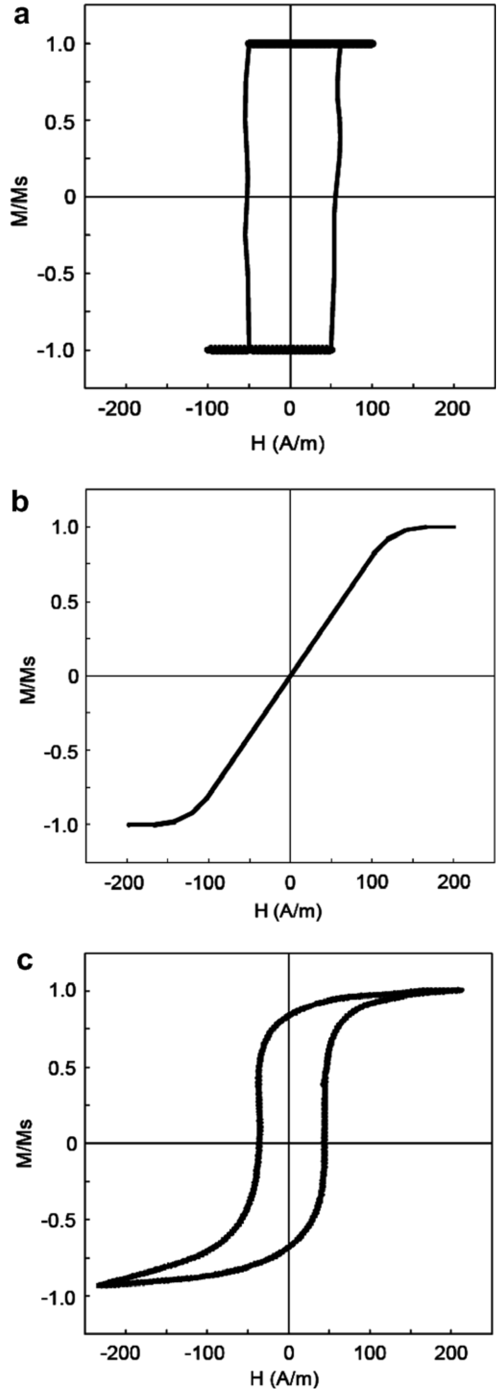

Fig. 18. Typical hysteresis loops of Co–Mn–Si–B amorphous microwires with (a) positive, (b) negative, and (c) negative and nearly zero magnetostriction (courtesy of L. Vladimir, reproduced with permission from Elsevier [59]).

normal shape with no observed LBE effect (see Fig. 18c). It was found that glass removal could result in the appearance of the LBE – which was again suppressed by applying an external tensile stress (~30 MPa), as was the case for the negative-magnetostrictive AGCWs [6,7,60]. The tensile stress needed to suppress the LBE for the nearly zero and negative magnetostrictive AGCW (~30 MPa) is obviously smaller than that for the negative-magnetostrictive AGCW (~50 MPa) [7]. This is attributed to the smaller value of the magnetostriction constant of the nearly zero and negative-magnetostrictive AGCW compared to the negative magnetostrictive AGCW.

4.2.1.2. Magnetic ribbons and films. The hysteresis loops of positive-magnetostrictive amorphous materials with different forms (e.g., ribbon, wire and microwire) have different shapes, due to the difference in the domain structures [6–12]. Both Fe-based amorphous wire and microwire are often found to exhibit the LBE effect. In some case, the LBE effect has also been observed in Fe-based amorphous ribbons [91], due to the evident presence of an axial domain structure (Fig. 17a).

In order to understand the changes in the magnetic hysteresis behaviors of an amorphous ribbon/film upon annealing, the annealing temperature dependence of the coercivity (the shape and magnitude) of Fe-based amorphous ribbon is displayed in Fig. 19 [92]. The shape of hysteresis loop changed significantly with the annealing temperature,

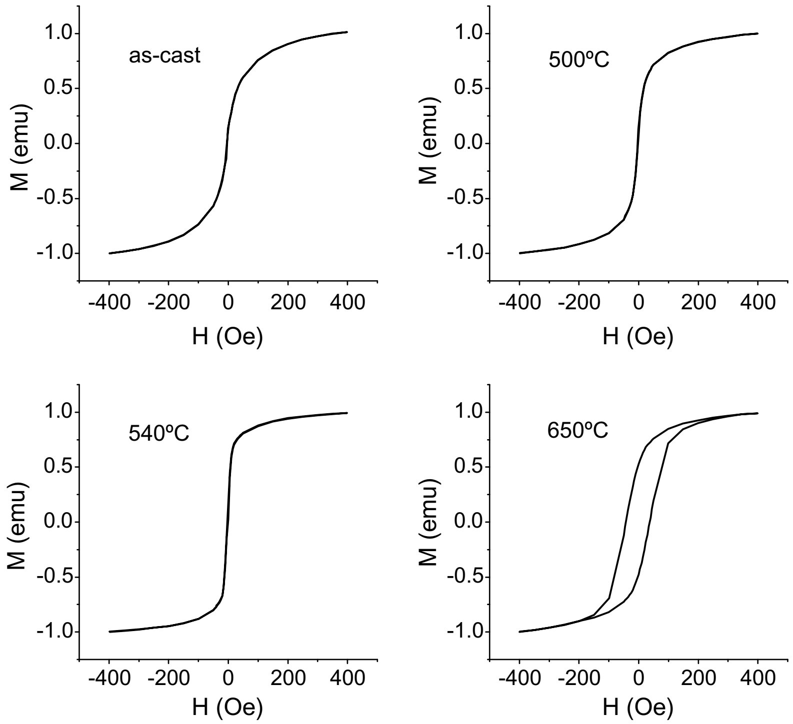

Fig. 19. Magnetic hysteresis loops of Fe–Si–B–Cu–Nb amorphous ribbon after annealing at different temperatures.

which indicates that the anisotropy field was dependent on the annealing temperature. It was found that the coercivity (H_c) decreased with increasing annealing temperature (T_a) up to 540 °C and then increased at higher temperatures. This can be interpreted as follows: when T_a is well below the onset crystallisation temperature (i.e., ~500 °C) the gradual decrease of H_c is a result of structural relaxation, while the decrease of H_c in the temperature range of the first crystallisation stage (~540 °C) is likely to be due to the appearance of nanosized α-Fe(Si) grains where magnetocrystalline anisotropies are averaged out. Annealing over 540 °C causes a rapid increase of H_c, indicating a large degradation of the soft magnetic properties. This coincides well with the microstructural change in the sample. Here, the increase of nanoparticle size could considerably reduce the magnetic exchange coupling in the nanocrystalline material [87]. Furthermore, it was shown that the change in the microstructure of the ribbon sample modified its domain structure [93,94]. For the Fe-based amorphous ribbon, wide and wavy lamina patterns as well as narrow patterns were observed [94]. Such domain structure usually results in the poor soft magnetic property, i.e., the very small value of magnetic permeability.

When an amorphous ribbon was annealed properly (e.g., annealed at 540 °C according to the results given in Fig. 19), it became a nanocrystal with additionally formed broad transverse domains [91,94]. Applying a small magnetic field parallel or perpendicular to the ribbon direction leads to a domain wall displacement of the transverse domains, implying that the easy magnetisation in transverse domain may lie between the longitudinal and transverse directions for the nanocrystalline sample as illustrated in Fig. 17c. It is the presence of the transverse domains that leads to a drastic improvement in the soft magnetic properties as well as the GMI effect of Fe-based nanocrystalline ribbons [91–94]. Annealing over 540 °C caused a strong modification of the broad transverse domain structure due to the microstructural change of the sample [87], and hence resulted in considerable degradation of the magnetic softness as well as the GMI effect [91,94–96].

For negative (e.g., Co–Si–B) and/or nearly zero magnetostrictive (e.g., Co–Fe–Si–B) amorphous ribbons/films, the transverse domain patterns were observed [93]. This is in agreement with the domain configuration suggested in Fig. 17b. Conventional annealing may lead to a fluctuation of the magnetic moments in the transverse direction of the ribbon, while annealing with a transversely applied magnetic field may result in an improvement in the transverse magnetic anisotropy. No magnetic hysteresis was observed in transversely field-annealed Co-based amorphous ribbons [9,10]. In an analogous manner, applying a tensile stress onto a Co-based amorphous ribbon may lead to an increase of the magnetic anisotropy in the transverse direction [97]. All this is reflected by the change in the shape of the hysteresis loop under different applied tensile stresses [4].

4.2.2. Permeability

Magnetic permeability is a key parameter for evaluating the magnetic softness and therefore potential applications of soft ferromagnetic materials. A high value of permeability is required and is related to the specific domain structure of the configuration. In particular, the permeability depends on the sample geometry, stress distribution in the material as well as the internal configuration of magnetisation that might be frequency dependent. It is therefore necessary to evaluate the magnitude of the magnetic permeability and its changes upon the application of an external field such as a magnetic field and a mechanical stress.

4.2.2.1. Magnetic wires. It has been shown that the relative magnetic permeability of a typical vanishing magnetostrictive amorphous wire (e.g., Co–Fe–Si–B amorphous wire) is the largest among the amorphous wires investigated [6,7]. This wire, together with its peculiar domain structure, is ideal for sensor applications based on the GMI effect. Meanwhile, both large negative and positive-magnetostrictive amorphous wires have relatively small permeability. It has generally been found that the glass removal of AGCWs leads to a drastic increase of the relative permeability due to the relief of internal stress. Applying an appropriate tensile stress onto a glass-removed amorphous wire leads to an improvement of the relative permeability [7]. The application of high external stresses usually causes a drastic reduction of the relative permeability. Proper annealing of amorphous wires (e.g., Fe-based alloys) also results in a strong increase of the relative permeability due to the appearance of the nanosized α-Fe(Si) grains [7,87,98].

Applying a magnetic field perpendicular to the wire axis (or in the circular direction) may improve the relative permeability of the wire, because of the increase of the circular component of the permeability due to increased domain wall displacement or the magnetisation rotation process in the circular direction. In contrast to this, applying a magnetic field along the wire axis (or in the longitudinal direction) may slightly increase the relative permeability when the magnetic field is below the switching field (or the anisotropy field), but it strongly reduces the relative permeability at higher fields. Therefore, the maximum value of permeability is often obtained near the switching field or the anisotropy field [7]. Utilising the magnetic field dependence of the permeability, a number of technical applications have been proposed [6–12].

4.2.2.2. Magnetic ribbons and films. Co-based amorphous ribbons/films have a very high relative permeability due to the presence of a transverse domain structure, whereas small values of permeability are often obtained in Fe-based amorphous ribbons/films with a longitudinal domain structure. Annealing the precursor Fe–Si–Cu–Nb–B-based amorphous ribbons can form nanocrystalline materials (the so-called FINEMET) with very high permeabilities that are comparable with those for Co-based amorphous ribbons [79]. In addition, Fe-based nanocrystalline ribbons have higher magnetisation and lower resistivity compared to Co-based amorphous ribbons. Consequently, they have been widely used for high-frequency transformer cores and recently for sensor systems [79,87].

Like amorphous wires, the transversely applied magnetic field may improve the transverse component of ribbon permeability via domain wall motion or a rotational magnetisation process in the transverse direction. In contrast, the longitudinally applied magnetic field may slightly increase the transverse permeability of the ribbon at small fields below the switching field (or the anisotropy field), but it strongly reduces the transverse permeability at higher field strengths. In nanocrystalline samples, the switching field is often very small and close to zero [92].

In order to assess the influence of annealing treatment on the permeability with respect to the magnetisation processes in an amorphous ribbon, the annealing temperature dependence of the permeability of an Fe-based amorphous ribbon was systematically studied and the results are displayed in Fig. 20. It can be seen that the longitudinal permeability resulting from domain wall motion (μ_L^{dw}) decreased with annealing temperature, whereas the longitudinal permeability from rotational magnetisation (μ_L^{rot}) increased with increasing annealing temperature up to 540 °C and then decreased at higher temperatures (see Fig. 20). This coincides well with the hysteresis loop shape, as shown in Fig. 19. The

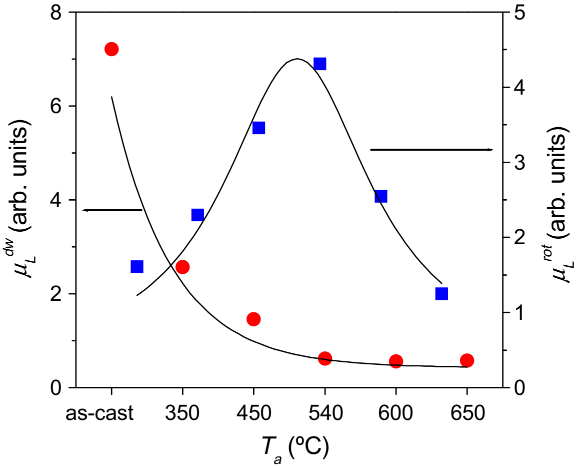

Fig. 20. The annealing temperature dependence of the longitudinal permeability from wall motion (μ_L^{dw}) and from rotational magnetisation (μ_L^{rot}) for Fe–Si–B–Cu–Nb amorphous ribbon.

increase in longitudinal permeability with annealing up to 540 °C is caused by the rotation of magnetic moments [92]. In addition, the dependence of the relative permeability on applied stress has been investigated. It has been found that the applied tensile stress significantly affects the magnitude of the permeability of the amorphous ribbons [79]. In particular, the application of a tensile stress in the direction of the Co-based amorphous ribbons led to an improvement in the transverse component of permeability as well as the transverse magnetic anisotropy, which are desirable for sensors based on the GMI effect.

4.2.3. Magnetisation processes

The magnetisation process of a magnetic material occurs in relation to its specific domain structure. Owing to the specific domain structure of each material (wire or ribbon), either a circular magnetisation process or an axial magnetisation process, or both, can be considered. Understanding the underlying mechanisms of these magnetisation processes helps us in tailoring the material properties for particular engineering applications.

4.2.3.1. Magnetic wires. For a negative (e.g., Co–Si–B) or vanishing magnetostrictive (e.g., Co–Fe–Si–B) amorphous wire, a magnetic field applied perpendicular to the wire axis is an easy axis field with respect to the circumferential anisotropy. Depending upon its magnitude, applying such a field precedes domain wall displacement and magnetisation rotation processes, thus changing the circular component of the magnetisation [99,100]. In contrast, the application of a magnetic field along the wire axis suppresses the circular magnetisation via the domain wall displacement, because this magnetic field is a hard axis field with respect to the circumferential anisotropy. The longitudinal magnetic field leads to a gradual transition from an almost square-shaped hysteresis loop to a linear one as the remagnetisation grows [101]. A domain model was proposed by Landau and Lifshitz [13] to interpret this feature. In the case of magnetic wires, the change in the circular component of the magnetisation is related to that of the impedance. Consequently, the GMI effect is observed because the application of an external magnetic field changes the magnetisation component [4,10].

Unlike the negative and nearly zero magnetostrictive amorphous wires with an outer shell circular domain structure, the positive-magnetostrictive (Fe-based) amorphous wires usually exhibit a small GMI effect because of the presence of the outer shell radial domain structure (Fig. 13). Such a domain structure is not favorable for domain wall displacements in the circular/transverse direction. It has been observed that, when a magnetic field is applied along the wire axis, the pre-existing closure domain structures at both ends will enlarge towards the center of the wire [6,7]. At the switching field, the domain wall from one of the two closure structures de-pins and irreversibly moves towards the other end, giving rise to a sharp change in magnetisation (see Fig. 18a). This is related to the well-known wall propagation mode, in which the wall propagating velocity depends on external factors such as magnetic fields or applied mechanical stresses. This is useful for some technical applications [102–104].

4.2.3.2. Magnetic ribbons and films. The magnetisation processes for negative and vanishing magnetostrictive amorphous ribbons/films are similar to those for the previously discussed negative and vanishing magnetostrictive amorphous wires. In the case of magnetic ribbons/films, applying a magnetic field perpendicular to the ribbon axis precedes a transverse magnetisation process via domain wall displacements at small fields and/or rotation of the magnetic moment at higher field strengths, thus changing the transverse component of the magnetisation [91–94]. This arises from the presence of the transverse domain structure in the ribbons as illustrated in Fig. 17b. The longitudinally applied magnetic field strongly suppresses the domain wall displacement process in the transverse direction and therefore, significantly changes the magnetoimpedance of the wire, resulting in the observed GMI effect [4].

In practice, the transverse domain structure of Co-based amorphous ribbons (see Fig. 17b) favors for the GMI effect more than the longitudinal domain structure of Fe-based amorphous ribbons (see Fig. 17a). When an Fe-based amorphous ribbon becomes nanocrystalline upon the proper annealing treatment, both domain structures (Domain I and II) coexist in the sample as illustrated in Fig. 17c and the magnetisation processes occurring in Domain I are found to be related to those in Domain II and vice versa [91].

4.2.3.3. Applications. Applications utilising the axial and circular magnetisation processes for magnetic wires have been reviewed [6,7,10,60]. The existence of the large LBE in amorphous wires (e.g., Fe-based wires) under longitudinal magnetisation is very useful for a wide variety of technological applications such as pulse generators, position and displacement sensors, non-contact torque sensors, security sensor systems, encoding systems, and detection of biological vibrations in human bodies [6,60]. For applications based on the circular magnetisation processes, the discovery of the GMI effect in vanishing magnetostrictive amorphous wires (e.g., Co–Fe–Si–B) has made these materials ideal for GMI sensor applications [10].

4.3. Mechanical properties

The mechanical properties of the amorphous metals are generally superior to their crystalline counterparts. For instance, the Al-based amorphous alloys have been found to be twice as strong as their commercial crystalline versions [105]. Some Fe-based amorphous alloys display a fracture strength of about 3.5 GPa, which is greater than that obtained in some special steels [106].

Recently, the mechanical properties of several CAWs and AGCWs have been investigated [107–110]. It has been found that these wires have good mechanical properties, and the tensile strength of the AGCWs after glass removal becomes comparable to the CAWs [7,107–109]. The influence of wire diameter on tensile strength has also been studied [54]. The size effect was observed in AGCWs with respect to the difference in the thermal expansion coefficients of the metal and the glass, i.e., the tensile strength increased with decreasing wire diameter when the thermal expansion coefficient of the metal was considerably different from that of the glass cover [54,60,108].

Annealing treatment of amorphous metallic alloys may lead to considerable change in the mechanical properties [109–111]. It has been found that the Fe-based amorphous ribbons show a ductile–brittle transition temperature and the phenomenon of thermal embrittlement. The latter is marked by an increase in the ductile–brittle transition temperature when annealing below the crystallisation temperature [111]. The mechanism of thermal embrittlement is related to the removal of excess free volume and/or to the separation of the homogeneous amorphous phase in the sample upon annealing. For instance, when studying the fracture behavior of Fe-based amorphous glass-covered microwires upon annealing, Zhukova et al. [110] observed a strong drop in tensile yield strength at annealing temperatures near the onset crystallisation temperature (see Fig. 21). The magnitude of the tensile yield strength of the nanocrystalline sample annealed at 600 °C is the largest among all samples annealed, even though it is smaller than that of the as-cast amorphous sample. This indicates that the presence of the nanosized α-Fe(Si) grains and its uniform distribution in the nanocrystalline sample led to a slight improvement of the tensile yield strength. In contrast to this, annealing over 600 °C made the sample extremely brittle, which was attributed to the microstructural change in the sample where a completely crystallised structure was observed [110]. This is consistent with the change in morphology of a fractured Fe–Si–B–Cu–Nb glass-coated microwire in as-prepared and annealed states (see Fig. 22). Effects of different annealing processes (furnace, current and pulse annealing) on the mechanical properties of the Fe-based amorphous wire were also investigated [109].

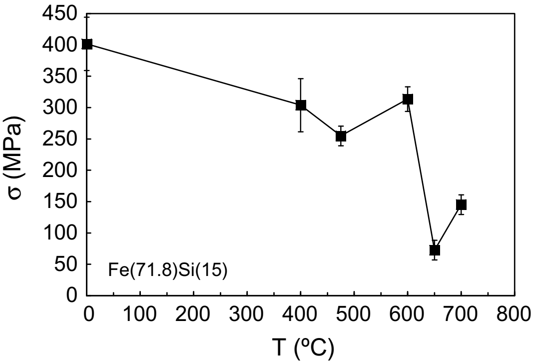

Fig. 21. Dependence of tensile yield on the annealing temperature in a Fe–Si–B–Cu–Nb glass-coated microwire (courtesy of A. Zhukov, reproduced with permission from Elsevier [110]).

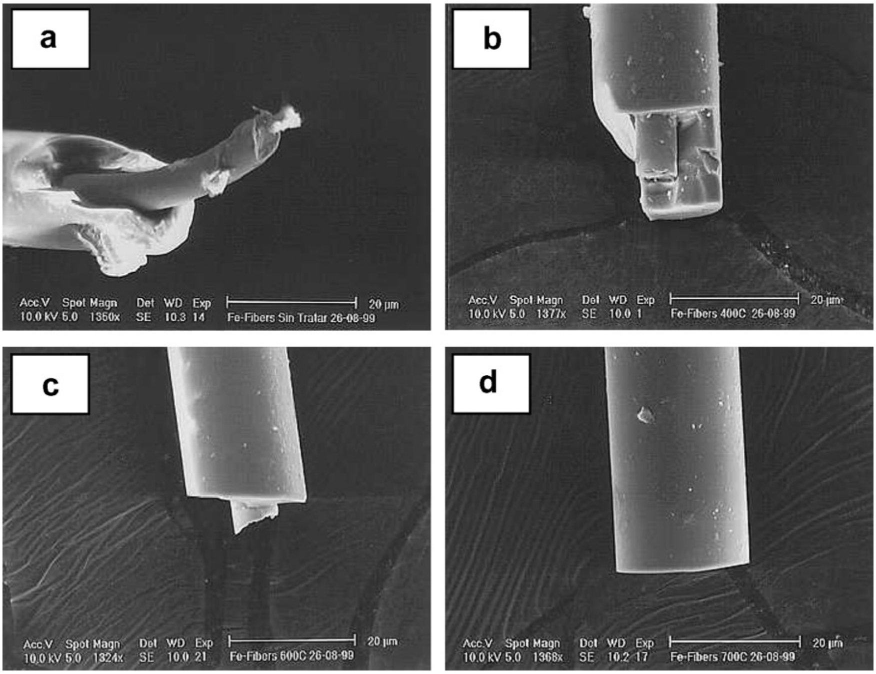

Fig. 22. Micrographs of the fractured Fe–Si–B–Cu–Nb glass-coated microwire samples in (a) as-prepared amorphous state and annealed at (b) 400 °C, (c) 600 °C, and (d) 700 °C (courtesy of A. Zhukov, reproduced with permission from Elsevier [110]).

In practice, owing to their good mechanical properties, amorphous metallic ribbons and wires are useful for applications such as reinforcement in composites and cutting utensils. For example, a reasonable reinforcing effect was observed in polymer–matrix composites containing amorphous metallic ribbons [112]. In this case, instead of using ribbons, the use of amorphous metallic wires (e.g., CAWs and AGCWs after glass removal) may be of much interest. Such wires can also be used as reinforcement for motor tyres [113]. It is believed that Fe-based amorphous wires with a suitable coating (e.g., AGCWs) are the most promising candidates to fulfil the requirements of tyre reinforcement, where high tensile strength, good adhesion to rubber, and excellent resistance to fatigue and corrosion are required.

When considering nanocrystalline ribbons and wires, although excellent magnetic properties can be achieved, embrittlement of these materials may to some extent limit their use in applications, such as sensors. To avoid this problem, the annealing time for an amorphous sample should be as short as possible. Alternatively, it is recommended that the annealed amorphous sample should be as near net-shape as possible in actual devices.

4.4. Electrical properties

In general, the electrical resistivities of the amorphous alloys (wires and ribbons) are higher than that of their crystalline counterparts with the same composition. For example, the resistivity of the Fe–Si–B AGCW was found to be about 20% higher than that of the

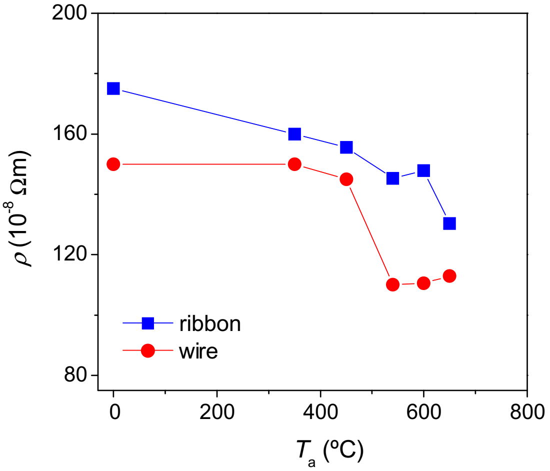

Fig. 23. The resistivity changes with the annealing temperature for Fe–Si–B–Cu–Nb ribbon and wire samples.

corresponding crystalline alloy [7]. This is useful for high-frequency applications, due to the greatly reduced eddy current losses [114]. However, for developing GMI-based sensors, the reduction of resistivity of the amorphous materials is necessary to improve the GMI effect. It is important to note that nanocrystalline materials – which have been synthesised by annealing their amorphous precursors (both wires and ribbons) – usually exhibit much lower resistivity relative to their amorphous counterparts.

Fig. 23 shows the dependence of the resistivity of the Fe-based ribbon and wire on the annealing temperature. It can be seen that the resistivity decreases with the annealing temperature up to 540 °C and then tends to increase at higher annealing temperatures. This is related to the increase of magnetic softness at annealing temperatures below 550 °C and to the microstructural change upon higher temperature annealing, i.e., the appearance of the nanosized α-Fe(Si) crystalline grains after annealing below 540 °C [115]. In this context, the emphasis is based on the measured temperature dependence of the resistivity of the amorphous sample, the structural relaxation and crystallisation processes occurring in these materials, which can be monitored and controlled. Furthermore, the resistivity of amorphous ribbons and wires strongly depends on the alloys' composition and external factors such as magnetic field, mechanical stress, and pressure. Therefore, the magnitude of the alloy's resistivity can be modified either by the addition of chemical elements or by the application of magnetic fields, tensile stress and pressure. In the case of AGCWs, glass removal can lead to a considerable decrease of the wires' resistivity, which is useful for GMI sensor applications.

4.5. Chemical properties

Among the chemical properties often investigated, several works have paid much attention to the wet corrosion resistance of amorphous metallic materials [116–119]. In particular, research has been focused on Fe-based amorphous materials containing metalloid addition in various acids and sodium chloride solutions. Due to the absence of grain boundaries in amorphous metals, the corrosion resistance of these materials is higher than that of conventional crystalline materials, including stainless steels. It has been shown that addition of elements such as Cr and Mo or both into Fe-based amorphous ribbons [116–118], thin films [119] and wires [7] leads to an improvement in corrosion resistance. Pardo et al. [118] have shown that the addition of Cr to Fe–Cr–Si–Cu–Nb–B ribbons, both in amorphous and nanocrystalline states, significantly improves the corrosion resistance of these materials in humid environments with a high SO_2 concentration, whilst retaining their excellent soft magnetic properties.

The superior corrosion resistance of Fe-based amorphous and nanocrystalline materials is useful for their application in chemical environments, where they can be used for protection of other materials [118]. For example, Fe–Cr–P–C amorphous ribbons are used as the active element in electromagnetic filters to remove rust from water, their high corrosion resistance ensuring a long life of the filter elements [117]. Further information on the corrosion resistance properties of typical amorphous metals as well as their applications can be found in Ref. [116].

5. Influence of measuring parameters on GMI

5.1. Alternating current

It is generally accepted that the circular (or transverse) magnetisation process takes place due to the ac circular magnetic field created by an alternating current (ac). Meanwhile, the change in impedance is directly related to this magnetisation process [4–10]. Therefore, a dependence of the impedance on the ac exists, according to Eq. (2.2). The higher the amplitude of the ac (I_m), the larger the impedance (Z) obtained. It has been theoretically predicted that for a double-peak (DP) feature of GMI in an amorphous wire, the magnetic field (H_m) at which the value of Z reaches a maximum should decrease with increasing amplitude of the ac [23].

In practice, GMI curves exhibit a DP behavior for low currents where only reversible wall motion takes place, but this changes to a single-peak (SP) at high currents related to circular coercivity [8,120–124]. This can be seen in Fig. 24 for a Co-based amorphous wire [8]. When investigating the dependence of GMI on ac, Aragoneses et al. [123] found different dependences in different materials (e.g., amorphous microwires/wires, nanocrystalline ribbons). For an amorphous $Co_{68.5}Mn_{6.5}Si_{10}B_{15}$ microwire, when I_m was increased the GMI effect increased until $I_m = 2.8$ mA and then decreased at higher values of I_m. This is consistent with what was reported by Vazquez et al. [120] on Co-based amorphous wires. With increasing I_m, the GMI effect decreased gradually for an $(Fe_{0.94}Co_{0.06})_{72.5}$- $B_{15}Si_{12.5}$ amorphous wire, while it sharply increased for a $Fe_{73.5}Si_{13.5}B_9Nb_3Cu_1$ nanocrystalline ribbon [123]. In these examples, the observed effect of driving current can be explained by considering the tensor character of the magnetic permeability, and the effect was attributed to the components of that tensor which are responsible for the transverse magnetic anisotropy [124]. The different dependences of GMI on driving ac reported in [120,123] are also believed to be caused by the difference in the domain structures of investigated samples.

For an Fe-based nanocrystalline ribbon, the GMI effect increased and H_m decreased with increasing I_m (see Fig. 25). Due to the saturation of the transverse magnetisation, the GMI profile became saturated when I_m was larger than 65 mA. In fact, the ac at which the GMI profile becomes saturated also depends on the domain structure of the samples

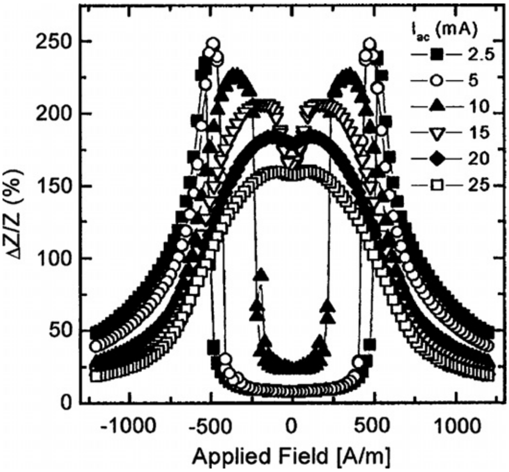

Fig. 24. GMI for a Co-base amorphous wire with induced circular anisotropy. Evolution from double-peak (DP) to single-peak (SP) feature with increasing current is observed (courtesy of M. Vazquez, reproduced with permission from Elsevier [8]).

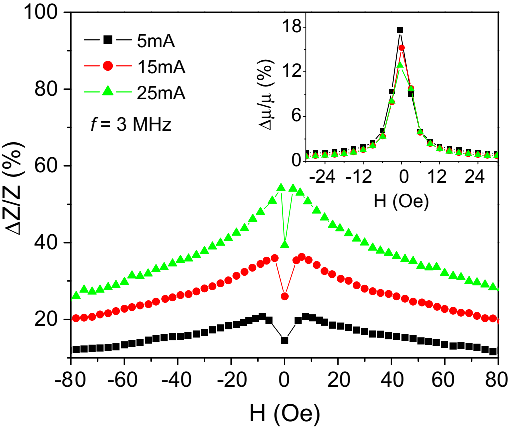

Fig. 25. Magnetic field dependence of the GMI ratio ($\Delta Z/Z$) and the longitudinal permeability ratio ($\Delta\mu/\mu$) at different driving currents.

[120,124]. The increase of the GMI ratio is correlated to the decrease of longitudinal permeability ratio for the Fe-based nanocrystalline ribbon (see the inset of Fig. 25). Furthermore, it has been shown that whenever GMI measurements are conducted, attention should be paid to the proper selection of the driving current amplitude, because non-linear effects can occur at relatively low current levels [124].

5.2. Magnetic field

To measure GMI effect, a dc magnetic field is usually applied parallel to the ac along the longitudinal direction of the sample. This is known as the longitudinal GMI effect

[4,10]. As discussed previously in Section 2, at a given frequency, the application of a dc magnetic field (H_{dc}) changes the circular or transverse permeability μ_T and hence the magnetic penetration depth δ_m that in turn alters the magnetoimpedance until the value of δ_m reaches the radius of the wire (t) or the half thickness of the sample (a). Consequently, the GMI effect increases to a maximum value when the applied dc field is increased as typically displayed in Fig. 26. In reality, the applied dc magnetic field (H_{dc}) may compensate the axial magnetic anisotropy when H_{dc} reaches the switching field of the sample [10,23,125,126]. At this field, the quasifree magnetisation responds quickly to the external oscillating magnetic field and gives rise to a large transverse permeability [125]. Since the value of the switching field is actually very small in nanocrystalline samples, the maximum value of GMI is observed at nearly zero field ($H_{dc} \sim 0$) for low frequencies ($f \leqslant 1$ MHz) [126]. The GMI profile also shows an SP behavior in this frequency range (see Fig. 26). When the dc magnetic field exceeds the switching field, the transverse permeability decreases due to the unidirectional magnetostatic anisotropy caused by H_{dc}. Therefore, with increasing dc magnetic field, the skin depth increases and consequently results in an increase of the GMI effect [125].

When studying the effects of applied dc fields on domain wall magnetisation processes at low frequencies in Fe-based nanocrystalline ribbons, Qin et al. [127] found that a small longitudinal dc field helped the domain wall unpin from the pinning field. A large longitudinal dc field increased the pinning field and damped the domain wall motion, while a transverse dc field had little influence on the pinning field. At high frequencies ($f >$ 1 MHz), GMI profiles showed a DP characteristic (see Fig. 26) due to the change in the switching and anisotropy field of the sample with increasing frequency [10]. It is the increase of the switching and anisotropy field with frequency that in turn causes the DP behavior in GMI profiles, together with a shift of the GMI peak towards a higher value of H_{dc}, when the frequency is increased [10,125]. However, the magnetic field dependence of GMI has been correlated to the magnetic field dependence of the circular/transverse permeability [4,5,10]. Such SP and DP features of GMI are determined by the relative contribution from the domain wall motion and magnetisation rotation processes to the

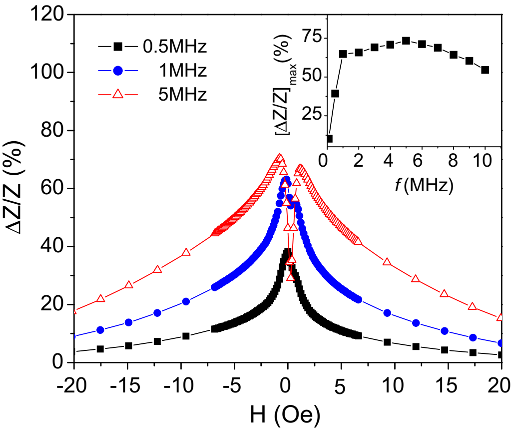

Fig. 26. The dc magnetic field dependence of $\Delta Z/Z$ for the nanocrystalline $Fe_{71}Al_2Si_{14}B_{8.5}Cu_1Nb_{3.5}$ ribbon at various frequencies. The inset shows the frequency dependence of $[\Delta Z/Z]_{max}$.

circular/transverse permeability [4,128]. Complex domain structures and distribution of local anisotropies in actual materials can also be additional causes of the complicated dependence of GMI on dc magnetic field [129–132].

It is important to note that using the magnetic field dependence of the GMI ratio, one can determine whether a magnetic material is syuitable for sensor applications. This is also known as the sensitivity of GMI to the applied field (i.e., $\xi = 2(\Delta Z/Z)_{\max}/\Delta H$, where ΔH is equal to the full width at half maximum of GMI curve).

5.3. Measuring frequency

According to Eqs. (2.6)–(2.9), GMI and its behavior depend strongly on measuring frequency [4,5,10], and such frequency-dependent GMI features have been experimentally studied in a wide range of frequencies up to several GHz in different materials [10,133–137].

It has been shown that, with increasing frequency, the magnetisation process via domain wall displacement relaxes at relatively low frequencies ranging between 0.1 and 1 MHz in amorphous wires [27] and ribbons [28]. For amorphous glass-covered microwires, the permeability spectra showed dispersion laws at higher frequencies [4,7]. At low frequencies $f < \sim 0.1$ MHz ($a < \delta_m$), the maximum value of GMI, defined as $[\Delta Z/Z]_{\max}(\%)$, is found to be relatively low due to the contribution of the induced magneto-inductive voltage to magnetoimpedance [4,10]. In this case, GMI features can be interpreted on the basis of the quasistatic models [11]. In the frequency range of 0.1–10 MHz, where most GMI measurements have been conducted, with increasing frequency, $[\Delta Z/Z]_{\max}(\%)$ first increases up to a maximum and then decreases and even changes sign [137]. As a typical example displayed in the inset of Fig. 26, when 1 MHz $\leqslant f \leqslant$ 5 MHz ($a \approx \delta_m$), the skin effect is dominant, and a higher $[\Delta Z/Z(\%)]_{\max}$ was found. Beyond $f = 5$ MHz, $[\Delta Z/Z(\%)]_{\max}$ decreases with increasing frequency. It is believed that, in this frequency region ($f \geqslant$ 5 MHz), the domain wall displacement was strongly damped owing to eddy currents, thus contributing less to the transverse permeability, i.e., a small $[\Delta Z/Z(\%)]_{\max}$. It should also be noted that the magnetoimpedance increases with frequency because the impedance is proportional to $(\omega\mu_T)^{1/2}$ even in the case of decreasing transverse permeability at high frequencies. Despite this, the frequency at which the maximum GMI value is obtained depends strongly on the samples' dimension. It has also been found that GMI usually reaches its maximum value at higher frequencies for amorphous microwires than for amorphous wires and ribbons [133–137]. At frequencies above 10 MHz, only the spin rotation mechanism occurs and the effective permeability is small [135,136]. The eddy current and domain models are valid for interpreting basic GMI features in the frequency range of 0.1–100 MHz [5,23]. At higher frequencies, where ferromagnetic resonance can occur [136,137], GMI features were successfully explained by the electromagnetic and conductivity-exchange models [14,15]. Furthermore, with increasing frequency, the low-frequency SP behavior may become DP-like as a consequence of the frequency dependence of permeability (see the inset of Fig. 26) [10,23]. GMI curves may also become broader with increasing frequency (see Fig. 26) [137]. When GMI curves become broader, one can adapt the model developed for transverse biased permeability in thick ferromagnetic films. It is the combination of eddy current damping, ripple field and anisotropy field that gives rise to the peak in permeability as well as the broadening of permeability curves [138]. This can explain the broadening of GMI curves at high frequencies.

From an experimental perspective, one should note that most GMI measurements have been performed at measuring frequencies up to only 10 MHz. This is due to the fact that, in this frequency range, the voltage–current measurement technique that gives a direct measurement of the transport properties of the sample can be easily employed. At higher frequencies, both voltage and current are not always quantitatively well defined and the classic measurement technique fails. To overcome this problem, another technique based on the *S*-parameter measurement of a transmission line section by means of an automatic vectorial network analyser has recently been exploited to measure the GMI effect in the microwave region of soft magnetic amorphous samples.

5.4. Measuring temperature

A thorough knowledge of the measuring temperature dependence of GMI is important and necessary, both from a fundamental and practical perspective. However, only a few works have studied the influence of the measuring temperature on GMI in materials such as Co-based amorphous wires [139], Co-based amorphous ribbons [140–143] and Fe-based nanocrystalline ribbons and wires [144,145].

In general, the GMI effect first increases with increasing measuring temperature and reaches a maximum value near the Curie temperature of the material, then finally decreases at higher temperatures [139,140]. The magnitude of GMI measured at room temperature was about three times larger than that measured at a lower temperature (~10 K) [140]. This tendency is in contrast to that previously reported for GMR materials [3]. The Co-based ribbons with cryogenic treatment possessed a larger value of the GMI effect after annealing [141]. The decrease of GMI at temperatures above the Curie point was attributed to the collapse of the magnetic coupling in the material [144]. The temperature dependence of GMI has been related to that of the circular permeability for amorphous wires [139], and to that of the effective permeability for amorphous ribbons [142]. Because the magnetic permeability is sensitive to temperature, the GMI changes rapidly

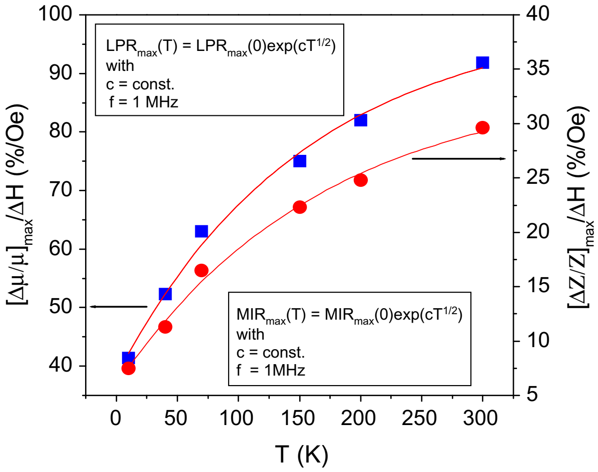

Fig. 27. The temperature dependence of $[\Delta\mu/\mu]_{max}/\Delta H$ and $[\Delta Z/Z]_{max}/\Delta H$ at a frequency of 1 MHz for the annealed $Co_{70}Fe_5Si_{15}Nb_{2.2}Cu_{0.8}B_7$ amorphous alloy. The solid line indicates the fit by the formula shown.

as a function of temperature (see Fig. 27). The exchange energy between magnetic moments at a low temperature is larger than that at a high temperature [144]. Therefore, the circular motion of magnetic moments will be frozen at a low temperature resulting in lower permeability and smaller GMI values [139,145]. Indeed, such investigations provide useful information on the magnetisation dynamics in the circular direction for wires [139,145] and/or in the transverse direction for ribbons [141–143]. Furthermore, it has been shown that appropriate annealing treatment of amorphous ribbons can improve the thermal stability of GMI-based sensors operating at different temperatures [143]. In this respect, nanocrystalline GMI materials are more appropriate than amorphous ones.

6. Influence of processing parameters on GMI

6.1. Effect of glass coating on GMI

The influence of glass coating on the domain structure and magnetic properties of amorphous wires have been discussed in Refs. [6,7,10,60]. This section will focus on describing the influence of glass coating on the GMI profile in amorphous and nanocrystalline wires. The effects of removing the glass coating on the GMI profile are also discussed.

6.1.1. Amorphous wires

Fig. 28 shows the magnetic field dependence of the GMI profile measured at different frequencies, for nearly zero magnetostrictive Co-based amorphous microwires (a) before and (b) after glass removal. As one can see from Fig. 28, over the entire measured frequency range, the GMI effect decreased considerably for the microwire after glass removal. This is likely to be a consequence of the glass removal causing a reduction of circumferential permeability in the microwire and hence a reduction of the GMI effect [146–148]. At low frequencies ($f = 0.1$–1 MHz), the GMI effect is obtained in the glass-covered sample (see Fig. 28a), but not in the glass-removed sample (see Fig. 28b). This is somewhat different to that reported in [7], where no GMI effect was observed in either Co-based glass-covered or glass-removed wires. This probably arises from the fact that, in the frequency range ($f < 1$ MHz), the circumferential permeability is relatively large and the skin effect is noticeable in the glass-covered microwire [149].

At higher frequencies (1 MHz $< f$), the GMI effect is obtained in the wire both before and after glass removal, and it increases with increasing frequency up to 10 MHz. Here, the skin effect is dominant and the magnetoimpedance is proportional to the square root of the circumferential permeability and frequency. More noticeably, at the highest frequency of 10 MHz, a DP behavior is observed in the glass-covered microwire, while a SP behavior remains for the glass-removed microwire (see Fig. 28). This can be understood by accounting for the less sensitive circumferential permeability of the microwire after glass removal. Concerning the different GMI features of Co-based conventional and glass-covered/glass-removed wires with the same composition, a detailed analysis can be found in Ref. [7]. It was shown that the largest GMI effect was obtained for the conventional wire at relatively low frequencies, but for the glass-removed wire, this was found at high frequencies due to the high value of magnetic permeability retained. The largest GMI effect was achieved in the glass-covered wire only in a relatively narrow and intermediate frequency range ($f = 4$–6 MHz) [7]. Furthermore, it has been shown that

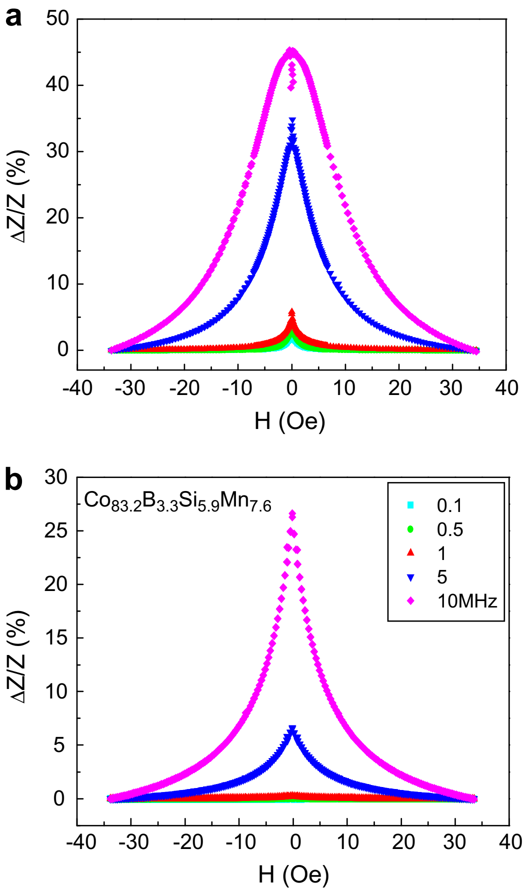

Fig. 28. Magnetic field dependence of GMI profile measured at different frequencies for the Co–B–Si–Mn amorphous microwire: (a) before and (b) after glass removal.

the thicker the glass coating, the larger the stress and the higher the level of induced circumferential anisotropy. Therefore, the magnetic field at which the GMI peak is observed reduces with the thickness of glass coating applied [146–148]. In fact, the coating not only changes the anisotropy distribution, but also reduces the magnitude of the magnetic permeability. Consequently, the GMI effect is smaller for a wire with a thicker glass cover.

In the case of positive-magnetostrictive glass-covered amorphous wires/microwires (e.g., Fe-based amorphous glass-covered alloys), a relatively small MI effect was observed [7,16,98]. For instance, a small MI effect (~1%) was obtained in the Fe-based glass-covered amorphous wire, this was attributed to the high positive magnetostriction of the sample ($\lambda \sim 25 \times 10^{-6}$) that led to a domain structure with axially magnetised inner core and radically magnetised outer shell through magnetomechanical coupling with internal stresses. After the glass cover was removed, a higher MI effect (~5%) was achieved [98]. This was attributed to the stress relief caused by the glass removal [7]. Such different behaviors of GMI observed in Co-based and Fe-based amorphous wires can be understood through the difference in their domain structure determined by the sign of magnetostriction of the sample.

6.1.2. Nanocrystalline wires

Many previous investigations have reported on the influence of glass coating on the GMI profile in nanostructured wires/microwires [16,98,150,151]. Such nanostructured wires (or nanocrystalline magnetic wires) were usually obtained by proper annealing of their precursor as-cast amorphous wires. Both Co-based negative and Fe-based positive magnetostrictive nanostructured wires were investigated [98,151], with much attention being paid to an Fe-based nanostructured wire, where a much improved GMI effect was obtained after glass removal [16,98,150]. For example, the GMI ratio of the FeSiBCuNb nanostructured wire reached a value of about 28% after glass removal [98], which is much larger than that of the glass-covered sample (~5%). Because the Fe-based nanostructured wires without glass cover are magnetically softer than the glass-covered ones, a much more sensitive GMI response was observed in these samples [16,98]. Furthermore, it was found that the GMI ratio of the FeSiBCuNb nanocrystalline wire without glass cover was even larger than that of CoFeSiB amorphous wires after glass removal (~20%), because of the fact that the Fe-based nanocrystalline wire without glass cover was magnetically softer due to its vanishing magnetostriction [98,146]. Another feature to be noted is that the frequency at which the maximum GMI value was obtained was often lower in Fe-based nanocrystalline wires without glass cover than in both Fe-based nanocrystalline wires with glass cover and Co-based amorphous wires without glass cover [98]. This probably results from the lowest value of resistivity observed in the Fe-based nanocrystalline wire without a glass cover [16]. These results indicate that the Fe-based nanocrystalline wires with glass-cover removed can be competitive candidate materials for high-performance sensor applications.

6.2. Effect of sample geometry on GMI

6.2.1. Sample length

The influence of the sample length on the magnetisation processes and GMI effect has been investigated [152–156]. It was found that the spontaneous magnetic bistability observed in a Co-based amorphous wire was lost when the sample length became less than a critical length [152,153]. The critical length was smaller for Co-based amorphous wires than for Fe-based amorphous wires [152]. The loss of magnetic bistability can be attributed to the influence of shape anisotropy, where for short wires, the demagnetising field becomes large enough to destroy the original domain structure of the sample. In a recent work, Vazquez et al. [154] analysed in detail the influence of sample length on the magnetic properties (e.g., coercivity, susceptibility) and GMI of a Fe-based nanocrystalline wire. It was found that, with decreasing wire length, the coercivity increased, the susceptibility decreased, and the GMI effect consequently reduced [154]. This phenomenon has been attributed to the formation of closure domain structures near the ends of the wire due to the demagnetising field [152–156]. It was the significant modification in the domain structure near the ends of the sample that led to different GMI features with respect to the change of sample length [154,155]. It was also found that the field sensitivity of GMI was reduced in samples where such a “border effect” was large enough [154]. However, Phan et al. [156] recently observed that the decrease of length (l) of a Co-based

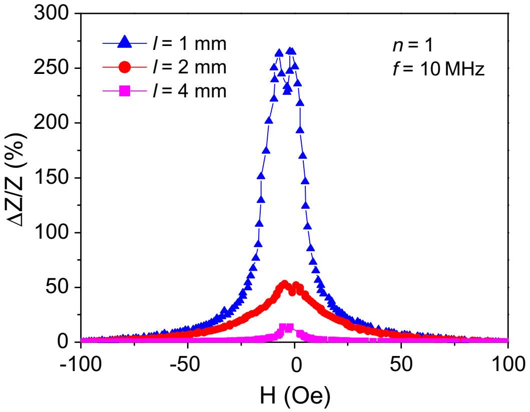

Fig. 29. GMI profiles measured at $f = 10$ MHz for a single microwire with varying length ($l = 1, 2, 4$ mm).

microwire (e.g., AGCW) resulted in a strong increase of the GMI ratio as shown in Fig. 29. It can be seen that at the highest measured frequency of 10 MHz, the GMI ratio increased from 15.5% to 268% as the microwire length decreased from 4 to 1 mm, respectively. This can be attributed to the decrease of electrical resistance from 19.7 to 3.1 Ohm.m with decreasing length from 4 to 1 mm, respectively. This finding is of practical importance because it shows that the ferromagnetic microwires or composites containing these microwires are ideally suited to designing miniaturised magnetic sensing devices which are compatible with biological systems for health monitoring purposes. This difference is likely to be a result of the "border effect" being larger in the normal wire [154] than in the microwire [156]. These results suggest that such geometrical effects should be considered carefully whenever GMI results are analysed and reported.

6.2.2. Sample thickness

Efforts have been made to investigate the influence of sample thickness on the GMI effect in different materials, including amorphous wires [157,158,67], layered and multilayered films [81,82,84,159], amorphous ribbons [160–162], and layered composite wires [62,64,67,68]. A typical example of the wire-diameter dependence of the GMI effect is displayed in Fig. 30. It can be seen that the largest GMI value was obtained in samples with an optimal diameter [157,158,67]. Due to the skin effect, the maximum value of GMI shifted to a lower frequency for the thicker wire [157]. It is the transformation of the longitudinal domain structure in the inner core of hard-drawn wires to a circular domain structure that resulted in the increase of the GMI effect in hard-drawn wires [158]. Both circumferential and longitudinal axial anisotropies depend on the radial distance of the wire [158,67], and this in turn causes the wire-diameter dependent GMI features [62,68].

Similar behaviors were also observed in layered and multilayered films [81,82,84] and amorphous ribbons [160–162]. The GMI ratio increased with increasing thickness of the conducting spacer layer (Cu or Ag) [81,82]. When the film width was less than a critical value, which depends on the transverse permeability and the layer thickness, the flux leakage through the conductive layer resulted in a considerable drop in the GMI ratio [82].

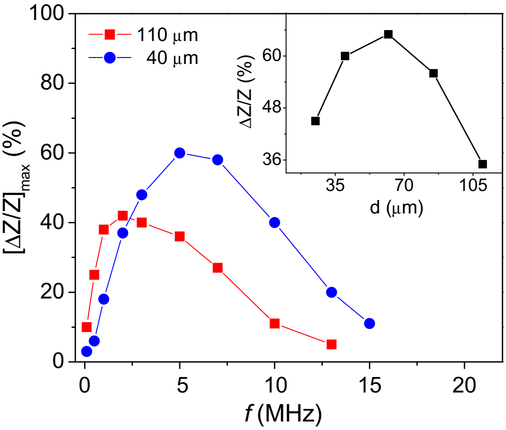

Fig. 30. Frequency dependence of the maximum GMI effect $[\Delta Z/Z]_{\max}$ for Co–Fe–Si–B wires with different diameters. The inset shows the change of the GMI effect ($\Delta Z/Z$) with the wire diameter, measured at $f = 5$ MHz.

With increasing film thickness, a variation from an SP feature to a DP one occurred [159]. This was attributed to the different anisotropy axes induced by the strain in the multilayers [82].

6.2.3. Sample surface

It has been shown that, in the case of a large skin effect, the surface roughness becomes important [10,11]. This is not only because the skin depth may become smaller than the surface irregularities, but also due to stray fields, which appear on the rough surface and cause a considerable reduction in the GMI magnitude. Indeed, the GMI effect was significantly improved in chemically thinned and polished magnetic amorphous ribbons [160], because the polishing resulted in a smoother ribbon surface thereby reducing the effective anisotropy as well as making the sample magnetically softer. This has recently been experimentally verified by Le et al. [163] when studying the GMI effect and surface morphological developments in the nanocrystalline $Fe_{73.5-x}Cr_xSi_{13.5}B_9Nb_3Au_1$ ($x = 1$–5) ribbons. Herein, the surface morphology of these samples was studied by atomic force microscopy (AFM). It was found that the GMI ratio reached a maximum in the sample with the smallest surface roughness (see Fig. 31). The GMI ratio strongly decreased in samples with large surface roughness. Therefore, it is recommended that for rapidly quenched magnetic ribbons, the sample surfaces should be polished before they are used for making sensors. Regarding the effect of sample surface, electrodeposited wires and films usually have higher quality surfaces relative to rapidly quenched wires and ribbons, and a higher GMI response is consequently achieved [61–77].

6.2.4. Sample axes

The influence of sample axis direction on the GMI effect of Co-based amorphous ribbons and films has been studied [164,165]. Kurlyandskaya et al. [165] investigated the angular dependence of the GMI profile for the angles $0 \leqslant \alpha \leqslant 90°$, where α is the angle between the long side of the ribbon and the external magnetic field. The results indicated that the GMI behavior remained stable for angles up to 30°, revealing that the field sensitivity of GMI-based magnetic sensors is not critically limited by the orientation of the

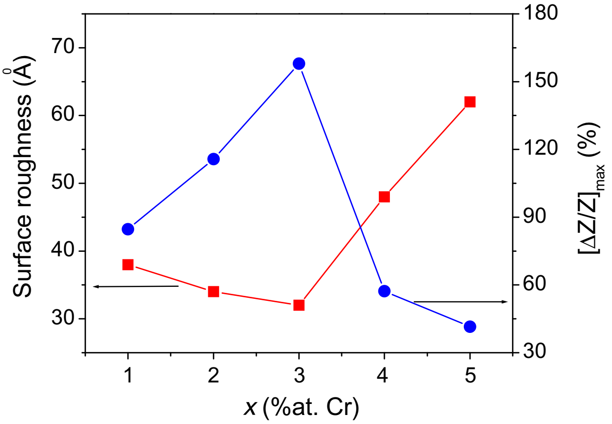

Fig. 31. The dependence of the maximum GMI measured at 2 MHz and the surface roughness on Cr-doped content for nanocrystalline $Fe_{73.5-x}Cr_xSi_{13.5}B_9Nb_3Au_1$ (x = 1–5) ribbons (courtesy A.T. Le).

applied magnetic field. However, the orientation of the applied magnetic field at larger angles ($\alpha \geqslant 30°$) resulted in a significant reduction in the field sensitivity of GMI and hence in the sensitivity of the GMI sensor. This warrants careful examination in the design of GMI sensors when using magnetic wires or ribbons as sensing elements.

6.3. *Effect of annealing on GMI*

The GMI effect can be improved when an amorphous ferromagnetic material is subjected to proper heat treatments such as an annealing treatment. Effects of different annealing procedures on the GMI effect in amorphous magnetic wires/microwires and ribbons are discussed below.

6.3.1. *Conventional annealing*

Conventional annealing is a process where samples are simply heated in an air/vacuum furnace for a given time. It has been shown that conventional annealing causes a considerable reduction in the GMI effect for Co-based amorphous wires/microwires [151] and ribbons [166] due to the fluctuation of the circumferential/transverse anisotropy in the circumferential/transverse direction of the wire/ribbon. However, it causes a drastic improvement in the GMI effect for Fe-based amorphous wires [16,98,150] and ribbons [87,109,167–172], resulting from the improved magnetic softness of the samples after annealing. Conventional annealing of amorphous ribbons can relieve the quench-in strains, reduce the transverse magnetic anisotropy and therefore reduce the GMI effect, even though the magnetic permeability is increased. Therefore, Sommer and Chian [166] claimed that a high permeability did not necessarily lead to a large MI effect. However, this statement is not entirely true, since the MI effect was only studied at relatively low frequencies (~100 kHz) [166]. The situation would be different if MI measurements were carried out at higher frequencies (1–10 MHz) where higher permeability is needed for a larger MI effect [10].

Indeed, Phan et al. [142,173] recently revealed that a suitable conventional annealing treatment (i.e., relatively low annealing temperature ~300 °C and short annealing time

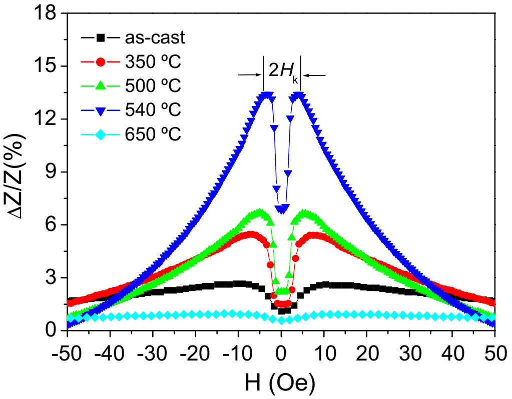

Fig. 32. GMI profile at $f = 10$ MHz in Fe–Si–Nb–Cu–B as-cast and annealed alloys.

~25 min) of Co-based amorphous ribbons resulted in a significantly improved GMI effect from ~50% to ~70% in the frequency range of 1–10 MHz. Suitable annealing treatment is also believed to lead to the relief of internal stress while retaining the orientation of the magnetic moments in the transverse direction of the ribbon [173]. Furthermore, it was found that the magnetic softness (e.g., magnetic permeability, saturation magnetisation) increased and the resistivity decreased in an Fe-based amorphous wire/ribbon when subjected to proper conventional annealing [16,98]. It is the increase in magnetic softness and the decrease in resistivity that results in the much improved GMI effect [16,98,150,167–172]. In this context, the magnetic softness may be used as a second criterion in selecting an appropriate material for GMI-based sensor applications [98]. The correlation between the microstructure and magnetic properties, including the GMI effect, in Fe-based nanocrystalline ribbons has been clarified [87]. Fig. 32 shows the change of GMI effect with annealing temperature. A decrease of the anisotropy field (H_k) and an increase of the GMI with increasing annealing temperature up to 540 °C were observed and attributed to the increase of the magnetic permeability and the decrease of the coercivity, whereas the opposite tendency was found for the sample annealed above 600 °C, which is likely to be a result of the microstructural change caused by high-temperature annealing [73]. These results show the usefulness of using the GMI effect to monitor the structural changes that occur in amorphous ferromagnets during annealing and especially during specific annealing for nanocrystallisation [16,87,98,150]. It has been shown that the magnitude of GMI for the Fe-based nanocrystalline materials (both wires and ribbons) is comparable with that for the Co-based amorphous ones. This makes them useful for practical sensor applications.

6.3.2. Field annealing

The presence of a dc magnetic field along the sample axis during annealing (the so-called field annealing method) led to a further improvement in the GMI effect when compared to conventional annealing [133,166,174,175]. For Co-based amorphous ribbons, the GMI effect was found to be significantly improved in samples subjected to transverse field annealing, while it was almost suppressed upon longitudinal field annealing [166]. A large hysteresis in the GMI curves with respect to increasing and decreasing dc magnetic fields was observed in the case of transverse field annealing. This hysteresis occurred at magnetic fields smaller than the anisotropy field and is probably related to the irreversible magnetisation process due to domain wall displacement. In the case of field-annealed Fe-based amorphous ribbons, the easy magnetisation direction was found to be along the ac driving current direction as well as the external dc magnetic field [175]. A large GMI effect was consequently achieved in the field-annealed sample but not in the zero-field-annealed sample. It is worth mentioning that the field annealing not only led to an increase of the GMI ratio, but also improved the magnetic response of the GMI [175]. This is beneficial for GMI-based sensor applications.

6.3.3. Current annealing

6.3.3.1. Joule heating. Joule heating is a method that allows a sample to be heated directly by the action of a dc current flowing along the sample axis for a certain time [129]. Low-current densities have been exploited to perform annealing at temperatures well below the crystallisation temperature and the Curie temperature of the investigated sample. During Joule heating, the dc magnetic field generated by the dc current allows a thermal treatment under the self-generated external circular magnetic field. Therefore, this method is useful for inducing additional circular/transverse magnetic anisotropy in amorphous ferromagnetic wires/microwires [69,129,135,176–179] and ribbons [179,180], and consequently, providing an improved GMI effect. For a Co-based amorphous microwire, Joule heating without applied stress can produce a short-range order relaxation and hence improve the soft magnetic properties [129]. Consequently, the GMI effect can be optimised when the applied annealing current density is properly adjusted [129,176–179]. With increasing annealing current density, the GMI ratio first increased due to the relief of internal stress caused by heating [129], while the decrease of the GMI ratio after completion of the annealing process was attributed to the microstructural change in the sample [69]. More interestingly, the GMI ratio measured at a frequency of 15 MHz reached a maximum value of about 600% and the magnetic response of 320%/Oe under specific current annealing (i.e., 10 min annealing with an applied dc current of 70 mA) [129]. This value of GMI is about 10 times larger than the maximum value reported so far for glass-coated microwires, and is ideal for high-performance magnetic sensor applications. When investigating high-frequency GMI features in Joule-heated Co-based amorphous ribbons and wires, Brunetti et al. [179] showed that the GMI variation was more pronounced in the as-cast wire than in the as-cast ribbon. This is likely to be due to the higher value of circular permeability compared to that for the transverse permeability [129,180]. The difference in the magnitude of the GMI effect between as-cast ribbon and wire observed at low frequencies ($\sim$500 MHz) tend to vanish at higher frequencies ($\sim$2600 MHz) [179].

6.3.3.2. Alternating current annealing. Alternating current (ac) annealing is considered as the conventional annealing process with the presence of an ac flowing along the sample axis during the annealing process. It was found that the GMI ratio of an ac annealed Co-based ribbon was much larger than that of a sample annealed without the presence of an ac [181]. The increase in GMI effect of ac annealed ribbon samples can be attributed to the increased transverse permeability and the increased transverse magnetic anisotropy due to the ac induced magnetic field, which is similar to the Joule-heating method [179,180]. In general, both the Joule heating and ac current annealing techniques allow the improvement of the GMI effect in amorphous ferromagnetic materials. These methods are efficient in homogenising the GMI response irrespective of the sample shape.

6.3.4. Conventional stress annealing

The conventional annealing method with the presence of an applied stress during the annealing process is known as the conventional stress annealing method [182,183]. The influence of applied stress during annealing on the magnetic properties and GMI effect of several amorphous ferromagnetic materials, including ribbons [182–185] and wires [148,186], has been investigated. It was shown that, in the case of Co-based amorphous ribbons, the transverse magnetic anisotropy was induced by stress annealing [182–184]. Samples with similar anisotropy strengths were found to show very different GMI responses [182]. When a Co-based amorphous ribbon was annealed under an applied tensile stress of 500 MPa, the field sensitivity of GMI measured at a frequency of 3 MHz was found to reach up to 83%/Oe [184]. In contrast, for stress-annealed Fe-based amorphous ribbons [185], the GMI effect was found to decrease gradually with increasing annealing stress. This is because the application of a tensile stress introduces a different transverse anisotropy that, in turn, significantly reduces the transverse magnetic permeability [180]. The different dependences of GMI on applied stress between the stress-annealed Co-based and Fe-based amorphous ribbons can be attributed to the difference in their domain structures that are determined by the samples' signal of magnetostriction [182,183].

6.3.5. Simultaneous stress and magnetic field annealing

The simultaneous presence of an applied tensile stress and a longitudinal dc magnetic field during the annealing process was found to have a strong influence on magnetic anisotropy and hence field-dependent GMI features of Co-based amorphous ribbon samples [187]. Asymmetry in the GMI profile was also observed in this case, and it was believed to originate from a ferromagnetic exchange coupling of the soft magnetic amorphous phase with a magnetically harder crystalline surface layer. Such asymmetry may be of interest in developing auto-biased linear GMI field sensors [10].

6.3.6. Simultaneous stress and current annealing

This is a modified Joule-heating technique with the addition of an applied stress during the heat treatment [125,129,180,186,188,189]. For stress-Joule-heated Fe-based amorphous wires, the GMI ratio increased with increasing annealing stress up to 275 MPa [186]. The GMI behavior of the wire was interpreted by considering a simple effective field model, where the anisotropy of the material is altered by annealing and applied stress [11]. Mandal et al. [125] found that the stress-Joule heating of positive-magnetostrictive glass-coated amorphous microwires caused a considerable reduction in the GMI ratio compared to the Joule-heating method [129]. With respect to these findings, it is worth mentioning that field-dependent GMI features at magnetic fields lower than the anisotropy field varied strongly upon the application of stress during the annealing process. Remarkably, a reduction in hysteresis in the GMI profile with respect to increasing and decreasing fields was observed in such stress-Joule-heated samples, which is useful for non-hysteretic GMI-based sensor applications.

Interestingly, a giant stress-impedance (SI) effect was observed in stress-Joule-heated Fe-based amorphous ribbons. With increasing annealing current density up to 42 A/mm^2, a maximum SI ratio of 350% was achieved in samples annealed by Joule heating at a current density of 33 A/mm^2 in the presence of a longitudinal applied tensile stress of 100 MPa [180]. This is consistent with what was reported for Joule-heated nearly zero magnetostrictive amorphous wires [188] and microwires [189,190]. In these examples, the torsion stress dependence of the GMI effect may be useful for stress sensing applications [190].

6.3.7. Laser annealing

The influence of laser annealing energy on the GMI effect in Co-based amorphous ribbons and microwires was first investigated by Ahn et al. [191,192]. These samples were annealed by pulsed Nd:YAG laser at various annealing energies between 65 and 230 mJ/pulse in air. For laser-annealed Co-based amorphous ribbons, with increasing laser-annealing energy, the GMI ratio first increased until reaching a maximum ($\Delta Z/Z = 30\%$) at 136 mJ and then decreased at higher energies [191]. It was also found that when the laser annealing energy increased up to 100 mJ, the anisotropy field in as-quenched samples decreased from 1.9 to ~0.5 Oe because of the increase of magnetic softness caused by the laser annealing effect. The decrease of the GMI effect and the increase of the anisotropy field were probably due to the microstructural change caused by laser annealing [172]. For a Co-based amorphous microwire after glass removal by chemical etching, the GMI effect was found to be enhanced by illuminating Nd:YAG laser at high frequency. This is a consequence of internal stress relief, resulting from laser energy absorption [192]. The increase in the high-frequency GMI effect reflects the fact that the contribution to the circumferential magnetisation from magnetic moment rotation in core domains increased due to magnetic softening.

The application of a small field (~3 Oe) along the microwire during laser annealing led to a considerable increase in the GMI effect in both low- and high-frequency ranges [192]. Recently, Roozmeh et al. [193] studied the effect of laser annealing on the GMI of Co-based amorphous ribbons with and without the presence of a transverse magnetic field. It was shown that laser annealing without an applied magnetic field had little influence on the GMI effect, while laser annealing with the presence of a transverse magnetic field strongly improved the GMI effect of as-quenched amorphous ribbons. It was also found that upon laser annealing, the GMI effect first increased with increasing annealing time, reached a maximum for the sample laser-annealed for 1 min, and then decreased for longer annealing times. The combination of magnetic field and laser annealing caused a local structural change and hence induced an excess anisotropy, as seen from the GMI curves [193].

In general, laser annealing is regarded as a superior method for improving soft magnetic properties and the GMI effect of amorphous ferromagnetic materials compared to furnace annealing (conventional annealing) because it is non-contact, quick to perform (a few microseconds), and can be performed in open air.

6.4. Effect of applied stress on GMI

The influence of applied stress on the GMI effect has been investigated in several amorphous ferromagnetic materials including amorphous microwires/wires [125,188–190,194] and ribbons [112,195,196]. For a positive-magnetostrictive glass-coated amorphous microwire (e.g., $Co_{83.2}Mn_{7.6}Si_{5.8}B_{3.3}$), the application of a tensile stress led to a considerable reduction in the magnitude of the GMI effect at frequencies below 8 MHz, but at higher frequencies, the magnitude of the GMI effect is equal to that without an applied tensile stress [125]. It should be noted that the magnetic field at which the GMI peak occurred decreased in the stressed samples. In contrast, an improvement of the GMI effect (~130%) measured at a frequency of 10 MHz was achieved in a nearly zero and negative-magnetostrictive amorphous microwire (e.g., $Co_{68.5}Mn_{6.5}Si_{10}B_{15}$) under an applied tensile stress of 66 MPa [189]. Based on the stress dependence of the GMI effect in these amorphous microwires, a magnetoelastic sensor has been developed [190]. Torsion-stress dependent GMI features were also observed in Co-based amorphous and Fe-based nanocrystalline wires with vanishing or transverse anisotropy [189,192]. Such variation in the shape of the GMI curve as well as its magnitude can be explained by considering the competition between the magnetoelastic anisotropy induced by the processing and the helical anisotropy induced by the torsion [192].

6.5. Effect of neutron irradiation on GMI

The effect of neutron irradiation on permeability spectra and GMI of Fe-based amorphous and nanocrystalline materials was first investigated by Phan et al. [197,198]. The results indicated that neutron irradiation increased the permeability of the amorphous alloy but decreased the permeability of the nanocrystalline alloy in a high-frequency region ($f \geqslant 1$ MHz), while the opposite was found in a low-frequency region ($f < 1$ MHz). The magnetic relaxations in the low- and high-frequency regions were attributed to the irreversible domain wall motion and reversible rotational magnetisation, respectively. It was the increase in permeability of the neutron-irradiated amorphous alloy, resulting from reversible magnetisation rotation, that caused an improvement in the GMI effect (see Fig. 33). In contrast, the decrease in permeability of the neutron-irradiated

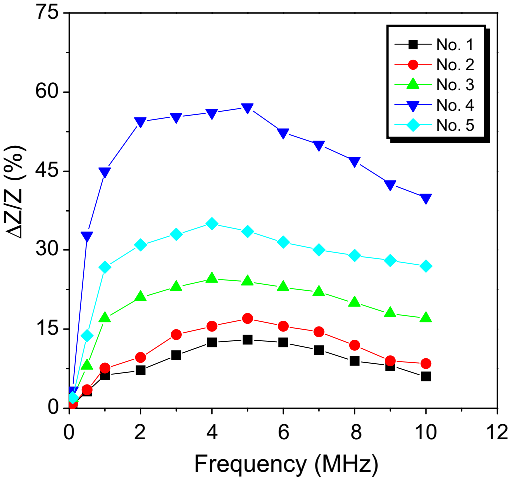

Fig. 33. The measured maximum GMI effect ($[\Delta Z/Z]_{max}$) as a function of frequency for $Fe_{73.5}Si_{13.5}Cu_1Nb_3Si_9$ ribbons. (No. 1) as-quenched alloy, (No. 2) alloy annealed at 473 K, (No. 3) neutron-irradiated amorphous alloy, (No. 4) alloy annealed at 823 K only, and (No. 5) the 823 K-annealed and neutron-irradiated alloy.

nanocrystalline alloy caused by reversible magnetisation rotation produced a reduction in the GMI effect relative to the nanocrystalline alloys (see Fig. 33). These results have important implications in the application of these materials as sensing elements in a nuclear environment, when the magnetoimpedance effect is used. This is because, compared with annealed amorphous alloy, amorphous materials are less brittle and easier to handle, which provides the necessary manufacturing flexibility and, more importantly, their magnetoimpedance properties can be enhanced by subsequent neutron irradiation. This offers an opportunity to explore the high magnetic sensing application of neutron-irradiated amorphous ferromagnetic materials.

Recently, Cayssol et al. [199] also investigated the influence of low-energy He ion irradiation on the dynamics of a single Bloch domain wall in magnetic wires based on Pt/Co/Pt trilayers with perpendicular anisotropy. The results showed that uniform ion irradiation caused a significant reduction in the pinning center's density and the pinning force, resulting in improved domain wall motion. This reveals that the GMI effect can be further enhanced in amorphous magnetic wires when submitted to appropriate ion irradiation, because the enhancement of GMI is related to improved domain wall motion [10]. This is of practical importance for future magnetic devices.

6.6. *Effect of hydrogen charging on GMI*

The influence of hydrogen charging on the magnetic softness and the GMI effect has been studied in amorphous Fe–Si–B and Co–Fe–Si–B wires [200]. The hydrogen charging was carried out at 25 °C and in a stirred solution by applying a constant current density of 20 mA/cm^2 for 1 h. It was found that hydrogen charging caused a drastic reduction in the GMI effect from 24.4% to 7.1% in the Fe–Si–B amorphous wire, while no significant variation in the GMI effect was observed in the Co–Fe–Si–B amorphous wire after hydrogenation. This indicates that such Co–Fe–Si–B amorphous wires with vanishing magnetostriction are more promising for sensor applications. In fact, the change of the GMI effect has been correlated to that of the magnetic softness (i.e., the magnetisation and coercivity) [200]. In this case, it was believed that hydrogen charging modified the domain structure and hence the magnetic properties of the samples. After 2700 min degassing, the GMI effect was found to be larger in the hydrogen-charged Fe–Si–B amorphous wire than in the as-received Fe–Si–B amorphous wire. It is believed that this is due to stress relief on the surface layer of the wire.

6.7. *Effect of pH value on GMI*

Influences of pH value on the GMI of electrodeposited CoNiFe/Cu wires have been systematically studied by Atalay et al. [201]. The results showed that the composition, surface quality and magnetic and magnetoimpedance properties were strongly affected by the pH value of the electrochemical bath. Under the same processing, with increasing pH, the wire diameter gradually increased, while the coercivity first decreased and then increased [201]. In particular, the GMI effect first increased with increasing pH, reached a maximum at pH 2.4, and then decreased for higher pH. This suggests that the selection of a solution with appropriate pH is important for optimising the GMI effect of electrodeposited wires.

6.8. Effect of magnetostriction on GMI

The influence of magnetostriction on the GMI effect has been studied in several amorphous wires [176,202] and ribbons [97,203,204]. Barandiaran and Hernando [203] have simulated the influence of magnetostriction on the GMI effect, revealing that magnetostriction is a key parameter in determining the magnitude of GMI. In order to assess the influence of magnetostriction on GMI, Table 2 shows the relationship between the GMI effect and magnetostriction in both amorphous and annealed $(Co_{1-x}Fe_x)_{70}Si_{12}B_{18}$ ribbons [112]. It can be seen that the largest GMI effect is obtained in samples with vanishing magnetostriction. The magnitude and sign of the magnetostriction constant of a sample can be changed either by modifying the alloy's composition, or by annealing (see Table 2). However, it should be noted from Table 2 that the ribbons with similar values of λ_s do not have the same level of GMI effect. This means that the magnetostriction constant is not the only factor affecting the GMI magnitude. It was also found that for the same ribbon, the change in GMI effect due to annealing tended to follow the change in magnetostriction constant. This shows that annealing under an applied magnetic field, and/or tensile stress, and/or torsion, may induce specific anisotropies, which can either be beneficial or detrimental to the GMI effect, depending on the annealing temperature and time [203]. Annealing at low temperatures and/or in a short time should be recommended for Co-based samples, because this will relieve the quenched-in stresses and result in an increase of magnetic permeability, hence increasing the GMI effect. As for Fe-based samples, annealing at temperatures close to the onset crystallisation temperature of the alloy has proved useful in producing nearly zero magnetostrictive nanocrystalline materials with a much improved GMI effect [87].

6.9. Aftereffect of GMI

The so-called magnetoimpedance aftereffect is known as the change in GMI effect with time and has been observed in amorphous wires and ribbons [97,205–210]. The origin of the magnetoimpedance aftereffect can be related to the permeability aftereffect of the diffusive type, and it has been experimentally shown that the occurrence of magnetoimpedance relaxation is a direct consequence of the diffusion permeability aftereffect. Therefore, the permeability aftereffect is the main mechanism behind the magnetoimpedance afteref-

Table 2
Saturation magnetostriction (λ_s) and GMI ratio $[\Delta Z/Z]_{max}$ (%) measured at $f = 100$ kHz and $i = 5$ mA for $(Co_{1-x}Fe_x)_{70}Si_{12}B_{18}$ ribbons before (as-quenched) and after annealing

Composition (x)	As-quenched λ_s ($\times 10^{-6}$)	As-quenched $[\Delta Z/Z]_{max}$ (%)	Annealed λ_s ($\times 10^{-6}$)	Annealed $[\Delta Z/Z]_{max}$ (%)
0.04	−0.48	3	−0.26	9
0.045	−0.35	4	−0.14	3
0.047	−0.30	13	−0.083	12
0.048	−0.28	2.5	−0.09	8
0.049	−0.20	11	−0.013	13
0.05	−0.16	14	0.065	7
0.053	−0.10	18	0.14	11
0.057	0	21	0.25	7.5

fect [97]. Furthermore, Raposo et al. [209,210] studied the temperature dependence of magnetic aftereffect in Co-based amorphous wires in the range of 80–400 K and found the highest aftereffect of GMI at temperatures around 350 K. Accordingly, they proposed that the existence of long-range diffusion processes governed the dynamics of this system. Nonetheless, this phenomenon is not thoroughly understood and it warrants further investigation.

From an engineering perspective, the magnetoimpedance aftereffect is undesirable for GMI sensor applications and it should be reduced as much as possible. Fortunately, a proper annealing treatment has been shown to be effective not only for improving the GMI effect, but also for considerably reducing the GMI aftereffect [10,112]. A very small GMI aftereffect was obtained in samples with vanishing magnetostriction [112]. This once again indicates that such zero-magnetostrictive samples are the most promising candidates for GMI sensor applications.

6.10. Effect of LC-resonance circuit on GMI

Influences of LC-resonance circuit on GMI in amorphous microwires have been investigated [211–215]. Lee et al. [211] produced a new LC resonator using a glass-coated magnetic microwire, in which the *LC*-resonator was directly constructed on the microwire by forming two capacitive terminal electrodes at the ends of the microwire without direct contact to its ferromagnetic core. The electrodes act as capacitors in the LC-resonance circuit. Because the change of impedance in the LC-resonator results from both the change in permeability of the microwire and the LC resonance of the circuit, the GMI response can be greatly improved by adjusting frequency of the ac flowing through the sample. The GMI effect reached an extremely large value of 450,000% by precisely tuning the frequency at a value of around 551.9075 MHz [211].

With increasing frequency, GMI profiles showed either a single-peak (SP) or double-peak (DP) feature [213–215]. Remarkably, a multiple-peak GMI behavior appeared to occur in the frequency range of 100–1000 MHz as displayed in Fig. 34. This is different from that observed for Co-based microwires [10] in the intermediate frequency range of

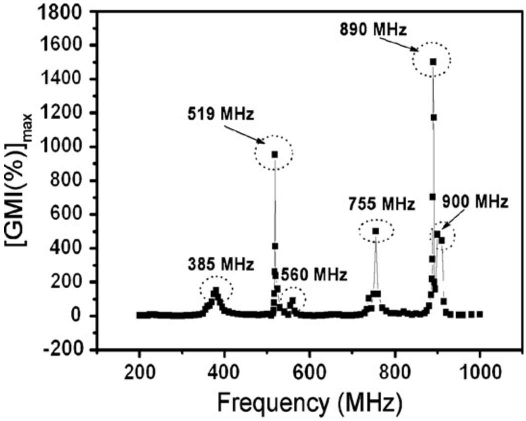

Fig. 34. The frequency dependence of the maximum GMI ratio, $[GMI(\%)]_{max}$, for a glass-covered microwire LC-resonator (courtesy A.T. Le).

1–100 MHz, in which GMI curves often show a SP feature at low frequencies and a DP feature at higher frequencies, with only a maximum of GMI ratio obtained over this frequency range. This also differs from what was observed in GMI curves with respect to ferromagnetic resonance in the frequency range of 1–10 GHz, for a typical Co-based microwire [10]. It is believed that the circumferential permeability can be increased by applying an ac current with a frequency sufficiently high to excite resonance of the wire sample through LC circuit matching [211,212]. The occurrence of resonance has been evidenced by a sudden change in phase angle by as much as 180° at a given external dc magnetic field [214]. Accordingly, the GMI features can be explained in terms of the LC-resonance effect [211] and the formation of standing waves in the sample [212]. However, in a high-frequency range where ferromagnetic resonance occurs, an additional contribution to the GMI effect from this resonance must also be included [214].

To further assess the origin of GMI, Le et al. [215] have recently studied the influences of annealing and sample geometry on the GMI effect in a glass-coated microwire LC-resonator. The results indicated that annealing magnetic microwires significantly changed the permeability and hence the GMI ratio, whereas the magnetoimpedance response was sensitive to varying sample geometry. Accordingly, the authors attributed the observed GMI features to the soft magnetic characteristics, the LC-resonance circuit and the formation of standing magnetic waves within the sample [215]. Nonetheless, the underlying mechanism of GMI in a glass-coated microwire LC-resonator still remains a subject of debate and thus warrants further study.

In general, the features of an LC-resonance circuit can be exploited to increase the sensitivity of GMI-based magnetic sensors while selecting the working frequency. A new class of micromachined magnetic resonator for high-frequency magnetic sensor applications has been proposed [216–218]. In particular, Kim et al. [218] have recently demonstrated the superior features of LC filter-type magnetoimpedance sensors. The LC filter circuit showed the output-changing ratio per 1 Oe of 5% at a high frequency of 50 MHz. This value was 2.5 times larger than that expected in a conventional bridge circuit with constant current excitation. This indicates that LC filter-type MI sensors can be used for a wide range of technological applications.

7. Hysteresis and asymmetry in GMI

7.1. Hysteresis in GMI

A typical example involving the hysteretic feature in GMI profiles with respect to increasing and decreasing applied dc magnetic field is displayed in Fig. 35. A two-peak behavior with a dip near zero field was observed at frequencies $f \geqslant 1$ MHz. With increasing frequency, the dip η(%) and hysteresis in the GMI profiles first increased up to $f = 5$ MHz and then slightly decreased at higher frequencies (see the inset of Fig. 35). The increase in the dip reflects an increase of anisotropy in the longitudinal direction of the ribbon with increasing frequency [92,122]. In addition, hysteresis was observed at dc magnetic fields below the anisotropy field and is likely to be related to the magnetisation process due to domain wall displacement [219–223].

Such hysteretic phenomena in GMI profiles can be interpreted by considering the corresponding magnetisation processes that take place in the sample [92,222]. Moreover, there are two kinds of magnetic fields (or two magnetic anisotropies) acting on the sample

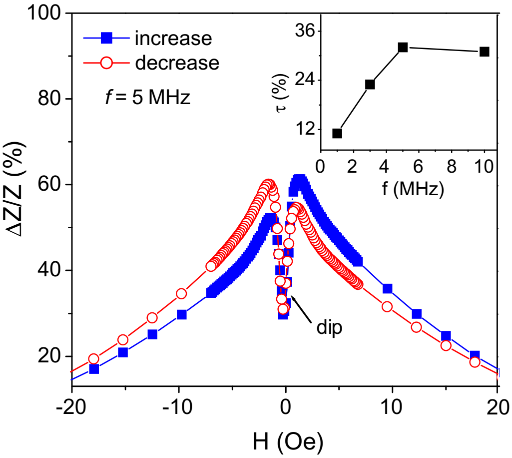

Fig. 35. Magnetic field dependence of the GMI effect [$\Delta Z/Z$] measured at $f = 5$ MHz with respect to increasing and decreasing fields, for a Fe-based nanocrystalline ribbon. The inset shows the change in the dip [τ(%)] with frequency.

when submitted to GMI measurements: one corresponds to the ac magnetic field created by the ac current along the sample, and the other is the dc axial magnetic field that superimposes itself over the first one. When saturation is reached, the dc magnetic field determines the magnetisation, and the ac magnetic field plays a minor role in the rotation of the magnetisation vector inside the sample [222]. When the dc magnetic field is decreased, the magnetisation starts to sense the presence of the ac magnetic field, and the magnetisation vector starts to rotate, thus increasing the transverse permeability and hence the impedance. When the anisotropy field is reached, the magnetisation becomes free to rotate under the influence of the ac magnetic field. The transverse permeability reaches the maximum and the GMI effect reaches the peak. When the dc magnetic field is further decreased, a domain wall irreversible process starts to take place, resulting in irreversible contributions to the transverse magnetisation processes. Consequently, a hysteretic GMI behavior was observed [220]. In short, the origin of the hysteretic GMI is related to the hysteresis of the magnetisation process and to the spatial distribution of magnetic anisotropy, which determines the domain structure in metallic glasses and their magnetic permeability. This hysteresis is often small in homogeneous magnetic materials and can be removed by annealing the as-cast amorphous samples under the application of an external stress and/or a magnetic field [188–190].

7.2. Asymmetry in GMI

In ferromagnetic materials, a small asymmetry in the GMI curve (Fig. 35) with respect to increasing and decreasing fields appeared to occur naturally at small dc-bias magnetic fields below the anisotropy field. It can be modified either by the application of a dc bias current [224–231] or an ac-bias-field [131,232,233] along the sample axis during GMI measurement or due to exchange bias [234–240]. This section will discuss the principal features and the origin of asymmetric GMI.

7.2.1. Asymmetrical GMI due to dc bias current

When a dc bias current (I_{dc}) is applied parallel to the ac current (I_{ac}) and the dc external magnetic field (H_a), it will induce a circumferential dc magnetic field (H_{dc}) that, together with the circumferential ac magnetic field generated by the ac current (H_{ac}), proceed the circumferential magnetisation processes against the dc external magnetic field (H_a). It is the combination of helical magnetic anisotropy and the circumferential dc field produced by the bias current that causes an asymmetry in GMI profiles in Co-based amorphous wires with a dc bias current superimposed on the driving ac current [224–231]. In this case, a symmetric SP or DP-like GMI curve should appear in the absence of the dc bias current [224]. But a very small asymmetry in the GMI curve was still observed in the case of $I_{dc} = 0$, reflecting the presence of the internal helical anisotropy in the wire [231]. When the dc bias current (I_{dc}) was applied, asymmetry in GMI appeared, depending upon both the direction and magnitude of I_{dc} [224–231].

The magnetic field dependence of an asymmetric GMI (AGMI) profile measured at different dc-bias currents is shown in Fig. 36. A small AGMI appears for $I_b = 1$ mA, and as I_b increases until around $I_b = 15$ mA, the asymmetry becomes larger, but subsequently decreases for $I_b = 25$ mA. This change is likely to be due to the influence of the unidirectional bias field on the domain wall motion in the circumferential direction. The biasing circumferential field produced by the dc-biased current makes the ac susceptibility, arising from wall displacement, asymmetric upon application of the external magnetic field along the wire axis [226,227,231]. The conjunction of the external static magnetic field and the dc-biased current applied along the wire introduced an effective helical field acting on the wire [231]. Hence, GMI becomes asymmetric with regard to the sign of the applied static field, and this asymmetry becomes larger with increasing biasing circumferential field. When the biasing circumferential field is large enough, the domain wall motion is suppressed. This, together with asymmetry, results in the decrease of permeability and thus the reduced GMI effect [231]. It is found that the permeability from the wall motion of core domains is nearly constant, irrespective of the bias current, while the permeability from the rotation of shell domains (μ_{rot}) increases with bias current up to 15 mA and then decreases. The increase of μ_{rot} up to $I_b = 15$ mA is due to the enhancement of the shell domain volume by the circumferential field, but the decrease of μ_{rot} for higher current is mainly caused by the hindrance of rotational magnetisation by strong bias field. This explains why AGMI is reduced in magnitude to under $I_b = 25$ mA. It is also found that with increasing dc-bias current, the position of AGMI peak shifts slightly to lower dc fields. When the direction of dc-bias current is reversed, the asymmetry also reverses. With increasing frequency, the asymmetry in GMI first increases and then decreases yielding a maximum at a certain frequency [231]. When frequency exceeds a critical frequency, the asymmetry of the GMI profile becomes small. This is because the influence of dc bias field on rotational magnetisation is smaller than that on wall motion. These finding are useful for constructing an auto-biased linear field sensor [224,230].

In an attempt to theoretically explain the proposed mechanism for AGMI in amorphous wires due to dc bias current, based on the electromagnetic model, Panina et al. [222,230] showed that the component of surface impedance (i.e., ζzz) becomes asymmetric when a circumferential dc magnetic field is added. The asymmetry is related to the axial hysteresis loop that is also asymmetric. However, this model cannot explain why AGMI appeared in Co-based amorphous wires without torsion [190]. This has been experimentally verified by Phan et al. [231] showing that helical internal stress exists in non-twisted

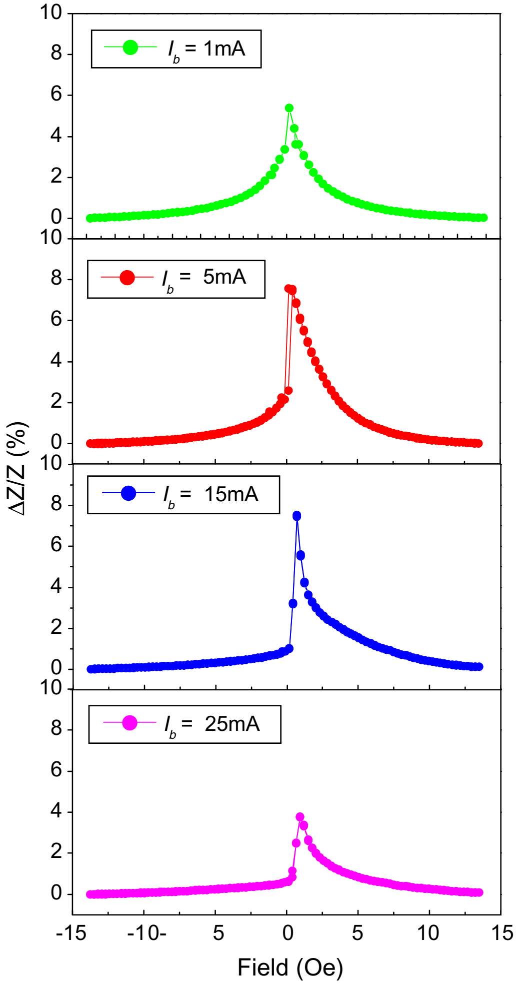

Fig. 36. AGMI profile measured $f = 1$ MHz for different dc bias currents.

Co-based amorphous wires. It has been further estimated that the helical internal stress is smaller in Co-based amorphous wire than that in Fe-based amorphous wire [231], due to the difference in their domain structures [6,7,10]. It is the helical internal anisotropy that plays a significant role in responding differently to the axial magnetisation process and thus to AGMI [227,231]. Therefore, the proposed model [222,230] needs to be further developed.

7.2.2. Asymmetrical GMI due to ac bias field

When a Co-based amorphous wire is subjected to a pulse helical magnetic field produced by the conjunction of an ac pulse current passing through the wire and a coil wound around it, asymmetry in the GMI profile can be produced [131,232,233]. The circumferential and axial components of the helical field were provided by the wire and the magnetising coil, respectively [232]. The effect of an ac bias field (H_b) created by the ac bias current on the wire voltage characteristic, is related to the ac cross-magnetisation process of inducing circulatory magnetisation, so the asymmetry in GMI can result from the combination of helical magnetisation and the axial ac field [232,233]. This process is believed to be similar to that of the Matteucci effect, in which a voltage appears in the presence of an axial field driving helical domain walls [131]. The similarity is considered only at high frequency when the induced circulatory magnetisation has a rotational mechanism. Because the contribution to the voltage due to H_b becomes similar to that induced by the current (i) itself, it can change the voltage versus H_{ex} behavior when frequency increases. In fact, the Matteucci component of impedance can also be controlled by the number of turns of the driving coil. When the number is large, the Matteucci effect contributed positively to the impedance and asymmetry was observed [131,232,233].

7.2.3. Asymmetrical GMI due to exchange bias

This type of AGMI, which is the so-called GMI-valve, was first reported by Kim et al. [234] when investigating the influence of longitudinal weak-field annealing on the GMI profile in Co-based amorphous ribbons. Later, extensive experimental and theoretical investigations have been conducted to understand the origin of this asymmetric GMI [235–240]. It was found that when a Co-based amorphous ribbon was annealed at a suitable temperature ($T_a = 350–380\ °C$) in air with a weak magnetic field ($H_a = 0.05–3$ Oe) along the ribbon, a large asymmetry in the GMI profile appeared [234,235,240]. At relatively low frequencies ($\sim$0.1 MHz), the GMI profiles showed a typical DP characteristic for $H_a \leqslant 100$ mOe whereas only a single-peak appeared under higher H_a with the peak in the anti-parallel field region disappearing completely. The GMI for the field-annealed samples also showed a distinct variation in AGMI features with increasing frequency. The peak in the anti-parallel field appeared again at frequencies above 1 MHz, and it developed strongly with increasing frequencies. The AGMI phenomenon has been attributed to the crystallisation of the surface underlayer, which becomes depleted in B and Si due to the surface oxidation [235]. In addition, this type of heat treatment produces asymmetric hysteresis loops in amorphous ribbons due to the interaction between the inner amorphous phase and the magnetically harder crystalline phase on the sample outer layer [241]. When the crystallisation took place under a weak magnetic field, the crystallites were magnetically ordered, resulting in an effectively unidirectional surface anisotropy. It is the influence of the unidirectional surface anisotropy on domain wall motion in the transverse direction that in turn causes the AGMI [234–237,240].

In an attempt to qualitatively explain the AGMI features, a phenomenological model has recently been proposed by Buznikov et al. [238,239]. Within the framework of this model, the effect of a surface crystalline layer on the GMI response is described in terms of an effective bias field, due to coupling between the crystalline layer and amorphous phase. It is generally accepted that the presence of a bias field significantly changes the GMI response. At low frequencies, domain wall displacement leads to a step-like change in the GMI profile. At high frequencies, domain wall motion is damped and an asymmetric DP-like GMI behavior is attained. This proposed model [238] can qualitatively describe the AGMI features in longitudinally weak-field-annealed Co-based amorphous ribbons [234], but it cannot address the question of why AGMI reduced considerably when the sample was annealed in air at a sufficiently high magnetic field [235–237,240]. Furthermore, the GMI peak for an antiparallel field region started to appear again at a relatively

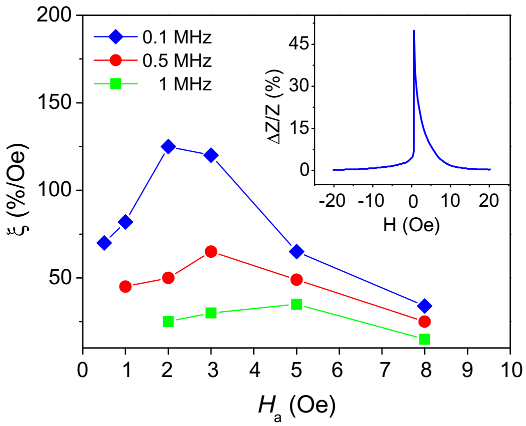

Fig. 37. The field sensitivity of GMI changes as a function of field annealing (H_a) at different frequencies. The inset shows the GMI profile measured at $H_a = 2$ Oe and $f = 0.1$ MHz.

high annealing field (~15 Oe), which was likely to be due to the dominant effect of unidirectional anisotropy over the uniaxial anisotropy on the domain wall motion and the rotation of magnetic moments [235]. This finding has been experimentally verified by Phan et al. [240] by considering the complex permeability spectra in relation to the rotational dc magnetisation. It has been highlighted that annealing in open air at magnetic fields (H_a) smaller than the anisotropy field (H_k) along the ribbon introduced a peculiar domain structure [234–237]. This enhanced the transverse permeability and a larger asymmetry in GMI was consequently observed [234–237,240]. Annealing at magnetic fields slightly higher than the anisotropy field ($H_a > H_k$) induces a unidirectional magnetic anisotropy along the ribbon and this anisotropy can be large enough to hinder domain wall motion in the transverse direction, thereby significantly reducing the GMI effect [235,240]. Interestingly, the optimum GMI-valve behavior, which corresponds to the highest field sensitivity of GMI of 125%/Oe, was observed at $f = 0.1$ MHz in the ribbon annealed under a field of $H_a = 2$ Oe (see Fig. 37) [240]. This is ideal for developing auto-biased linear field sensors. However, further theoretical developments are necessary to provide a quantitative explanation for the observed phenomenon.

8. Selection of GMI materials for sensor applications

8.1. Criteria for selecting GMI materials

For a GMI material to be employed for GMI sensor applications, two main requirements should be met, namely, a high GMI ratio (or a large GMI effect) and a high sensitivity to the applied field (or a high magnetic response). In view of the theoretical analyses and experimental results, it is concluded that a large GMI effect should exist in magnetic materials having:

- low resistivity, ρ,
- high magnetic permeability, μ,

- high saturation magnetisation, M_s, and
- small ferromagnetic relaxation parameter (or low damping parameter), α.

In this context, crystalline ferromagnetic materials have the advantage of lower resistivity (ρ), but amorphous ones have better soft magnetic behavior (e.g., higher magnetic permeability, μ, and saturation magnetisation, M_s) because they lack magnetocrystalline anisotropy. In particular, non-magnetostrictive materials can be expected to show the best GMI performance because the magnetoelastic contribution to magnetic anisotropy substantially deteriorates the soft magnetic behavior. Improvement in the magnetic softness of an actual amorphous material by appropriate thermal treatment and/or the application of external parameters (mechanical stress, magnetic field, etc.) can lead to a simultaneous improvement in the GMI effect and its field sensitivity. The damping parameter (α) is often considered in the high-frequency range where ferromagnetic resonance takes place, while it can be neglected in the intermediate frequency range (i.e., $f = 0.1$–10 MHz), where most GMI-based sensing applications have been identified (see Section 9). In addition, for practical sensor applications, the manufacturability and cost of materials are also important factors.

8.2. Evaluation of GMI materials

In ferromagnetic materials, the highest value of the GMI effect, experimentally observed is much smaller than the theoretically predicted value. Research in the field has been focused on special thermal treatments and on the development of new materials with properties appropriate for practical GMI sensor applications. In this section, all existing GMI materials will be reviewed and evaluated.

8.2.1. Rapidly quenched wires

8.2.1.1. Co-based wires. Both conventional and glass-covered Co-based amorphous wires exhibit a GMI effect, owing to their high circular permeability. This is mainly due to the presence of circumferential anisotropy and outer shell circular domain structure that results from coupling between negative magnetostriction and quenching compressive stress [7–10,242]. Among the Co-based amorphous alloys investigated, an alloy system with the nominal composition of Co–Fe–Si–B exhibits nearly zero and negative magnetostriction of $\lambda_s = -0.4 \times 10^{-7}$. This alloy is often obtained by alloying Fe–Si–B that has a positive λ_s of 25×10^{-6} with Co–Si–B that has a negative λ_s of -3×10^{-6} [79,242]. As a result, a record value of GMI ratio (1200% at 14.2 MHz) has been achieved in the conventional amorphous $Co_{68}Fe_{4.35}Si_{12.5}B_{15}$ wire [204]. This value is much larger than that reported earlier (600%) with the same composition [8,242]. This larger value of GMI ratio is a result of minimising contact resistance and cancelling parasitic impedance [204]. However, a high field sensitivity of GMI (~500%/Oe) was reported by Vazquez [8], while no information was found in the work by Garcia et al. [204].

In an attempt to develop magnetic wires for high-frequency sensor applications, Nie et al. [147] reported that a Co–Mn–Si–B amorphous glass-covered wire with nearly zero magnetostriction exhibited a GMI effect at high frequencies. For the amorphous $Co_{68.2}Mn_7Si_{10}B_{15}$ microwire, the GMI ratio and magnetic response reached the values of 153% and 65%/Oe, respectively, at a frequency of 30 MHz. Vinai et al. [243] recently revealed that these microwires also exhibited a GMI effect at frequencies up to GHz. In the frequency range of 100 MHz–6 GHz, the GMI ratio reached a maximum value of ~100% at a frequency of 2 GHz. As shown earlier in Section 6, for Co-based amorphous wires, the GMI effect can be further improved by appropriate field annealing [16], Joule current annealing [176–180] or the application of a tensile stress [183,184].

In summary, the Co-based amorphous wires with nearly zero and negative magnetostriction are good candidates for GMI sensor applications. It should be noted that while the Co-based conventional and glass-covered amorphous wires are suitable for sensor applications in the low and intermediate frequency range (up to several MHz), the glass-covered amorphous microwires can be used for electro-technical devices operating at much higher frequencies (up to several GHz). Due to their relatively high resistivity, the microwires retain their large GMI value at higher frequencies, when compared to ribbons and wires. In practice, depending upon the specific requirements of a sensor device (e.g., the operating-frequency range), either wires or microwires should be chosen accordingly.

8.2.1.2. Fe-based wires. Fe-based amorphous wires have relatively small or even no MI effects, owing to their relatively small effective permeability, which is due to the presence of an outer shell radial domain configuration that results from the coupling between the highly positive magnetostriction and the quenching compressive stress [6,10,16,130]. A primary alloy of Fe–Si–B having a positive λ_s of 25×10^{-6} was found to show poor magnetic softness and hence a small MI effect (~3%), while a larger MI effect (~36%) was obtained in the annealed wires [16,130,244]. It was the precipitation of an FeSi nanocrystalline phase that significantly decreased the bulk positive magnetostriction and hence gave rise to the MI effect of the annealed Fe–Si–B wires [244]. The crystallisation of Fe–Si–B-based amorphous alloys containing Nb and Cu causes the formation of a nanoscale bcc structure and the bcc alloys exhibit excellent ultrasoft magnetic properties (i.e., high effective permeability and small coercivity) [16,79]. In these alloys, the roles that Cu and Nb play are to maximise the density of crystal nuclei and to retard grain growth, respectively, leading to an ultrafine grain structure. Among these alloys, the nanocrystalline alloys with a nominal composition of $Fe_{73.5}Si_{13.5}B_9Nb_3Cu_1$ were found to show the best magnetic softness. These materials are therefore expected to show large MI effects. Indeed, Knobel et al. [16] reported that conventional $Fe_{73.5}Si_{13.5}B_9Nb_3Cu_1$ nanocrystalline wires (e.g., the amorphous wire samples annealed at 550–600 °C) exhibited a GMI effect. The largest value of GMI ratio was about 200% at a frequency of 500 kHz for the wire sample annealed at 600 °C for 1 h. In another study, Li et al. [245] partially substituted Fe by Cr in $Fe_{73.5}Si_{13.5}B_9Nb_3Cu_1$ nanocrystalline wires with the expectation of further reducing the magnetostriction of the primary alloy. They found that although the GMI ratio and magnetic response were slightly smaller in Cr-doped samples, the addition of Cr improved the GMI response and significantly reduced the undesirable hysteretic effect in GMI curves with increasing and decreasing applied magnetic fields [245]. In addition, the presence of Cr significantly improved the corrosion resistance properties, which is desirable for sensing applications in a corrosive environment. The GMI effect was also observed in Fe-based nanocrystalline glass-coated wires and microwires [6,10]. Interestingly, the $Fe_{89}B_1Si_3C_3Mn_4$ nanocrystalline glass-covered microwires were found to show the GMI effect in the GHz-frequency range [243]. At a frequency of 4 GHz, the GMI ratio reached a value as high as 70% for the sample annealed at 350 °C. For this typical microwire, conventional furnace annealing proved more effective in improving the GMI effect compared with current annealing. Furthermore, it should be recalled that for both Fe-based amorphous and nanocrystalline glass-covered wires, the removal of the glass layer can significantly improve the GMI effect and magnetic response. However, the GMI ratios of Fe-based nanocrystalline wires are often smaller than those of Co-based amorphous wires [242].

8.2.2. Electrodeposited wires

Besides rapidly quenched wires, electrodeposited wires, which comprise of a highly conductive non-magnetic metal core (e.g., Cu, CuBe, and Ag) and a thin layer of soft magnetic metal (e.g., NiFe, NiFeRu, NiFeMo, CoP, and CoNiFe), have been found to show excellent GMI behaviors [62–77,246–250]. For electrodeposited wires, the magnetic layer has either a circular or radial domain configuration depending strongly upon the alloy composition and the sample processing conditions [248]. Wires having a circular domain structure are often expected to show a larger MI effect [246,250].

In a pioneering work, Usov et al. [246] predicted that the GMI effect could be further improved in a composite amorphous wire when the electrical conductivity of the inner core is much higher than that of the shell region. Since this work, experimental efforts were devoted to investigating the GMI effect in electrodeposited wires, such as CoP/Cu [62–66,247], NiFe/Cu [68–70,249], CoNiFe/Cu [71,72,248], NiFeRu/Cu [73], and NiFeMo/Cu [74]. Sinnecker et al. [62] reported that an electrodeposited CoP/Cu wire exhibited radial magnetic anisotropy (i.e., the radial domain structure) and the size of the closure domains increased with the magnetic layer thickness (CoP). It is interesting to note that, although magnetic wires with a radial magnetic anisotropy are not expected to show any GMI effect, the significant increase in GMI ratio with the magnetic layer thickness of the CoP/Cu composite wire was attained [62]. This indicated that the observed GMI effect was associated with the current distribution along the sample radius with two well-defined regions having different transport and magnetic properties [63–66]. Recently, Phan et al. [247] optimised the processing conditions in order to achieve the largest GMI effect in a typical CoP/Cu electrodeposited wire. The largest GMI ratio was achieved with a deposition time of 6 min and an electrolytic current density of 639 mA/cm^2. At the measured frequency of 10.7 MHz, the GMI ratio and magnetic response reached the highest values of 534% and 21%/Oe, respectively. It was proposed that the changes of deposition time and electrolytic current density, caused variations in the domain structure of the CoP magnetic layer and hence the GMI behavior [247]. More interestingly, Kurlyandskaya et al. [248] found that the GMI ratio reached a value as high as 1200% at a frequency of 4 MHz for the FeNiCo/CuBe electroplated wire. This is the highest value reported until now, amongst existing electrodeposited wires. However, no information on the magnetic response of GMI was given [248]. In a comprehensive study into investigating the influences of processing parameters (e.g., electrodeposition current density, duty cycle, electrolyte solution, pH value, applied magnetic field, magnetic layers, and post annealing) on the GMI of electrodeposited NiFe/Cu wires, Li et al. [249] reported that the GMI ratio and magnetic response reached maximum values of 1110% and 218%/Oe, respectively, at a frequency of 4 MHz for a DC joule annealed wire sample.

Recently, it has been revealed that the GMI effect can be further improved in electrodeposited wires by the inclusion of an insulating interlayer between the core and the magnetic shell (e.g., CuBe/Insulator/NiFeB wires) [76,77]. For instance, the GMI ratio reached a value of 250% at $f = 500$ kHz to 1 MHz for an electrodeposited CuBe/insulator/NiFeB wire, which is much larger than that of ~23% at $f = 1$ MHz for the electrodeposited CuBe/NiFeB wire without the insulator layer [76]. This can arise from the differences in current distribution under the external magnetic field and from the electromagnetic interaction between the conductive core and the ferromagnetic layer of the composite wires with and without an insulator layer [76,77]. In this context, Buznikov et al. [250] have recently developed a model for predicting the GMI effect in these typical wires. The model reveals that the field dependence of magnetic shell permeability significantly effects the eddy current distribution and therefore leads to the observed GMI effect. The inclusion of a thin insulator layer can lead to a further improvement in the GMI effect at sufficiently high frequencies, because it actually increases both the diagonal and off-diagonal impedance [250].

In general, electrodeposited composite wires are good candidate materials for producing high-performance magnetic sensors and sensing devices operating at low and intermediate frequencies (up to several MHz). Within this operating regime, electrodeposited composite wires may be even more promising than rapidly quenched wires and ribbons.

8.2.3. Rapidly quenched ribbons

8.2.3.1. Co-based ribbons. GMI effects have been reported in Co-based amorphous ribbons owing to the high transverse permeability, due to the presence of a transversely oriented domain configuration [5,10]. Like Co-based amorphous wires, ribbons with Co–Fe–Si–B composition and nearly zero but negative magnetostriction were found to show the largest GMI ratio among Co-based ribbons [98]. The GMI ratio reached a value as high as ~160% at a frequency of 1 MHz in the $(Co_{1-x}Fe_x)_{70}Si_{12}B_{18}$ ($x = 0.057$) amorphous ribbon with nearly zero magnetostriction. Several attempts were made to improve the GMI ratio and magnetic response of the Co–Fe–Si–B alloy by introducing other elements such as Cr, Mn, Ni, and Mo. However, the results obtained were unsatisfactory [251–253].

Recently, Phan et al. [142,173,254] showed that the partial substitution of Cu and Nb for B in an initial Co–Fe–Si–B composition (forming the Co-Fe–Si–B–Cu–Nb composition) improved both the GMI ratio and magnetic response. This substitution favored the formation of a transverse domain structure, because the presence of Cu and Nb allows the formation of well-differentiated microstructures [79]. Annealing at low temperatures also led to a significant improvement in the GMI ratio and magnetic response of these alloys [142]. By optimising the annealing conditions, the largest GMI ratio (513%) and magnetic response (144%/Oe) were achieved at a measured frequency of 5 MHz in the $Co_{70}Fe_5Si_{15}Nb_{2.2}Cu_{0.8}B_7$ ribbon annealed at 300 °C for 25 min (see Fig. 38 and its inset) [254]. These are the largest values to date for Co-based amorphous ribbons. These materials are ideal for use in GMI-based sensing devices operating in the low and intermediate frequency range.

Overall, the GMI effect is smaller in the ribbon-shaped sample than in the wire-shaped one, which is due to their different magnetic domain structures [10]. The advantages of Co-based amorphous materials include low magnetostriction and simple control of magnetic anisotropy by annealing with either an applied magnetic field or an applied external stress [6–12]. The disadvantages are their high resistivity and relatively large GMI aftereffect [97]. In addition, the Co-containing materials are relatively expensive.

8.2.3.2. Fe-based ribbons. Fe-based amorphous ribbons often show relatively small or even no MI effects because of their very small effective permeability due to the presence of a longitudinally oriented domain configuration [10,16,255–273]. In contrast, their Fe-based

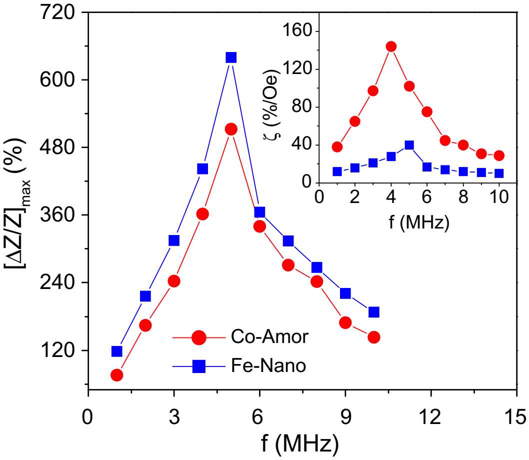

Fig. 38. The frequency dependence of the maximum GMI ratio $[\Delta Z/Z]_{max}$ for (Co-Amor) $Co_{70}Fe_5Si_{15}Nb_{2.2}$-$Cu_{0.8}B_7$ amorphous and (Fe-Nano) $Fe_{71}Al_2Si_{14}B_{8.5}Cu_1Nb_{3.5}$ nanocrystalline samples. The inset shows the frequency dependence of the magnetic response (ξ).

nanocrystalline counterparts have a much improved GMI effect as a result of the increased magnetic softness due to the formation of transversely oriented domains [106,107]. The GMI effect was reported for the first time in Fe–Si–B–Cu–Nb nanocrystalline ribbons by Chen et al. [167]. They showed that the partial substitution of Cu and Nb for B in an initial Fe–Si–B nanocrystalline composition forming the Fe–Si–B–Cu–Nb nanocrystalline composition resulted in a simultaneous improvement in the GMI effect and magnetic response.

Guo et al. [94] reported that, at a frequency of 4.5 MHz, the GMI ratio reached a maximum value of 400% for a $Fe_{73.5}Si_{13.5}B_9Cu_1Nb_3$ ribbon annealed at 550 °C for 3 h, while it was only about 40% for its amorphous counterpart. Several efforts were made to improve the GMI effect as well as the magnetic response of Fe–Si–B–Cu–Nb nanocrystalline alloy either by using different annealing methods [87,168] or by modifying the alloy composition, such as $Fe_{73.5}Si_xB_{22.5-x}Cu_1Nb_3$ ($x = 9,16$) [256], Fe–Cu–Mo–Si–B [175,257,258], $Fe_{73.5-x}Mn_xSi_{13.5}B_9Nb_3Cu_1$ ($x = 1, 3, 5$) [260,261], $Fe_{73.5-x}Cr_xSi_{13.5}B_9Nb_3Au_1$ ($x = 1, 2, 3, 4, 5$) alloys [163,262]. An appropriate heat treatment (e.g., suitable annealing temperature and time, annealing under applied magnetic field and/or tensile stress, etc.) can lead to a large increase in the GMI effect [10]. The addition of a small amount of Al (2 at.%) into the Fe–Si–B–Cu–Nb nanocrystalline alloy, resulted in a significant improvement in both the GMI effect and its magnetic response [92]. This is ascribed to the increased magnetic permeability, decreased coercive force and decreased resistivity [79]. The increased magnetic permeability resulted from a reduction in magnetocrystalline anisotropy and saturation magnetostriction. It is important that the magnetic response value of the Al-containing nanocomposite is significantly larger than that of the Al-free nanocomposite in the whole frequency range investigated [92]. For the nanocrystalline $Fe_{71}Al_2Si_{14}B_{8.5}Cu_1Nb_{3.5}$ sample optimised by annealing, the amorphous ribbon at 550 °C for 45 min, the GMI ratio and magnetic response reached maximum values of 640% and 40%/Oe respectively at the measured frequency of 5 MHz [254]. These values are among the largest for existing Finemet-based nanocrystalline alloys.

GMI effects have also been reported in Nanoperm-based nanocrystalline ribbons, such as Fe–Zr–B [168,171,264,265], Fe–Zr–B–Cu [267,268], Fe–Zr–Cu–B–Al [169,170,266], and Fe–Co–Zr–Nb–B [269,270]. Lee et al. [170] reported that the GMI ratio reached an extremely large value of 1100% at a frequency of 4.6 MHz in a nanocrystalline $Fe_{92-x}Zr_7B_xCu_1$ ($x = 8$) ribbon (i.e., an amorphous alloy annealed at 550 °C for 1 h). This is the largest value reported to date for existing Fe-based nanocrystalline ribbons and wires. However, it is quite difficult to evaluate the GMI response of this sample because a large asymmetrical two-peak feature is observed in the GMI curve, which is due to a small residual hysteresis of the local anisotropy distribution at low magnetic fields. Note that such an asymmetrical two-peak feature of the GMI profile is undesirable for sensor applications [169]. When comparing the magnitude of the GMI effect for Fe-based nanocrystalline ribbons, Knobel et al. [264] revealed that a larger GMI ratio was obtained in a sample with lower electrical resistivity. Because the electrical resistivity of the nanocrystalline Fe–Zr–B–Cu sample was smaller than that of the nanocrystalline Fe–Si–B–Cu–Nb one, a larger GMI ratio was consequently achieved in the former sample [264,265].

Overall, Fe-based nanocrystalline materials have the advantages of nearly zero magnetostriction and simple control of the magnetic softness by appropriate heat treatments where the nanocrystallisation process takes place. When compared with Co-based amorphous alloys, Fe-based nanocrystalline materials have lower resistivity and a higher saturation magnetisation and therefore have a larger GMI effect [254]. However, the field sensitivity of GMI is often lower in an Fe-based nanocrystalline sample. Another disadvantage of the Fe-based nanocrystalline material may arise from its brittleness due to annealing. However, Fe-containing materials are much less expensive than the Co-containing ones.

8.2.4. Magnetic thin films

A large number of single-layer films [274–290], sandwiched films [81,281–287], multilayer films [82–84,159,288–295] and magnetic oxide films [296–301] have been found to show a large MI effect. It has been experimentally shown that the MI effect is much larger in a sandwiched/multilayer film than in a single-layer film [81–83,275]. A large MI ratio was achieved even in as-deposited multilayer films, while no MI effect was observed in as-deposited single-layer films [286,287]. For single-layer films, the longitudinal GMI effect (i.e., when the applied external dc magnetic field is parallel to the ac current) was found to be significantly larger than the transverse GMI effect (i.e., when the applied external dc magnetic field is perpendicular to the ac current). For instance, for an annealed FeSiBCuNb single-layer film, the maximum GMI values obtained were about 18% and 14% respectively, for the longitudinal and transverse cases [275]. Meanwhile, an opposite trend was found for an annealed FeSiBCuNb/Cu/FeSiBCuNb multilayer film, where the maximum GMI ratios were about 67% and 80% for the longitudinal and transverse cases, respectively [275]. In addition, a giant magneto-inductive effect was observed in this film, with a record value of 1733% at a low frequency of 100 kHz.

The difference in MI effect between sandwiched/multilayer films and single-layer films can be understood as follows: for single-layer films, the MI ratio was relatively small at frequencies as low as several MHz because the skin effect was relatively small (i.e., the magnetic depth is much larger than the half film thickness). In contrast, a multilayer film structure (F/M/F) consists of a conductive layer (M = Cu, Ag, Au) sandwiched between two ferromagnetic layers (F = CoSiB, CoFeSiB, FeSiBCuNb). Due to the resistivity difference between the inner and outer layers (i.e., between M and F), a very large change in impedance can occur at much lower frequencies, if the inductance caused by the outer magnetic layers (F) becomes larger than the resistance determined mainly by the inner conductor (M) [82–84,159,288–295]. The difference in electrical resistivity of the inner layer (M) also resulted in a different response of GMI in the CoSiB/M/CoSiB (M = Cu, Ag, Ti) multilayer films [286,287]. The electrical resistivity of Ag (1.62 μΩcm) is smaller than that of Cu (1.72 μΩcm) and Ti (47.8 μΩcm), and the largest GMI ratio was consequently obtained in the CoSiB/Ag/CoSiB sample [287]. The GMI ratio and magnetic response of this sample reached their highest values of 440% and 49%/Oe at a frequency of 10 MHz. Interestingly, an extremely large GMI ratio has been achieved in a sandwich thin-film structure with the inclusion of an insulating interlayer (SiO_2) between the core and the magnetic shell (e.g., CoSiB/SiO_2/Cu/SiO_2/CoSiB) [286]. The obtained GMI ratio and magnetic response were 700% and 300%/Oe, respectively, at a frequency of 20 MHz. These are the highest recorded values for all magnetic thin films. It is believed that the enhancement in GMI of the CoSiB/SiO_2/Cu/SiO_2/CoSiB multilayer film can be attributed to the fact that the driving current flows only through the conductive layer (M = Cu) and the resistivity difference between the F and M layers is enhanced by the existence of the insulator layer (SiO_2) [286]. In the FeSiBCuNb/SiO_2/Cu/SiO_2/FeSiBCuNb multilayer films with a similar structure, however, Li et al. [294] obtained a much smaller value of GMI ratio (i.e., ~32% at 5.45 MHz). This can be attributed to the difference in the domain structure of the magnetic layers (i.e., CoSiB versus FeSiBCuNb) [10]. Regarding the ageing effect of GMI for FeSiBCuNb/SiO_2/Cu/SiO_2/FeSiBCuNb multilayer films, the authors [294] also found that for samples with the covered layer (SiO_2), the GMI ratio remained almost constant with time, while it rapidly decreased for those without the covered layer (SiO_2). This indicates that the insulator layer can improve not only the GMI ratio and magnetic response, but also the lifetime of a magnetic sensor utilising these GMI thin films. Furthermore, it should be noted that for multilayer films with a finite width, the magnetic flux can actually leak across the inner conductive layer, hence resulting in a considerable reduction in GMI ratio [286,287]. In this context, Makhnovskiy and Panina [82] have highlighted that the flux leakage through the conductive layer can result in a considerable drop in GMI ratio when the film width is less than a critical value, which depends on the transverse permeability and the layer thickness. This can quantitatively explain the decrease of GMI ratio in the CoSiB/SiO_2/Cu/SiO_2/CoSiB multilayer films with decreasing Cu layer width [286]. High-frequency MI effects have also been reported in some single-layer and multilayer films [292]. However, the MI values obtained were relatively small. High-frequency MI behavior is quite complex and cannot be fully understood within the framework of existing models [10,11].

Large MI effects have also been reported in a new class of magnetic oxide films, such as Co–M–O (M = Sm, Al, Ti, Si) [296–299], Co–Fe–Al–O [300] and Co–Fe–Hf–O [301] in the high-frequency range. Tuan et al. [300] reported that the MI ratio reached a value of 33% at a measured frequency of 143.66 MHz in a Co–Fe–Al–O film of 1200 nm thickness. However, the research into magnetic oxide films is still at an early stage.

With respect to sensor applications, sandwiched/multilayer films are more promising than single-layer ones. The use of thin film technology is preferable because its compatibility and integrated circuit technology will enable miniaturisation, and avoid alignment and wire soldering issues. However, when compared with rapidly quenched wires and ribbons, thin films are often more difficult to prepare with exact compositions. They are also difficult to connect electrically to a GMI measurement system and difficult to fit into a properly designed transmission line for high-frequency measurements.

8.2.5. Magnetic composites

In order to improve the GMI effect of Co-based amorphous ribbons, Amalou et al. [160–162] successfully designed and produced an amorphous ribbon/Cu/amorphous ribbon trilayer microstructure showing a maximum GMI ratio of 830% at a frequency of 280 kHz, but no information on GMI response was reported. Enhancement of the GMI effect can be attributed to the large effective permeability due to the closed magnetic flux path in the trilayer structure [161,162]. Importantly, these studies have provided an opportunity to develop new magnetic composites that use the amorphous ribbon as precursors.

Recently, Phan et al. [156] produced a new kind of composite material, which consists of amorphous microwires embedded in a polymer–matrix. With the aim of reducing the total resistivity of a composite material, the amorphous microwires were arranged in parallel. The GMI effect was found to increase with increasing number of microwires. It can be seen from Fig. 39 that, at a frequency of 10 MHz, the GMI effect is about 14% for a single amorphous microwire, while it reaches a value of 447% for the composite sample containing four amorphous microwires. Furthermore, the magnetic response of the composite containing four amorphous microwires reaches a value of 43%/Oe, which is much higher than that of a single microwire (~2%/Oe) at the measured frequency of 10 MHz. To clarify the assumption that an enhancement of the GMI effect in a composite material is due to reduced resistivity, the authors [156] also investigated the GMI effect with reducing length of microwires. Because the resistivity of a microwire decreases with reducing length, a larger GMI effect can be expected in a shorter microwire. Indeed, the GMI effect was observed to be larger in the composite samples containing shorter microwires. For example, at the measured frequency of 10 MHz the observed GMI effect was 235% for the composite sample containing two microwires of 1 mm length, while it was 83% for one of 4 mm length. This once again reaffirms that the sample resistivity is an important factor in determining the magnitude of the GMI effect. Furthermore, both the GMI effect and

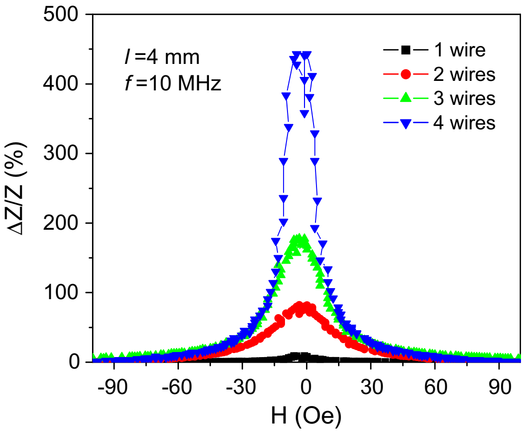

Fig. 39. The GMI effect measured as a function of magnetic field at $f = 10$ MHz in the composite sample containing different amorphous microwires of 4 mm length as compared to the single amorphous microwire.

its magnetic response were significantly enhanced with reducing microwire-length. This is beneficial for practical applications, because the miniaturisation of actual electronic devices requires the sensing element to be as small as possible. This investigation demonstrates the potential for using magnetic wires as sensing elements for smart structural composite materials, where sensing is the most fundamental aspect of a smart structure.

8.2.6. Other materials

In the past decades, perovskite manganites have attracted much attention with the so-called magnetoresistive (MR) [302] and magnetocaloric (MC) effects [303]. Recently, the MI effect has also been reported in these materials, such as La–Ca–Mn–O [304–306], La–Sr–Mn–O [307–310] and La–Ba–Mn–O [311–313]. It was shown that, in the same perovskite manganite, the MI effect was much larger than the MR effect [304]. This is because the change of the magnetic reactance is much larger than that of the resistance under the same applied magnetic field [305]. This indicates that perovskite manganites using the MI effect may be more beneficial for sensor technology than those using the MR effect. It has also been shown that, for perovskite manganites, the temperature and frequency dependence of MI is likely to be related to the ratio of Mn^{3+}/Mn^{4+} and the magnetic phase [304–313]. In fact, the temperature dependence of MI was similar to that of MR [305]. For perovskite manganites, an applied magnetic field, not only decreases the transverse permeability, but also reduces the electrical resistivity by aligning the local spins and varying the transfer integral t_{ij}. Due to the co-existence of ac MI and dc MR, the observed MI effect in perovskite manganites can originate from the combined effects of double-exchange interaction, electro–phonon coupling and skin effect [304–306]. This reflects the complex nature of MI phenomena in manganite materials.

Recently, the MI effect has been reported in ferrite materials, such as ZnNi-ferrite encapsulated NiFe microspheres [314] and MnZn ferrite [315]. The MI ratio was quite small for the former sample, but a value of 61.2% was observed for the MnZn ferrite sample at a frequency of 4 MHz. This is not only because of the field induced permeability variation, but also due to the eddy current effect, the high-frequency loss and the magnetic resonance [315]. In addition, some highly textured FeSi alloys [316–318], Fe flakes [319], FeAg granular alloys [320], crystalline Mumetal [321] and Heusler compounds [322] have been found to show a GMI effect. Most interestingly, the maximum GMI value of 310% and the magnetic response of 20%/Oe were obtained in a crystalline Mumetal sample, when subjected to appropriate annealing.

8.3. Nominated GMI materials for sensor applications

A wide variety of GMI materials are currently available for practical GMI sensor applications. Table 3 summarises several materials that possess a high GMI ratio and magnetic response and are promising for making high-performance GMI sensors. Appropriate selection is dependant upon specific requirements, such as its field sensitivity, working frequency range, size and thermal stability. The ultra-high sensitivity of GMI to external dc magnetic field (down to 10^{-8} Oe) can be used for magnetic field sensors and other sensors based on the change of a local magnetic field. It should be emphasised that not only the GMI ratio (η) and the magnetic response (ξ), but also the particular shape of the $\eta(H)$ curve, are important for high-performance sensor applications. In this context, the longitudinal weak-field-annealed amorphous ribbons [314–322] and amorphous wires subjected

Table 3
Candidate materials for GMI sensors

Materials	Comment	$H_{\max}$ (Oe)	η (%)	ξ (%/Oe)	Frequency (MHz)	Reference
$Co_{68}Fe_{4.35}Si_{12.5}B_{15}$	Conventional amorphous wire	180	1200	–	14.2	[204]
$(Co_{94}Fe_6)_{75}Si_{10}B_{15}$	Amorphous homogeneous microwire	10	125	50	3.22	[151]
$Co_{68.25}Fe_{4.5}Si_{12.25}B_{15}$	Amorphous microwire under Joule annealing	125	600	320	15	[129]
$Co_{83.2}B_{3.3}Si_{5.9}Mn_{7.6}$	Amorphous microwire under dc current	1	7.8	15.6	1	[231]
$Co_{68.2}Mn_7Si_{10}B_{15}$	Amorphous microwire	50	153	65	30	[147]
$Fe_{73.5}Si_{13.5}B_9Cu_1Nb_3$	Conventional wire annealed at 600 °C for 1 h	100	200	–	0.5	[16]
$Fe_{73.5}Si_{13.5}B_9Cu_1Nb_3$	Glass-covered microwire under conventional annealing	25	25.5	8.9	2	[130]
$Fe_{89}B_1Si_3C_3Mn_4$	Annealed at 350 °C for 1 h	300	70	–	4000	[243]
CoP/Cu/CoP electrodeposited layers	Electrodeposited technique	30	190	26	1	[64]
CoP/Cu composite wire	Electrodeposited technique	100	534	21	10.7	[247]
NiFe/Cu composite wire	Electroplated in magnetic field	45	370	47.5	1	[68]
NiFe/Cu composite wire	Joule annealing	45	1100	218	4	[249]
FeNiCo/CuBe composite wire	Electroplated technique	50	1200	–	4	[248]
$Co_{70}Fe_5Si_{15}Nb_{2.2}Cu_{0.8}B_7$	Ribbon under field-annealing in air	2	50	125	0.1	[240]
$Co_{70}Fe_5Si_{15}Nb_{2.2}Cu_{0.8}B_7$	Ribbon under field-annealing in air	2	106	35	1	[240]
$Co_{70}Fe_5Si_{15}Nb_{2.2}Cu_{0.8}B_7$	Amorphous ribbon annealed at 300 °C for 25 min	50	513	144	4	[254]
$Fe_{73.5}Si_{13.5}B_9Cu_1Nb_3$	Amorphous ribbon annealed at 550 °C for 3 h	150	400	37	4.5	[94]
$Fe_{71}Al_2Si_{14}B_{8.5}Cu_1Nb_{3.5}$	Amorphous ribbon annealed at 540 °C for 45 min	100	640	40	5	[254]
$Fe_{84}Zr_7B_8Cu_1$	Amorphous ribbon annealed at 550 °C for 1 h	75	1100	40	4.6	[170]
$Fe_{73.5}Si_{13.5}B_9Cu_1Nb_3$	Nanocrystalline sputtered film	50	80	–	500	[276]
NiFe/Au/NiFe multilayered film	RF-sputtered	65	150	30	300	[293]
NiFe/Ag Multilayered film	RF-sputtered	150	250	12	18000	[290]
FeSiBCuNb/Cu/FeSiBCuNb Sandwiched film	RF-sputtered	70	1733	87	0.1	[275]
FeNiCrSiB/Cu/FeNiCrSiB Sandwiched film	RF-sputtered	70	77	7.2	13	[81]
CoSiB/Cu/CoSiB Sandwiched film	RF-sputtered	9	440	49	10	[287]
CoSiB/SiO_2/Cu/SiO_2/CoSiB Sandwiched film	RF-sputtered in magnetic field	11	700	304	20	[286]
FeSiBCuNb/ SiO_2/Cu /SiO_2/ FeSiBCuNb Sandwiched film	RF-sputtered	60	32	4	5.45	[294]

Table 3 (*continued*)

Materials	Comment	$H_{\max}$ (Oe)	η (%)	ξ (%/Oe)	Frequency (MHz)	Reference
Mumetal alloy	Annealed at 580 °C for 40 min	115.5	310	20	0.6	[321]
Co-based amorphous ribbon/Cu/Co-based amorphous ribbon	Trilayer microstructure	20	830	–	0.28	[162]
$Co_{70.3}Cr_3Fe_{3.7}B_{10}Si_{13}$/polymer composites	Magnetic microwires embedded in a polymer–matrix	50	470	43	10	[156]

to dc bias current [304–313] are promising candidate materials for producing auto-biased linear field sensors.

9. GMI sensors and their applications

9.1. Types of GMI sensors

Since GMI changes as a function of external dc magnetic field or applied dc/ac current, it is possible to design GMI-based sensors that can measure either magnetic fields or dc/ac currents. GMI is also sensitive to applied stress, and this provides a new opportunity for developing stress sensors. These sensors will be briefly described and evaluated below.

9.1.1. Magnetic field sensors

A typical magnetic sensor based on the GMI effect (or the so-called GMI sensor) was designed and produced by Mohri et al. [323]. Continuous efforts have been devoted to improving the sensitivity of the sensor by optimising the processing parameters and/or the design of the electrical circuit [324–332]. Detailed investigation of how the processing parameters can be controlled, as well as the influences of these parameters on the performance of a designed GMI sensor, can be found in Refs. [323,327]. In these sensors, the sensing elements can be amorphous wires [323,327,328], thin films [325,326,329], or ribbons [330]. They can be used for measuring or tracking the presence of both homogeneous and inhomogeneous magnetic fields. A variety of GMI sensors using amorphous wires have been designed and developed by the Aichi Steel Corporation in Japan for a wide range of technological applications [328]. A photograph of a MI sensor using a Co-based amorphous wire is shown in Fig. 40 [328]. GMI sensors provide several advantages (e.g., low power consumption, small dimension) over conventional magnetic sensors (see Table 4, for comparison), but their high sensitivity is the most important of these. Using a CoNbZr thin film as the sensing element, Yabukami et al. [329] have achieved an extremely high resolution of magnetic field detection of 1.7×10^{-8} Oe at 500 kHz. This resolution is even higher than that obtained from the flux gate (FG) sensor (see Table 4). The head length of a GMI sensor (~1 mm) is about 1/20th of that of a FG sensor (~20 mm). Furthermore, the resolution for detecting localised magnetic-pole fields is over 20 times higher for the GMI sensor than that for the FG sensor [327]. In addition, the GMI sensor has better thermal stability compared to conventional sensors [325,326,328,332]. The variation

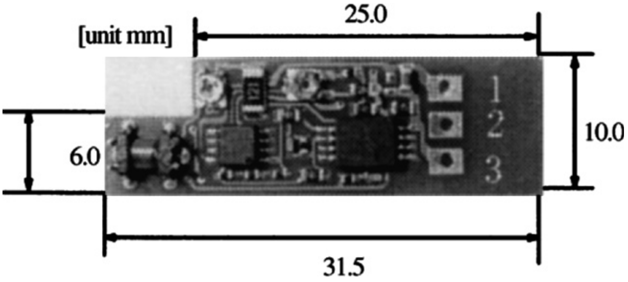

Fig. 40. Photograph of a MI sensor (reproduced with permission from Elsevier [328]).

Table 4
Comparison of magnetic sensors

Sensor type	Head length	Detectable field (Oe)	Response speed	Power consumption
Hall	10–100 μm	$1–10^6$	1 MHz	10 mW
GMR	10–100 μm	$0.1–10^2$	1 MHz	10 mW
GMI	1–2 mm	$10^{-8}–10^2$	1–5 MHz	10 mW
Flux gate	10–20 mm	$10^{-6}–10^2$	5 kHz	1 W

in GMI sensor output with temperature is about one-third of a conventional thin film sensor [325]. Particularly, the GMI sensors, using Co-based amorphous wires have good thermal stability over a wide temperature range between −40 °C and 85 °C, enabling the sensor to make reliable outdoor measurements [328].

9.1.2. Passive, wireless magnetic field sensors

By combining GMI sensors and the surface acoustic wave (SAW) transponder devices, Hauser et al. [333] have designed a new type of wireless sensor for measuring magnetic fields. Fig. 41 shows a diagram of a passive, wireless magnetic field sensor. In this device, the GMI sensor is coupled with the second port of the SAW transponder, and the circuit is adjusted to the resonance of the transducer's capacitance. Tuning the resonance for one octave in the frequency domain, by applying a magnetic field to the GMI sensor, can yield a sufficient effect for radio request readout. The main advantage of this sensor is that it can

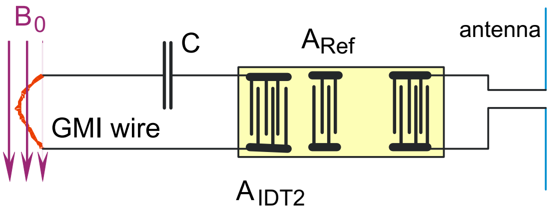

Fig. 41. Passive, wireless magnetic field sensor (courtesy Hans Hauser).

be used for applications where a magnetic field has to be measured without physical contact and where a wired power supply is not feasible for the sensor [333,334].

9.1.3. Current sensors

Using a nearly zero magnetostrictive Co–Fe–Si–B amorphous wire, Valensuela et al. [335] have successfully produced a current sensor based on the GMI effect. In this sensor, the dc current to be monitored flows through a solenoid, and the magnetic field produced by this solenoid on the wire leads to a controlled decrease of its impedance response. Consequently, the axial magnetic field dependence of impedance is used to accurately measure the dc current. The advantage of this sensor is its reduced size, since the sensing element is a wire. In another work, Rheem at al. [223] developed a high-sensitivity current sensor based on the asymmetric GMI effect and using a field-annealed Co-based amorphous ribbon as a sensing element. The sensor output voltage increases with applied current up to 1 A with a high degree of linearity. Due to the asymmetric characteristic of the GMI effect, this sensor can determine the direction of currents but only dc currents. Moreover, these GMI current sensors are suitable for dc current measurements but not for ac current measurements. Therefore, further work is required to develop GMI current sensors that can measure both dc and ac currents [336]. In this context, a prototype of a GMI current sensor based on the GMI effect has been designed and produced [337]. This sensor allows accurate measurement of the magnitude of both ac and dc currents, and the basic setup is displayed in Fig. 42. The voltage output signal of the GMI current sensor shows a consistent trend for both ac and dc current measurements. This sensor is appropriate for non-contact and non-coil dc/ac measurements, which are important for many engineering applications, where wire-contact measurement cannot be performed.

9.1.4. Stress sensors

Based on the applied stress dependence of the GMI effect, Tejedor et al. [338] proposed the development of stress sensors using Co-based amorphous ribbons. For conventionally annealed ribbon, the maximum stress sensitivity of the effective anisotropy field of $\sim$214 MPa/Oe is found at a frequency of 1 MHz, while for the stress-annealed ribbon the sensitivity is 167 MPa/Oe, and the impedance varies with applied stress at about 100 MPa/Ω [338].

A magnetoelastic sensor using a Co–Mn–Si–B amorphous microwire has been introduced by Cobeno et al. [190]. Under a load of 3 g, the change of voltage across the microwire was found to be about 3.5 V [190]. This high sensitivity of GMI ratio to a small mechanical load is very promising for practical applications. Recently, utilising Co–Fe–Si–B amorphous ribbons and a unique magnetic field bias, Bowles et al. [339] developed a low-cost and high proportional change stress sensor. This stress sensor, combined with a battery-free analogue tag, allows the data to be transmitted inductively to a remote transceiver without a hardwire connection. These stress-induced impedance sensors have several advantages over conventional stress sensors. For instance, a semiconductor strain gauge usually shows only a 15% change in resistance when strained to its maximum recommended stress level, while the amorphous alloy sensor has demonstrated a large change in inductance of 315% when strained to its maximum working level [339]. In this context, the discovery of the giant stress-impedance (GSI) effect in several amorphous wires [188,189] and ribbons [180,339] provides a new opportunity for developing novel stress-sensors.

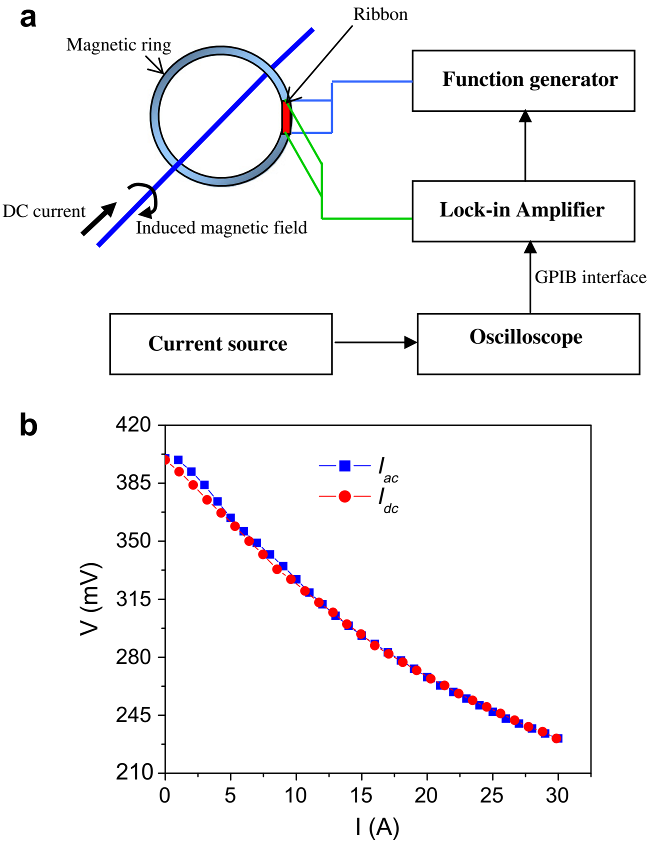

Fig. 42. (a) A basic setup of a GMI current sensor using an amorphous ribbon as a sensing element. (b) The output signals of the GMI current sensor for both ac and dc measurements.

9.2. Applications of GMI sensors

Many industrial and engineering applications of GMI sensors have been proposed and realised to date, including computer disk heads, rotary encoders, pin-hole detectors, displacement detection sensors, direction sensors for navigation (electronic compass), field sensors, biomedical sensors, car traffic monitoring, antitheft systems and so forth. Here, we briefly describe some GMI-based sensing devices of practical importance.

9.2.1. Target detection and processes control

GMI sensors can be used to detect the presence or passage of moving objects, simply by fixing a small permanent magnet on the object [340]. Detection is observed as a decrease in the ac voltage on the wire's ends. Such devices have been used to monitor and control many industrial processes and the advantages of using GMI sensors include simplification and low fabrication costs [1–3]. Monitoring and control systems employing GMI field sensors have proven superior to those based on optical devices, especially for industrial processes involving (non-magnetic) dusty atmospheres. From this perspective, the passive and wireless magnetic field sensor is best suited for remote control of industrial processes [333]. Recently, a so-called nano-GMI sensor has been developed, and has been used in an anti-lock brake system (ABS) and for the measurement of electric injector speeds for the automotive and truck industries [341].

9.2.2. Space research and aerospace applications

The role of magnetic sensors is important in the field of space physics research [1–3]. For instance, the accurate measurement of the ambient magnetic field vector and its orientation in space can be achieved through the use of highly sensitive magnetic sensors such as GMI sensors. The space magnetic instruments utilising the GMI sensors can be used onboard spacecraft to precisely measure magnetic fields in space. These sensors can also be used to eliminate the sources of stray magnetic fields generated by the complex systems of mechanical, electrical and electronic components onboard the spacecraft [3].

Magnetic sensors also play an important role in aerospace applications. One example is the precise determination of the gear-tooth position in aircraft-engines that can be achieved with the use of high-sensitivity magnetic sensors like GMI sensors [1]. This gear-tooth sensor detects the presence and absence of a gear tooth made of a ferrous material. It detects a fixed level of magnetic field when no magnetic material is present. When a tooth moves over the sensor, the ferrous material acts a flux concentrator, thus leading to a change of the magnetic flux that can be detected by the sensor. Consequently, the sensor can be used to control the speed of the gear as well as determine the gear-tooth position precisely. Furthermore, the development of non-contact switching systems utilising magnetic sensors has enabled improved flight safety standards. In this case, GMI sensors are ideal because of their ultrahigh sensitivity and reduced size.

9.2.3. Electronic compasses and automobile uses

Electronic compasses using flux gate (FG) sensors are being used for a wide variety of engineering and electronic devices such as in cars, small boats and for mobile phones. However, the main disadvantages of the electronic compasses using FG sensors are their large size and high power consumption. These problems have recently been overcome by the introduction of GMI sensors into electronic compasses [328]. When compared with an FG sensor, a GMI sensor has much reduced size and lower power loss (see Fig. 43). The Aichi Steel Corporation has recently designed and produced an ultrasmall one-package compass device (i.e., the so-called two-axis electronic compass AMI201), which allows the sensing of geomagnetic fields with two-axis GMI sensors [342]. This product won a Sensors Expo Silver Award at the recent US Sensors Expo & Conference. For mobile phone applications, the Aichi Steel Corporation has also developed a new device, i.e., the so-called G^2 motion sensor, using the GMI effect to detect both geomagnetism and gravity. These G^2 motion sensors are being widely used in mobile devices by the Korean mobile phone manufacturer and by the Japanese Vodafone KK Corporation [342].

9.2.4. High-density information storage

In modern computers, magnetic sensors form an essential part of magnetic storage disks and tape drives [1,3]. In these devices, the reading module usually comprises a giant magnetoresistive (GMR) sensor, which uses a multilayer film structure consisting of magnetic and non-magnetic layers. The writing module operation induces local magnetic

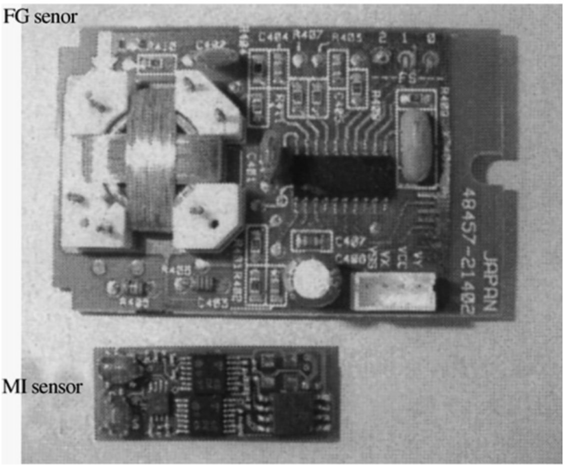

Fig. 43. Comparison of flux gate (FG) and magnetoimpedance (MI) electronic compasses. The size of MI sensor is much smaller (reproduced with permission from Elsevier [328]).

moments in the bit areas of the hard disk magnetic layer. Bits with remanent magnetisation cause a measurable change in the resistance of the GMR sensor of the reading module, which enables the two levels of digital signal to be distinguished. Because the sensitivity of a GMI sensor is much higher than that of a GMR sensor (see Table 4), thin film GMI sensors will be of much interest in future high-density magnetic recording technology [343].

9.2.5. Traffic controls

Accidents and jams present serious problems in our daily transportation systems; this is partially due to the lack of automatic control and monitoring systems. Many systems, such as ultrasonic sensors and video cameras, have been used for monitoring traffic conditions. However, these devices are quite expensive and sometimes inconvenient for practical use. Recently, Uchiyawa et al. [344] proposed and developed, a new car sensing system, using an amorphous wire GMI sensor built into a disk set on the road. In this device, the role of the GMI sensor is to detect stray fields from the car body as it passes above the disk. The speed and length of a car can be estimated by processing the signals from two GMI sensors. Using a microcomputer, the disk system can record the length, the velocity and the time for about two thousand cars. The advantages of this sensing technique are that it can be easily installed, it is insensitive to weather conditions, it does not obstruct the stress surface, and it has very high reliability.

Using GMI sensors and magnet markers, magnetic guidance systems have recently been designed and developed for use in the automated highway system (AHS). One example is that of a car, which could be driven automatically using this magnetic guidance system (see Fig. 44) [328]. Research into automatic car control has mainly been carried out in Japan and has been led by the Aichi Steel Corporation. In this research, magnetic markers are fixed into the road, and GMI sensors are placed on the car to sense the position of these markers. By travelling from marker to marker, the car can automatically drive without the

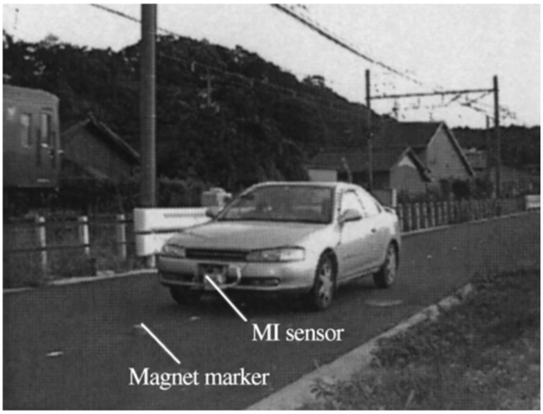

Fig. 44. Automated highway system (AHS) experiment with a MI sensor: this car drives automatically without a driver (reproduced with permission from Elsevier [328]).

aid of a driver. By similar priciples, these magnetic guidance systems can be used in industrial processes involving automatic control of product transportation [342]. In addition, the Aichi Steel Corporation has produced switch-type GMI sensors for use in magnetic encoders. These sensors are simple and less expensive than conventional sensors [328].

9.2.6. Non-destructive crack detection

Magnetic methods of non-destructive evaluation have been widely used either to monitor material state and properties or to find defects. For instance, the eddy current method and the residual magnetic field technique are often used to prevent the catastrophic fracture of mechanical parts in machines. In this context, GMI sensors have been proposed for detecting magnetic fields created by current passing through conductors or localised magnetic fields [323–332]. The lack of material continuity resulting from a crack produces a disturbance in the material's magnetic field, and the magnitude of this disturbance is determined by the size and shape of the crack. A GMI amorphous wire sensor has been used to capture cracked regions in materials [345].

9.2.7. Biological detection

In biomedical applications, magnetic methods have proved useful for disease treatments and improving the health of human beings. For instance, magnetic trackers are used to determine the position of medical tools inside the body (e.g., endoscope, colonoscopy, and biopsy needle) and to observe biomechanical motions [3]. Magnetopneumography is a magnetic method that can detect ferromagnetic dust deposited in human lungs by using its magnetic moment after dc magnetisation. In fact, the sources of magnetic induction in biological systems (e.g., body, human brain, and animals) are found to be very small and the magnetic field range is of 10^{-10}–10^{-5} Oe. In order to detect such small fields, a detector is required to have a high sensitivity. A miniature GMI sensor should be ideal, because it can detect magnetic fields as small as 10^{-8} Oe.

Recently, Kurlyandskaya [346,347] have designed and produced a new GMI-based biosensor prototype using Co-based amorphous ribbons with a working frequency range of 0.5–10 MHz at a current intensity of 60 mA. They have demonstrated that the GMI effect can be used to probe the electric features of the ribbon magnetic electrode surface modified by human urine. Totsu et al. [348] have developed a three-axis GMI sensor system that allows the detection of position and orientation of a catheter tip to a high degree of accuracy. Chiriac et al. [349] have designed a magnetic sensing device utilising the GMI sensor for biological detection, such as fast identification and diminution of the direction threshold of pathogens or other targeted biomolecules (e.g., DNA, RNA, antibodies, metabolites, etc.). Furthermore, the GMI sensor has been used for determining spin rate of a rotating body in the presence of an external magnetic field [350]. Compared with classical methods (e.g., electrical, mechanical, and optical), which are costly, time-consuming and have a high detection threshold, the magnetic method provides several advantages, including rapid results, multi-analyte detection, low cost and reduced waste handling. Other biomedical applications using highly sensitive GMI sensors have been proposed by the Aichi Steel Corporation, and this will lead to the further exploration of GMI sensors in the near future.

9.2.8. Magnetic anomaly detection and geomagnetism

The magnitude of the Earth's magnetic field varies from 10^{10} to 10^{-4} Oe when going from the core to the crust, and the magnitude of the Earth's surface magnetic field varies between 10^{-4} and 1 Oe depending upon the specific geometry. The detection and orientation of the Earth's magnetic field have found wide applications in petroleum and minerals exploration and shielding used for degaussing of high performance monitors [3,328]. However, because the Earth's surface magnetic field is small, its detection is a difficult task and requires a highly sensitive magnetic sensor, which can be fulfilled using a GMI sensor. A GMI-based sensing element (e.g., wire or microwire) as small as 1 mm can be used to detect magnetic anomaly and localised weak magnetic fields. Many devices utilising GMI sensors have been used in antitheft systems and in magnetic marking and labelling technology. The GMI sensor can be used to eliminate the error of measurements due to the effect of the Earth's magnetic field, and to detect stray magnetic fields created by engines and machines during their operating processes [1,3,10].

9.2.9. Stress sensing applications

Altering GMI response with mechanical stress provides potential for developing strain sensors. An important application of these could be in toque measurement systems, which have proved useful to develop based on the GMI effect. Uchiyawa and Meydan [351] have designed a new GMI torque sensor module with FM transmitter, which allows the detection of torque from a rotating shaft. This transducer has several advantages including a simple construction without the torsion bar, high accuracy, low power consumption and easy installation. In this context, the new findings of the giant stress-impedance (GSI) effect in amorphous wires or ribbons have opened up the opportunity of developing strain sensors for accurate measurements of torque [180,188,189,339]. For instance, stress-induced impedance sensors utilising amorphous alloys have proved useful for wireless, battery-free applications [339]. A demonstration unit has recently been developed for vehicle tyre pressure monitoring (see Fig. 45). A quick response acceleration sensor has been constructed using the stress-impedance (SI) element of amorphous wires combined with a CMOS IC multivibrator [352]. This sensor has a very high sensitivity and has been used for sensing the seismovibration of bridges due to cars passing.

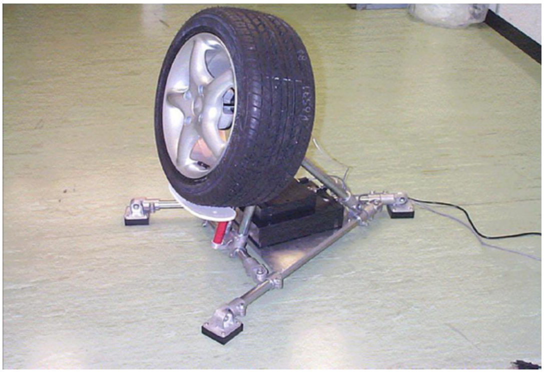

Fig. 45. Tyre Pressure Monitoring System incorporating the amorphous alloy wireless, battery-free sensor (courtesy A. Bowles [339]).

9.3. GMI as a research tool

In addition to the above-mentioned applications, many other applications of GMI sensors can be found in Refs. [3,6,7,10]. In these cases, magnetic sensing devices utilising GMI sensors have been used to measure variables, instead of measuring magnetic field or current. However, some of these devices use principles similar to those of magnetic field sensors.

In a different area, GMI sensors have been employed for research purposes. Using a GMI sensor in its sensing section, a Milli-Gaussmeter (a high precision magnetic field measuring instrument) is able to measure submilligauss minute magnetic fields [342]. A compact magnetic field canceller device using highly sensitive GMI sensors has been produced by the Aichi Steel Corporation, which allows precise control of 3D external magnetic fields [342]. Furthermore, GMI has been used as a research tool to investigate intrinsic and extrinsic magnetic properties of novel artificially grown soft magnetic materials [9]. Using the correlation between the domain structure, magnetic properties and the GMI effect, several important magnetic parameters (e.g., anisotropy field, saturation magnetisation, and magnetostriction) can be deduced [10,16,25,33,97,121]. It has also been shown that the changes in the GMI curve can be used to evaluate the formation and growth of domain structures in magnetic wires [6,7,66,71,90], ribbons [93,94,183] and thin films [274–277].

When investigating the annealing-temperature dependence of GMI in Fe–Si–B–Cu–Nb amorphous ribbons, Phan et al. [87] established a correlation between the magnetic softness and the GMI effect. Accordingly, GMI profiles were used to determine the magnitude of the anisotropy field of Fe–Si–B–Cu–Nb amorphous ribbons as a function of annealing temperature. Similarly, GMI profiles were also used to evaluate the magnitude of the anisotropy field of Fe–Nb–B amorphous ribbons as a function of iron content [9]. Interestingly, the anisotropy fields determined from GMI profiles coincide with those determined from magnetic hysteresis loops. In relation to material structure, the authors [87] have also revealed that the study of annealing-temperature dependent GMI profiles, can provide an alternative way of assessing the magnetic exchange coupling between α-Fe(Si) nanocrystalline grains through the amorphous boundaries in Fe-based nanocrystalline materials. Within a theoretical model of GMI using the ferromagnetic resonance (FMR) procedures, Menard et al. [14,31,32] were able to deduce several important parameters such as gyromagnetic ratio, anisotropy field and saturation magnetisation of magnetic wires. These values show close agreement with those obtained by conventional methods [32]. Based upon the stress dependence of GMI, several magnetoelastic parameters (e.g., saturation magnetostriction constant) were deduced for Co-based amorphous wires [188–190] and ribbons [180,338].

GMI has been useful for the evaluation of magnetisation dynamics that involve domain wall motion and magnetisation rotation processes within magnetic materials [25,29]. When investigating the GMI effect of perovskite manganites, Fu et al. [304] revealed that the specific features of impedance provide an alternative way of sensing the complex phase states of these typical materials. Indeed, Patanjali et al. [310] have demonstrated the existence of secondary transitions at high temperatures in a double perovskite $La_{1.2}Sr_{1.8}Mn_2O_7$ through GMI measurements. It is worthy to note that this feature was not observed by static resistivity and magnetisation measurements [310].

10. Concluding remarks and future perspectives

The present paper provides the state-of-the-art of the processing-domain structure-magnetic properties of GMI materials and the development of high-performance GMI sensors. The concluding remarks are as follow:

(i) Existing theoretical models of GMI are developed for specific materials and/or certain frequency ranges. None of them can explain all GMI features in a wide frequency range (from a few kHz up to GHz). It is believed that, to assess the underlying mechanisms of GMI for a variety of magnetic materials, further theoretical models should be developed on the basis of the identified domain structures of the materials.

(ii) A GMI effect should exist in magnetic materials having: (i) low resistivity; (ii) high magnetic permeability; (iii) high saturation magnetisation; and (iv) a low damping parameter. Therefore, the Co-based amorphous and Fe-based nanocrystalline materials (wires, ribbons, and thin films) are good candidates for GMI sensor applications. Fe-containing materials are much cheaper than the Co-containing ones. Magnetic composite materials containing amorphous wires are not only good for GMI sensor applications, but are also promising for structural and functional applications.

(iii) Techniques such as in-rotating water spinning, glass-coated melt spinning, electrodeposition, single-roller melt spinning, and sputtering methods have been effective for the production of amorphous magnetic wires, ribbons and thin films. Nanocrystalline materials can be obtained by annealing their corresponding amorphous alloys (wires, ribbons, and thin films) under optimised treatment conditions (i.e., the optimal annealing temperature and time). Such optimisations have been made, based on systematic structural analyses such as X-ray diffraction, differential scanning calorimetry, scanning electron microscopy and transmission electron microscopy.

(iv) The measuring parameters (e.g., ac current, dc magnetic field, and frequency) directly affect the measured value of GMI and so the selection of appropriate measuring parameters becomes extremely important in designing practical GMI sensors.

Depending on the type of GMI material, the amplitude of an applied ac current and the maximum dc magnetic field applied to saturate the magnetoimpedance are different, and for practical uses, they should be as small as possible. Furthermore, because the magnitude of GMI and its sensitivity varies with measuring frequency, it is necessary to select suitable a working frequency range for a given material. At relatively low frequencies, it should be noted that an SP behavior of a GMI is often observed and is useful for practical applications. In contrast, the DP behavior of a GMI observed in the high-frequency range is undesirable.

(v) A conventional annealing method is useful for improving both magnetic softness and the GMI effect in Fe-based materials and in Co-based materials at relatively low annealing temperatures due to partial internal stress relief. The circumferential/transverse magnetic anisotropy plays a crucial role in improving GMI response for a given material form (e.g., wire or ribbon/film). In the case of wires, a circumferential magnetic anisotropy can be created by the application of a current along the wire (e.g., the dc current-annealing or Joule-annealing method). For ribbons and films, the transverse magnetic anisotropy can be induced by annealing with an applied transverse magnetic field (i.e., the field-annealing method). In Co-based amorphous wires or ribbons, the application of a tensile stress during annealing (i.e., the stress-annealing method) may lead to an improvement in the GMI response. In general, for negative-magnetostrictive materials, the application of such a tensile stress may induce transverse anisotropy, thereby increasing GMI. In amorphous glass-covered wires, the glass cover itself produces this kind of stress. Any fluctuation of local magnetic anisotropy will lead to a reduction in the GMI effect. In this case, the use of homogenous materials (e.g., electrodeposited wires and films) should be recommended. Although a proper thermal treatment can improve the GMI effect and significantly reduce the GMI aftereffect, this treatment also leads to a deterioration in the material's mechanical properties. Therefore, the sample should ideally be in its near-net shape before such an annealing treatment is performed. Neutron irradiation has been shown to improve the magnetic softness and the GMI response of Fe-based amorphous alloys while maintaining their excellent mechanical properties. This is of practical importance, especially for sensor applications in a neutron-irradiated environment.

(vi) Magnetic hysteresis of GMI is undesirable for practical sensor applications. To overcome this problem, GMI materials must be homogeneous (e.g., electrodeposited wires and films). Alternatively, hysteresis can be removed by annealing the as-cast amorphous samples under the application of an external stress and/or a magnetic field. On the other hand, asymmetry of GMI (AGMI) is of practical importance in constructing auto-biased linear field sensors and magnetic sensing devices. Among the methods developed for producing AGMI, that due to dc bias current is useful, because the asymmetry can be controlled by the dc bias current and the AGMI can be easily optimised. However, application of a dc bias current increases electric power consumption. Another method – AGMI due to ac bias field is not recommended, since it is related to the Matteucci effect and only a small improvement in the asymmetry can be achieved. Perhaps the most promising method is the AGMI due to bias exchange, which can achieve the highest magnetic response of GMI without the need of an additional electric power supply. The use of Co-based ribbons or wires is recommended for producing the highest magnetic response.

(vii) GMI sensors are superior to conventional magnetic sensors (e.g., Induction, Hall-effect, and GMI sensors). It is likely that stress sensors based upon the GMI effect and/or the giant stress-impedance (GSI) effect will provide a wider range of technological applications compared to conventional stress sensors.

From a fundamental perspective, a theoretical study of GMI with respect to the high-frequency range (between several MHz and GHz) remains to be conducted. The development of new materials, as well as special thermal treatments, is necessary to further improve the GMI effect, because the maximum value of GMI effect experimentally observed is still much smaller than the theoretically predicted value. On the technological side, in order to produce highly sensitive GMI sensors with reduced dimensions, electrical circuits need to be optimised by integrating amorphous and nanocrystalline materials in the form of films, wires and ribbons on electronic circuit boards.

Furthermore, GMI materials offer exciting new opportunities in the development of smart structural composites with embedded multifunctionality. Some examples are given below:

- A new class of magnetic composite material, which consist of amorphous magnetic wires embedded in a polymer–matrix [156] or in a dielectric matrix [353,354], can potentially be useful for specific engineering applications. For instance, due to a strong field dependence of the permittivity in the vicinity of the antenna resonance, it is possible to use the GMI effect to design field-controlled composites and band-gap structures. The stress dependence of GMI in the high-frequency regime ($\sim$GHz) may allow the production of microwave stress-tuneable composite materials containing short magnetic wires, and consequently, the structural stress can be monitored using the microwave contrast imaging method [355].
- The importance of smart materials and structures lie in their relevance to hazard mitigation, structural vibration control, structural health monitoring, transportation engineering, thermal control, and energy reduction. The incorporation of amorphous microwires into a glass fibre glass–fibre/polymer composite for the production of a ‘smart structural’ material is of significant interest [356]. Further applications of existing fibre composite materials are being considered by the introduction of magnet-sensing functions into the composites and their structures. Sensing is regarded as the most fundamental aspect of a smart structural system.

Acknowledgements

The authors wish to acknowledge their collaborators: Prof. Seong-Cho Yu (Chungbuk National University, South Korea), Prof. Cheol Gi Kim (Research Center for Advanced Magnetic Materials, South Korea), Prof. Heebok Lee and Dr. Le Anh Tuan (Kongju National University, South Korea), Prof. Nguyen Chau and Mr. Nguyen Duc Tho (Center for Materials Science, Vietnam) Prof. Nguyen Hoang Nghi (Hanoi University of Technology) and Prof. Manuel Vázquez (Institute of Materials Science, Spain). The authors would like to thank Prof. Hans Hauser (Vienna University of Technology, Austria), Dr. Arcady Zhukov (Basque Country University, Spain), Dr. Larin Vladimir (Microfiber Technology Industry, Modova) and Dr. Adrian Bowles (QinetiQ, United Kingdom) for providing the original data. The authors are indebted to the Microfiber Technology Industry (MFTI) (www.microwires.com) for the provision of some magnetic microwires. Sepecial thanks are also due to Paul Harper and Sandy Mitchell for their aid in reading and editing the manuscript. This work was partially supported by the EPSRC under Grant No. EP/C532392.

References

[1] Lenz JE. A review of magnetic sensors. Proc IEEE 1990;78:973–89.

[2] Meydan T. Application of amorphous materials to sensors. J Magn Magn Mater 1995;133:525–32.

[3] Ripka P. Magnetic sensors and magnetometers. Artech House Publishers; 2001.

[4] Panina LV, Mohri K. Magneto-impedance effect in amorphous wires. Appl Phys Lett 1994;65:1189–91.

[5] Panina LV, Mohri K, Uchiyama T, Noda M. Giant magneto-impedance in Co-rich amorphous wires and films. IEEE Trans Magn 1995;31:1249–60.

[6] Vazquez M, Hernando A. A soft magnetic wire for sensor applications. J Phys D: Appl Phys 1996;29:939–49.

[7] Chiriac H, Ovari TA. Amorphous glass-covered magnetic wires: preparation, properties, applications. Prog Mater Sci 1996;40:333–407.

[8] Vazquez M. Giant magnetoimpedance in soft magnetic “wires”. J Magn Magn Mater 2001;226–230:693–9.

[9] Knobel M, Pirota KR. Giant magnetoimpedance: concepts and recent progress. J Magn Magn Mater 2002;242-245:33–40.

[10] Knobel M, Vazquez M, Kraus L. Giant magnetoimpedance. In: Buschow KH, editor. Handbook of magnetic materials, vol. 15. Amsterdam: Elsevier Science B.V.; 2003. p. 1–69 [Chapter 5].

[11] Kraus L. GMI modeling and material optimization. Sens Acta A 2003;106:187–94.

[12] Tannous C, Gieraltowski J. Giant magneto-impedance and its applications. J Mater Sci: Mater Electro 2004;15:125–33.

[13] Landau LD, Lifshitz EM. Electrodynamics of continuous media. Oxford: Pergamon Press; 1975.

[14] Menard D, Britel M, Ciureanu P, Yelon A. Giant magnetoimpedance in a cylindrical magnetic conductor. J Appl Phys 1998;84:2805–14.

[15] Kraus L. Theory of giant magneto-impedance in the planar conductor with uniaxial magnetic anisotropy. J Magn Magn Mater 1999;195:764–78.

[16] Knobel M, Sanchez ML, Gomez-Polo C, Marin P, Vazquez M, Hernando A. Giant magneto-impedance effect in nanostructured magnetic wires. J Appl Phys 1996;79:1646–8.

[17] Beach RS, Berkowitz AE. Giant magnetic field dependent impedance of amorphous FeCoSiB wire. Appl Phys Lett 1994;64:3652–4.

[18] Mohri K, Kohsawa T, Kawashima K, Yoshida H, Panina LV. Magneto-inductive effect (MI effect) in amorphous wires. IEEE Trans Magn 1992;28:3150–2.

[19] Yelon A, Menard D, Brittel M, Ciureanu P. Calculations of giant magnetoimpedance and of ferromagnetic resonance response are rigorously equivalent. Appl Phys Lett 1996;69:3084–5.

[20] Machado FLA, Rezende SM. A theoretical model for the giant magnetoimpedance in ribbons of amorphous soft-ferromagnetic alloys. J Appl Phys 1996;79:6558–60.

[21] Atkinson D, Squire PT. Phenonemological model for magnetoimpedance in soft ferromagnet. J Appl Phys 1998;83:6569–71.

[22] Chen DX, Munoz JL. Theoretical eddy-current permeability spectra of slabs with bar domains. IEEE Trans Magn 1997;33:2229–44.

[23] Chen DX, Munoz JL, Hernando A, Vazquez M. Magnetoimpedance of metallic ferromagnetic wires. Phys Rev B 1998;57:10699–704.

[24] Chen DX, Munoz JL. AC impedance and circular permeability of slab and cylinder. IEEE Trans Magn 1999;35:1906–23.

[25] Betancourt I, Valenzuela R, Vazquez M. Domain model for the magnetoimpedance of metallic ferromagnetic wires. J Appl Phys 2003;93:8110–2.

[26] Yoon SS, Kim CG, Kim HC. The mechanism of magnetic relaxation in Co-based amorphous ribbon determined by permeability spectroscopy. J Magn Magn Mater 1999;203:235–7.

[27] Kim CG, Yoon SS, Yu SC. Decomposition of susceptibility spectra in a torsion-stressed Fe-based amorphous wire. Appl Phys Lett 2000;76:3463–5.

[28] Yoon SS, Kim CG. Separation of reversible domain wall motion and magnetization rotation components in susceptibility spectra of amorphous magnetic materials. Appl Phys Lett 2001;78:3280–2.

[29] Carara M, Baibich MN, Sommer RL. Magnetization dynamics as derived from magneto impedance measurements. J Appl Phys 2000;88:331–5.

[30] Buttino G, Cecchetti A, Poppi M. Domain wall relaxation frequency and magnetocrystalline anisotropy in Co- and Fe-based nanostructured alloys. J Magn Magn Mater 2004;269:70–7.

[31] Menard D, Melo LGC, Brittel MR, Ciureanu P, Yelon A, Rouabhi M, et al. Modeling the magnetoimpedance in anisotropic wires. J Appl Phys 2000;87:4801–3.

[32] Brittel MR, Menard D, Melo LGC, Ciureanu P, Yelon A, Cochrane CW, et al. Magnetoimpedance measurements of ferromagnetic resonance and antiresonance. Appl Phys Lett 2000;77:2737–9.

[33] Machado FLA, de Araujo AEP, Puca AA, Rodrigues A, Rezende SM. Surface magnetoimpedance measurements in soft-ferromagnetic materials. Phys Stat Sol A 1999;173:135–44.

[34] Ménard D, Yelon A. Theory of longitudinal magnetoimpedance in wires. J Appl Phys 2000;88:379–93.

[35] Patton CE. Classical theory of spin-wave dispersion for ferromagnetic metals. Czechoslovak J Phys 1976;26:925–35.

[36] Lofland SE, Baghat SM, Dominguez M, Garciabeneytez JM, Guerrero F, Vazquez M. Low-field microwave magnetoimpedance in amorphous microwires. J Appl Phys 1999;85:4442–4.

[37] Tatara G. Theory of electron scattering by domain wall in nano-wires. J Magn Magn Mater 2001;226–230:1873–4.

[38] Dong C, Chen S, Hsu TY. A simple model of giant magneto-impedance effect in amorphous thin films. J Magn Magn Mater 2002;250:288–94.

[39] Phan MH, Cuong N, Yu SC. Theoretical considerations on the giant magnetoimpedance effect in amorphous ribbons. In: Digests of the 2003 summer conference & Japan–Korea symposium on spintronics, June 19–21; 2003, Busan, Korea. p. 60–1.

[40] Barandiaran JM, Kurlyandskaya GV, Vazquez M, Gutierrez J, Garcia D, Munoz JL. A simple model of the magnetoresistance contribution to the magnetoimpedance effect in thin films. Phys Stat Sol A 1999;171:R3–4.

[41] Kurlyandskaya GV, Barandiaran JM, Vazquez M, Garcia D, Gutierrez J, Vaskovskiy VO, et al. The magnetoresistance contribution to the total magnetoimpedance of thin films: a simple model and experimental basis. J Magn Magn Mater 2000;215–216:516–8.

[42] Davies HA, Lewis BG, Donald IW. In: Mehrabian R, Kear BH, Cohen M, editors. Rapid solidification processing: principles and technologies. Baton, Rouge, LA: Claitor's Pub. Div.; 1978. p. 78–83.

[43] Luborsky FE, Walter JL, Liebermann HH. Engineering magnetic properties of Fe–Ni–B amorphous alloys. IEEE Trans Magn 1979;15:909–11.

[44] Goto T. Fe–B and Fe–Si–B system alloy filaments produced by glass-coated melt spinning. Trans Jpn Inst Met 1980;21:219–25.

[45] Squire PT, Atkinson D, Gibbs MRJ, Atalay SJ. Amorphous wires and their applications. J Magn Magn Mater 1994;132:10–21.

[46] Ohnaka I, Fukusako T, Matui T. Preparation of amorphous wires. J Jpn Inst Met 1981;45:751–62.

[47] Matsumoto T, Ohnaka I, Inoue A, Hagiwara M. Scripta Metall 1981;15:293–306.

[48] Matsumoto T, Inoue A, Hagiwara M. US Patent No. 4, 523, 626; 1995.

[49] Nderu JN, Shinokawa Y, Yamasaki J, Humphrey FB, Ogasawara I. Dependence of magnetic properties of $(Fe_{50}Co_{50})_{78}Si_7B_{15}$ amorphous wire on the diameter. IEEE Trans Magn 1996;32:4878–80.

[50] Ogasawara I, Mohri K. Tension annealing cold-drawn amorphous CoFeSiB wires. IEEE Trans Magn 1990;26:1795–7.

[51] Taylor GF. A method of drawing metallic filaments and a discussion of their properties and uses. Phys Rev 1924;23:655–60.

[52] Taylor GF. Process and apparatus for making filaments, Patented February 24, 1931, United States Patent Office, 1, 793, 529.

[53] Donald IW. Production, properties and applications of microwire and related products. J Mater Sci 1987;22:2261–79.

[54] Goto T, Nagano M, Tanaka K. Tensile strength of copper and iron filaments produced by method of glass-coated melt spinning. Trans Jpn Inst Met 1977;18:209–13.

[55] Wiesner H, Schneider J. Magnetic properties of amorphous FeP alloys containing Ga, Ge, and As. Phys Stat Soli A 1974;26:71–5.

[56] Ulitovsky AV. In: Micro-technology in design of electric devices, vol. 7. Leningrad; 1951. p. 6.

[57] Ulitovsky AV, Maianski IM, Avramenco AI. Method of continuous casting of glass coated microwire. Patent No. 128427 (USSR), 15.05.60, Bulletin. No. 10. p. 14.
[58] Chiriac H. Preparation and characterization of glass covered magnetic wire. Mater Sci Eng A 2001;304–306:166–71.
[59] Larin VS, Torcunov AV, Zhukov A, Gonzalez J, Vazquez M, Panina L. Preparation and properties of glass-coated microwires. J Magn Magn Mater 2002;249:39–45.
[60] Zhukov A, Gonzalez J, Vazquez M, Larin V, Torcunov A. Nanocrystalline and amorphous magnetic microwires. In: Nalwa HS, editor. Encyclopedia of nanoscience and nanotechnology, vol. X. p. 1–22.
[61] Beach RS, Smith N, Platt CL, Jeffers F, Berkowitz AE. Magneto-impedance effect in NiFe plated wire. Appl Phys Lett 1996;68:2753–5.
[62] Sinnecker JP, Garcia JM, Asenjo A, Vazquez M, Garcia-Arribas A. Giant magnetoimpedance in CoP electrodeposited microtubes. J Mater Res 2000;15:751–5.
[63] Yu RH, Landry G, Li YF, Basu S, Xiao JQ. Magneto-impedance effect in soft magnetic tubes. J Appl Phys 2000;87:4807–9.
[64] Sinnecker JP, Knobel M, Pirota KR, Garcia JM, Asenjo A, Vazquez M. Frequency dependence of the magnetoimpedance in amorphous CoP electrodeposited layers. J Appl Phys 2000;87:4825–7.
[65] Garcia JM, Sinnecker JP, Asenjo A, Vazquez M. Enhanced magnetoimpedance in CoP electrodeposited microtubes. J Magn Magn Mater 2001;226-230:704–6.
[66] Garcia JM, Asenjo A, Vazquez M, Yakunin AM, Antonov AS, Sinnecker JP. Determination of closure domain penetration in electrodeposited microtubes by combined magnetic force microscopy and giant magneto-impedance techniques. J Appl Phys 2001;89:3888–91.
[67] Jantaratana P, Sirisathitkul C. Effects of thickness and heat treatments on giant magnetoimpedance of electrodeposited cobalt on silver wires. IEEE Trans Magn 2006;42:358–62.
[68] Li XP, Zhao ZJ, Seet HL, Heng WM, Oh TB, Lee JY. Effect of magnetic field on the magnetic properties of electroplated NiFe/Cu composite wires. J Appl Phys 2003;94:6655–8.
[69] Li XP, Zhao ZJ, Chua C, Seet HL, Lu L. Enhancement of giant magnetoimpedance effect of electroplated NiFe/Cu composite wires by dc Joule annealing. J Appl Phys 2003;94:7626–30.
[70] Hu J, Qin H, Zhang L, Chen J. Giant magnetoimpedance effect in Ag/NiFe plate wire. Mater Sci Eng B 2004;106:202–6.
[71] Atalay FE, Kaya H, Atalay S. Unusual grain growth in electrodeposited CoNiFe/Cu wires and their magnetoimpedance properties. Mater Sci Eng B 2006;131:242–7.
[72] Atalay FE, Kaya H, Atalay S. Giant magnetoimpedance effect in electrodeposited CoNiFe/Cu wires with varying Ni, Fe and Co content. J Alloy Compd 2006;420:9–14.
[73] Atalay FE, Kaya H, Atalay S. Magnetoimpedance effect in electroplated NiFeRu/Cu wire. J Phys D: Appl Phys 2006;39:431–6.
[74] Velleuer J, Munoz AG, Yakabchuk H, Schiefer C, Hackl A, Kisker E. Giant magnetoimpedance in electroplated NiFeMo/Cu microwires. J Magn Magn Mater 2007;311:651–7.
[75] Zhang Z, Wu Q, Zhong K, Yang S, Lin X, Huang Z. The size and space arrangement roles on coercivity of electrodeposited $Co_{1-x}Cu_x$ nanowires. J Magn Magn Mater 2006;303:e304–7.
[76] Wang XZ, Yuan WZ, Zhao Z, Li XD, Ruan JZ, Yang XL. Giant magnetoimpedance effect in CuBe/NiFeB and CuBe/Insulator/NiFeB electroless-deposited composite wires. IEEE Trans Magn 2005;41:113–5.
[77] Wang XZ, Yuan WZ, Zhao Z, Li XD, Ruan JZ, Zhao ZJ, et al. Enhancement of giant magnetoimpedance in composite wire with insulator layer. J Magn Magn Mater 2007;308:269–72.
[78] Chen HS, Miller CE. Centrifugal spinning of metallic glass filaments. Mater Res Bull 1976;11:49–54.
[79] McHenry ME, Willard MA, Laughlin DE. Amorphous and nanocrystalline materials for applications as soft magnets. Prog Mater Sci 1999;44:291–433.
[80] Feldman LC, Mayer JW. Fundamentals of surface and thin film analysis. New York: North Holland; 1986.
[81] Xiao SQ, Liu YH, Dai YY, Zhang L, Zhou SX, Liu GD. Giant magnetoimpedance effect in sandwiched films. J Appl Phys 1999;85:4127–30.
[82] Makhnovskiy DP, Panina LV. Size effect on magneto-impedance in layered films. Sens Acta A 2000;81:91–4.
[83] Panina LV, Mohri K. Magneto-impedance in multilayer films. Sens Acta A 2000;81:71–7.
[84] Zhou Y, Yu JQ, Zhao XL, Cai BC. Giant magnetoimpedance in layered FeSiB/Cu/FeSiB films. J Appl Phys 2001;89:1816–9.

[85] Yoshizawa Y, Oguma S, Ymauchi K. New Fe-based soft magnetic alloys composed of ultrafine grain structure. J Appl Phys 1988;64:6044–6.

[86] Hono K, Zhang Y, Tsai AP, Inoue A, Sakurai T. Atom probe studies of nanocrystalline microstructural evolution in some amorphous alloys. Scr Metal Mater 1995;32:131–40.

[87] Phan MH, Peng HX, Wisnom MR, Yu SC, Chau N. Effect of annealing on the microstructure and magnetic properties of Fe-based nanocomposite materials. Composites: Part A 2006;37:191–6.

[88] Velazquez J, Vazquez M, Hernando A, Savage HT, Wun-Fogle M. Magnetoelastic anisotropy in amorphous wires due to quenching. J App Phys 1992;70:6525–7.

[89] Reininger T, Kronmuller H, Gomez-Polo C, Vazquez M. Magnetic domain observation in amorphous wires. J Appl Phys 1993;73:5357–9.

[90] Usov NA. Stress distribution and domain structure in amorphous ferromagnetic wires. J Magn Magn Mater 2002;249:3–8.

[91] Phan MH, Peng HX, Wisnom MR, Yu SC, Nghi NH, Kim CG. Effect of annealing temperature on permeability and giant magneto-impedance of Fe-based amorphous ribbon. Sens Acta A 2006;129:62–5.

[92] Phan MH, Peng HX, Wisnom MR, Yu SC. Giant magnetoimpedance effect in ultrasoft FeAlSiBCuNb nanocomposites for sensor applications. J Appl Phys 2005;98:014316.

[93] Kolano R, Kuzminski M, Gawior W, Wojcik N. Induced transverse magnetic anisotropy and domain structure in Co-based amorphous ribbons. J Magn Magn Mater 1994;133:321–4.

[94] Guo HQ, Kronmuller H, Dragon T, Cheng ZH, Shen BG. Influence of nanocrystallization on the evolution of domain patterns and the magnetoimpedance effect in amorphous $Fe_{73.5}Cu_1Nb_3Si_{13.5}B_9$ ribbons. J Appl Phys 2001;89:514–6.

[95] Hernando A, Barandiaran JM. Circular magnetisation measurement in ferromagnetic wires. J Phys D: Appl Phys 1978;11:1539–41.

[96] Chiriac H, Ovari TA, Vazquez M, Hernando A. Magnetic hysteresis in glass-covered and water-quenched amorphous wires. J Magn Magn Mater 1998;177–181:205–6.

[97] Pirota KR, Sartorelli ML, Knobel M, Gutierrez J, Brandiaran JM. Influence of induced anisotropy and magnetostriction on the giant magnetoimpedance effect and its aftereffect in soft magnetic amorphous ribbon. J Magn Magn Mater 1999;202:431–44.

[98] Chiriac H, Ovari TA, Marinescu CS. Giant magneto-impedance effect in nanocrystalline glass-covered wires. J Appl Phys 1998;83:6584–6.

[99] Dominguez L, Blanco JM, Aragoneses P, Gonzalez J, Valenzuela R, Vazquez M, et al. Circumferential magnetization processes in CoFeBSi wires. J Appl Phys 1996;79:6539–41.

[100] Zhukova V, Zhukov AP, Usov NA, Blanco JM, Gonzalez J. Magnetization reversal process at low applied magnetic field in a Co-rich amorphous wire. Physica B 2004;343:369–73.

[101] Radkovskaia AA, Sandacci SI, Panina LV, Mapps DJ. Valve-like behavior of the magnetoimpedance in the GHz range. J Magn Magn Mater 2004;272–276:1855–7.

[102] Zhukov A. Domain wall propagation in a Fe-rich glass-coated amorphous microwire. Appl Phys Lett 2001;78:3106–8.

[103] Puerta S, Cortina D, Garcia-Miquel H, Chen DX, Vazquez M. Propagation of domain walls in bistable amorphous wires and microwires. J Non-cryst Solid 2001;287:370–3.

[104] Chiriac H, Hristoforou E, Neagu M, Darie I. On the domain wall propagation in glass covered amorphous wires. Mater Sci Eng A 2001;304–306:1011–3.

[105] Bechet D, Regazzoni G, Dubois JM. Pour la Science 1989;139:30.

[106] Li JCM. In: Liebermann HH, editor. Rapidly solidified alloys: processes, structures, properties, applications. New York: Marcel Dekker Inc.; 1993. p. 379 [Chapter 13].

[107] Chen HS, Sherwood RC, Jin S, Chi GC, Inoue A, Masumoto T, et al. Mechanical properties and magnetic behavior of deformed metal glass wires. J Appl Phys 1984;55:1796–8.

[108] Goto T, Toyama T. The preparation of ductile high-strength Fe-based filaments using the methods of glass-coated melt spinning. J Mater Sci 1985;20:1883–8.

[109] Atalay S, Adiguzel HI, Kamer O. Effect of different heat treatments on magnetoelastic properties of Fe-based amorphous wire. Mater Sci Eng A 2001;304–306:495–8.

[110] Zhukova V, Cobeno AF, Zhukov A, de Arellano Lopez AR, Lopez-Pombero S, Blanco JM, et al. Correlation between magnetic and mechanical properties of devitrified glass-coated $Fe_{71.8}Cu_1Nb_{3.1}Si_{15}B_{9.1}$ microwires. J Magn Magn Mater 2002;249:79–84.

[111] Spaepen F, Tsao SS, Wu TW. In: Haasenm P, Jafee RI, editors. Amorphous metals and semiconductors. Oxford: Pergamon; 1986. p. 365–78.

[112] Fels A, Friedrich K, Hornbogen E. Reinforcement of brittle epoxy resin by metallic glass ribbons. J Mater Sci Lett 1984;3:569–74.

[113] Ohnaka I. Melt spinning into a liquid cooling medium. Int J Rapid Solidif 1985;1:219–36.

[114] Marin P, Hernando A. Applications of amorphous and nanocrystalline magnetic materials. J Magn Magn Mater 2000;215–216:729–34.

[115] Phan MH, Peng HX, Wisnom MR, Chau N, Yu SC, Vazquez M. Giant magneto-impedance effect in nanostructured magnetic ribbons and wires. In: Proceedings of the ninth Asia Pacific physics conference (9th APPC), Hanoi October 25–31, 2004, Vietnam. p. 35–7.

[116] Hashimoto K. In: Steeb S, Warlimont H, editors. Rapidly quenched metals. Proceedings of the fifth International Conference. North-Holland: North-Holland; 1985. p. 1449–56.

[117] Kawashima A, Asami K, Sato T, Hashimoto K. In: Steeb S, Warlimont H, editors. Rapidly quenched metals. Proceedings of the fifth International Conference. North-Holland: North-Holland; 1985. p. 1671–4.

[118] Pardo A, Otero E, Merino MC, Lopez MD, Vazquez M, Agudo P. The influence of Cr addition on the corrosion resistance of $Fe_{73.5}Si_{13.5}Nb_3Cu_1$ metallic glass in SO_2 contaminated environments. Corros Sci 2001;43:689–705.

[119] Choi HW, Kim HK, Kim J, Han SH, Kim HJ. The effect of Cr addition on structure and corrosion resistance in FeTiN nanocrystalline soft magnetic thin films. IEEE Trans Magn 2001;37:1773–5.

[120] Vazquez M, Zhukov A, Aragoneses P, Aras J, Garcia JM, Marin P, et al. Magneto-impedance in glass-coated CoMnSiB amorphous microwires. IEEE Trans Magn 1998;34:724–8.

[121] Valenzuela R, Knobel M, Vazquez M, Hernando A. An alternative approach to giant magnetoimpedance phenomena in amorphous ferromagnetic wires. J Appl Phys 1995;78:5189–91.

[122] Freijo JJ, Hernando A, Vazquez M, Mendez A, Ramanan VR. Exchange biasing in ferromagnetic amorphous wires: A controllable micromagnetic configuration. Appl Phys Lett 1999;74:1305–7.

[123] Aragoneses P, Zhukov A, Gonzalez J, Blanco JM, Dominguez L. Effect of AC driving current on magneto-impedance effect. Sens Acta A 2000;81:86–90.

[124] Chen AP, Britel MR, Zhukova V, Zhukov A, Dominguez L, Chizhik AB, et al. Influence of AC magnetic field amplitude on the surface magnetoimpedance tensor in amorphous wire with helical magnetic anisotropy. IEEE Trans Magn 2004;40:3368–77.

[125] Mandal K, Pan Mandal S, Vazquez M, Puerta S, Hernando A. Giant magnetoimpedance effect in a positive-magnetostrictive glass-coated amorphous microwire. Phys Rev B 2002;65:064402:1–2:6.

[126] Guo HQ, Kronmüller H, Dragon T, Chen C, Shen BG. Transverse domain structure related giant magnetoimpedance in nanocrystalline $Fe_{73.5}Cu_1Nb_3Si_{13.5}B_9$ ribbons. J Appl Phys 1998;84:5673–6.

[127] Qin W, Xu F, Peng K, Gao W, Du Y. Effect of the slight surface oxidation of ribbons on the dynamic magnetization of nanocrystalline soft magnetic ribbons. J Non-cryst Solid 2003;316:398–402.

[128] Lachowicz HK, Garcia KL, Kuzminski M, Zhukov A, Vazquez M. Skin-effect and circumferential permeability in micro-wires utilized in GMI-sensors. Sens Acta A 2005;119:384–9.

[129] Pirota KR, Kraus L, Chiriac H, Knobel M. Magnetic properties and giant magnetoimpedance in a CoFeSiB glass-covered microwire. J Magn Magn Mater 2000;221:L243–7.

[130] Moron C, Garcia A. Giant magneto-impedance in nanocrystalline glass-covered microwires. J Magn Magn Mater 2005;290–291:1085–8.

[131] Makhanovskiy DP, Panina LV, Mapps DJ. Field-dependent surface impedance tensor in amorphous wires with two types of magnetic anisotropy: Helical and circumferential. Phys Rev B 2001;63:144424: 1–4:17.

[132] Kim CG, Yoon SS, Jang KJ, Kim CO. Validity of the Stoner–Wohlfarth model in hysteretic giant magnetoimpedance of annealed amorphous materials. Appl Phys Lett 2001;78:778–80.

[133] Rao KV, Humphrey FB, Costa-Kramer JL. Very large magneto-impedance in amorphous soft ferromagnetic wires. J Appl Phys 1994;76:6204–8.

[134] Betancourt I, Valenzuela R, Vazquez M. Giant magnetoimpedance in Co-based microwires at low frequencies (100 Hz to 13 MHz). J Appl Phys 2002;91:8423–5.

[135] Raposo V, Garcia D, Zazo M, Flores AG, Iniguez JI. Frequency dependence of the giant magnetoimpedance in current annealed amorphous wires. J Magn Magn Mater 2004;272–276:1463–5.

[136] da Silva RB, de Andrade AMH, Severio AM, Schelp LF, Sommer RL. Giant magnetoimpedance in glass-covered amorphous microwires at microwave frequencies. J Appl Phys 2002;91:7436–8.

[137] de Araujo AEP, Machado FLA, de Aguiar FM, Rezende SM. GMI measurements in ribbons of $Co_{70.4}Fe_{4.6}Si_{15}B_{10}$ in a wide range of frequencies. J Magn Magn Mater 2001;226–230:724–6.

[138] Doyle WD, He X, Tang P, Jagielinski T, Smith N. Frequency dependence of the transverse biased permeability in thin permalloy films. J Appl Phys 1993;73:5995–7.

[139] Chiriac H, Marinescu CS, Ovari TA. Temperature dependence of the magneto-impedance effect. J Magn Magn Mater 1999;196–197:162–3.

[140] Kim YK, Cho WS, Kim TK, Kim CO, Lee HB. Temperature dependence of magnetoimpedance effect in amorphous $Co_{66}Fe_4NiB_{14}Si_{15}$ ribbon. J Appl Phys 1998;83:6575–7.

[141] Dokukin ME, Perov NS, Kim CO. The cryogenic treatment effect on the magneto-impedance properties of the Co- and Fe-based amorphous ribbons. Phys Stat Sol A 2004;201:1988–91.

[142] Phan MH, Peng HX, Wisnom MR, Yu SC, Chau N. Enhanced GMI effect in a $Co_{70}Fe_5Si_{15}B_{10}$ ribbon due to Cu and Nb substitution for B. Phys Stat Sol A 2004;201:1558–62.

[143] Tehranchi MM, Ghanaatshoar M, Mohseni SM, Coisson M, Vazquez M. Temperature dependence of magnetoimpedance in annealed Co-based ribbons. J Non-cryst Solid 2005;351:2983–6.

[144] Chen G, Yang XL, Zeng L, Yang JX, Gong FF, Yang DP, et al. High-temperature giant magnetoimpedance in Fe-based nanocrystalline alloy. J Appl Phys 2000;87:5263–5.

[145] Marin P, Vazquez M, Arcas J, Hernando A. Thermal dependence of magnetic properties in nanocrystalline FeSiBCuNb wires and microwires. J Magn Magn Mater 1999;203:6–11.

[146] Chiriac H, Ovari TA, Marinescu CS. Comparative study of the giant magneto-impedance effect in CoFeSiB glass-covered and cold-drawn amorphous wires. IEEE Trans Magn 1997;33:3352–4.

[147] Nie HB, Zhang XX, Pakhomov AB, Xie Z, Yan X, Zhukov A, et al. Giant magnetoimpedance of glass-covered amorphous microwires of Co–Mn–Si–B and Co–Si–B. J Appl Phys 1999;85:4445–7.

[148] Zhukova V, Larin VS, Zhukov A. Stress induced magnetic anisotropy and giant magnetoimpedance in Fe-rich glass-coated magnetic microwires. J Appl Phys 2003;94:1115–8.

[149] Phan MH, Peng HX, Wisnom MR, Yu SC. Giant magneto-impedance effect in a Co-based amorphous microwire for quick-response magnetic sensor applications. In: Proceedings of ESDA04 seventh biennial conference on engineering systems design and analysis, July 19–22, 2004, Manchester, UK. p. 1–5.

[150] Antonenco A, Manov V, Shepelev L, Sorkine E, Tarakanov J. Annealing induced evolution of structure and high frequency magnetic properties in nanocrystalline glass-coated microwires. Mater Sci Eng A 2001;304–306:975–8.

[151] Vazquez M, Garcia-Beneytez JM, Garcia JM, Sinnecker JP, Zhukov AP. Giant magneto-impedance in heterogeneous microwires. J Appl Phys 2000;88:6501–5.

[152] Zhukova V, Usov NA, Zhukov A, Gonzalez J. Length effect in a Co-rich amorphous wire. Phys Rev B 2002;65:134407:1–7:7.

[153] Vazquez V, Zhukov AP, Garcia KL, Pirota KR, Ruiz A, Martinez JL, et al. Temperature dependence of magnetization reversal in magnetostrictive glass-coated amorphous microwires. Mater Sci Eng A 2004;375–377:1145–8.

[154] Vazquez V, Li YF, Chen DX. Influence of the sample length and profile of the magnetoimpedance effect in FeCrSiBCuNb ultrasoft magnetic wires. J Appl Phys 2002;91:6539–44.

[155] Ruiz J, Atienza JM, Elices M. Residual stresses in wires: influence of wire length. J Mater Eng Perform 2003;12:480–9.

[156] Phan MH, Peng HX, Wisnom MR, Yu SC. Large enhancement of GMI effect in polymer composites containing Co-based ferromagnetic microwires. J Magn Magn Mater 2007;316:e253–6.

[157] Panina LV, Mohri K, Bushida K, Noda M. Giant magneto-impedance and magneto-inductive effects in amorphous alloys. J Appl Phys 1994;76:6198–203.

[158] Hu J, Qin H, Zhang F, Zheng RK. Diameter dependence of the giant magnetoimpedance in hard-drawn CoFeSiB amorphous wires. J Appl Phys 2002;91:7418–20.

[159] Sommer RL, Gundel A, Chien CL. Magneto-impedance effects in multilayered permalloy materials. J Appl Phys 1999;86:1057–61.

[160] Amalou F, Gijs MAM. Giant magnetoimpedance of chemically thinned and polished magnetic amorphous ribbons. J Appl Phys 2001;90:3466–70.

[161] Amalou F, Gijs MAM. Giant magnetoimpedance in trilayer structures of patterned magnetic amorphous ribbons. Appl Phys Lett 2002;81:1654–6.

[162] Amalou F, Gijs MAM. Giant magnetoimpedance of amorphous ribbon/Cu/amorphous ribbon trilayer microstructures. J Appl Phys 2004;95:1364–71.

[163] Le AT, Kim CO, Chau N, Cuong ND, Tho ND, Hoa NQ, et al. Soft magnetic properties and giant magneto-impedance effect of $Fe_{73.5-x}Cr_xSi_{13.5}B_9Nb_3Au_1$ ($x = 1$–5) alloys. J Magn Magn Mater 2006;307:178–85.

[164] Pirota KR, Kraus L, Knobel M, Pagliuso PG, Rettori C. Angular dependence of giant magnetoimpedance in an amorphous Co–Fe–Si–B ribbon. Phys Rev B 1999;60:6685–91.

[165] Kurlyandskaya GV, Barandianran JM, Vazquez M, Garcia D, Dmitrieva NV. Influence of geometrical parameters on the giant magnetoimpedance response in amorphous ribbons. J Magn Magn Mater 2000;215–216:740–2.

[166] Sommer RL, Chien CL. Role of magnetic anisotropy in the magnetoimpedance effect in amorphous alloys. Appl Phys Lett 1995;67:857–9.

[167] Chen C, Luan KZ, Liu YH, Mei LM, Guo HQ, Shen BG, et al. Giant magnetoimpedance effects in the soft ferromagnet $Fe_{73.5}CuNb_3Si_{13.5}B_9$. Phys Rev B 1996;54:6092–4.

[168] Knobel M, Chiriac H, Sinecker JP, Marinescu S, Ovari TA, Inoue A. Comparative study of the giant magneto-impedance effect in Fe-based nanocrystalline ribbons. Sens Acta A 1997;59:256–60.

[169] Lee HB, Kim YK, Kim TK, Song YH, Yu SC. Magnetoimpedance effect in nanocrystalline $Fe_{90-x}B_xZr_7Cu_1Al_2$ ($x = 2,4,6,8$) alloys. J Appl Phys 1999;85:5429–31.

[170] Lee HB, Kim KJ, Kim TK, Kim CO, Yu SC. Magnetoimpedance effect in the nanocrystalline Fe–Zr–Cu–B–Al alloy system. J Appl Phys 2000;87:5269–91.

[171] He J, Guo HQ, Shen BG, He KY, Zhang HW. Influence of annealing on the magnetic properties and magneto-impedance response in $Fe_{84}Zr_7B_8Cu_1$ ribbons. Mater Sci Eng A 2001;304–306:988–91.

[172] Lee HB, Kim KJ, Kim YK, Kim KS, Yu SC. Ultra-soft magnetic properties in nanocrystalline $Fe_{81}B_{11}Nb_7Cu_1$ alloy. J Alloy Compd 2001;326:313–6.

[173] Phan MH, Kim YS, Chien NX, Yu SC, Lee HB, Chau N. Giant magnetoimpedance effect in amorphous $Co_{70}Fe_5Si_{15}B_{10}$ and $Co_{70}Fe_5Si_{15}Nb_{2.2}Cu_{0.8}B_7$ ribbons. Jpn J Appl Phys 2003;42:5571–4.

[174] Machado LA, da Silva BL, Rezende SM, Martins CS. Giant ac magnetoresistance in the soft ferromagnet $Co_{70.4}Fe_{4.6}Si_{15}B_{10}$. J Appl Phys 1994;75:6563–5.

[175] Ku W, Ge F, Zhu J. Effect of magnetic field annealing on the giant magnetoimpedance in FeCuMoSiB ribbons. J Appl Phys 1997;82:5050–3.

[176] Kraus L, Knobel M, Kane SN, Chiriac H. Influence of joule heating on magnetostriction and giant magnetoimpedance effect in a glass covered CoFeSiB microwire. J Appl Phys 1999;85:5435–7.

[177] Kraus L, Chiriac H, Ovari TA. Magnetic properties of stress-joule-heated amorphous FeCrBSi microwire. J Magn Magn Mater 2000;215–216:343–5.

[178] Pirota KR, Kraus L, Chiriac H, Knobel M. Magnetostriction and GMI in Joule-heated CoFeSiB glass-covered microwires. J Magn Magn Mater 2001;226–230:730–2.

[179] Brunetti L, Tiberto P, Vinai F, Chiriac H. High-frequency giant magnetoimpedance in joule-heated Co-based amorphous ribbons and wires. Mater Sci Eng A 2001;304–306:961–4.

[180] Li DR, Lu ZC, Zhou SX. Magnetic anisotropy and stress-impedance effect in Joule heated $Fe_{73.5}Cu_1Nb_3Si_{13.5}B_9$ ribbons. J Appl Phys 2004;95:204–7.

[181] Lee HB, Kim YK, Kim KJ, Kim TK. A novel annealing technique for the magneto-impedance effect in amorphous $Co_{66}Fe_4Ni_1B_{14}Si_{15}$ alloy. J Magn Magn Mater 2000;215–216:310–2.

[182] Hernando B, Sanchez ML, Prida VM, Tejedor M, Vazquez M. Magnetoimpedance effect in amorphous and nanocrystalline ribbons. J Appl Phys 2001;90:4783–90.

[183] Kurlyandskaya GV, Vazquez M, Munoz JL, Garcia D, McCord J. Effect of induced magnetic anisotropy and domain structure features on magneto-impedance in stress annealed Co-rich amorphous ribbons. J Magn Magn Mater 1999;196–197:259–61.

[184] Tejedor M, Hernando B, Sanchez ML, Prida VM, Vazquez M. Stress and magnetic field dependence of magneto-impedance in amorphous $Co_{66.3}Fe_{3.7}Si_{12}B_{18}$ ribbons. J Magn Magn Mater 1999;196–197:330–2.

[185] Wang ZC, Gong FF, Yang XL, Zeng L, Chen G, Yang JX, et al. Longitudinally driven giant magnetoimpedance effect in stress-annealed Fe-based nanocrystalline ribbons. J Appl Phys 2000;87:4819–21.

[186] Li YF, Vazquez M, Chen DX. Giant magnetoimpedance effect and magnetoelastic properties in stress-annealed FeCuNbSiB nanocrystalline wire. IEEE Trans Magn 2002;38:3096–8.

[187] Kraus L, Malatek M, Postava K, Janickovic D. Asymmetric giant magnetoimpedance in stress-field annealed CoFeBSi amorphous ribbons. J Magn Magn Mater 2005;290-291:1131–3.

[188] Blanco JM, Zhukov A, Gonzalez J. Asymmetric torsion stress giant magnetoimpedance in nearly zero magnetostrictive amorphous wires. J Appl Phys 2000;87:4813–5.

[189] Gonzalez J, Chen AP, Blanco JM, Zhukov A. Effect of applied mechanical stressses on the impedance response in amorphous microwires with vanishing magnetostriction. Phys Stat Sol A 2002; 189:599–608.

[190] Cobeno AF, Zhukov A, Blanco JM, Larin V, Gonzalez J. Magnetoelastic sensor based on GMI of amorphous microwire. Sens Acta A 2001;91:95–8.

[191] Ahn SJ, Kim CG, Park CG, Yu SC. Laser annealing effect of giant magneto-impedance in amorphous $Co_{66}Fe_4Nib_{14}Si_{15}$ ribbon. Mater Sci Eng A 2001;304–306:1026–9.

[192] Ahn SJ, Lee BS, Kim CG, Rheem YW, Yoon SS, Kim CO. Giant magnetoimpedance in Co-based microwire annealed by pulsed Nd:YAG laser. Sens Acta A 2003;106:221–4.

[193] Roozmeh SE, Tehranchi MM, Ghanatshoar M, Mohseni SM, Parhizkari M, Ghomi H, et al. Magnetoimpedance effect in laser annealed $Co_{68.25}Fe_{4.5}Si_{12.25}B_{15}$ amorphous ribbons. J Magn Magn Mater 2006;304:e633–5.

[194] Li YF, Vazquez M, Chen DX. Torsion-dependent magnetoimpedance in FeCuNbSiB nanocrystalline wires with vanishing or transverse anisotropy. J Appl Phys 2003;93:9839–41.

[195] Coisson M, Tiberto P, Vinai F, Kane SN. Influence of stress-annealing on magneto-transport properties in Co-based amorphous ribbons. Sens Acta A 2003;106:199–202.

[196] Ohnuma M, Hono K, Yanai T, Nakano M, Fukunaga H, Yoshizawa Y. Origin of the magnetic anisotropy induced by stress annealing in Fe-based nanocrystalline alloy. Appl Phys Lett 2005;86: 152513–5.

[197] Phan MH, Peng HX, Wisnom MR, Yu SC, Kim CG, Vazquez M. Neutron irradiation effect on permeability and magnetoimpedance of amorphous and nanocrystalline magnetic materials. Phys Rev B 2005;71:134423:1–3:5.

[198] Kim YS, Phan MH, Yu SC, Kim KS, Lee HB, Kim BG, et al. Annealing and neutron irradiation effects on the permeability in $Fe_{86}Zr_7B_6Cu_1$ alloy. Physica B 2003;327:311–4.

[199] Cayssol F, Menendez JL, Ravelosona D, Chappert C, Jamet JP, Ferre J, et al. Enhancing domain wall motion in magnetic wires by ion irradiation. Appl Phys Lett 2005;86:022503:1–3:3.

[200] Atalay F, Atalay S. Giant magnetoimpedance effect in NiFe/Cu plated wire with various plating thicknesses. J Alloy Compd 2005;392:322–8.

[201] Atalay F, Kaya H, Atalay S. Effect pf pH on the magnetoimpedance properties of electrodeposited CoNiFe microtubes. Physica B 2006;371:327–31.

[202] Costa-Kramer JL, Rao KV. Influence of magnetostriction on magneto-impedance in amorphous soft ferromagnetic wires. IEEE Trans Magn 1995;31:1261–5.

[203] Barandianran JM, Hernando A. Magnetostriction influence on the giant magnetoimpedance effect: A key parameter. J Magn Magn Mater 2004;268:309–14.

[204] Garcia D, Raposo V, Montero O, Iniguez JI. Influence of magnetostriction constant on magnetoimpedance-frequency dependence. Sens Acta A 2006;129:227–30.

[205] Makhotkin VE, Shurukhin BP, Lopatin VA, Marchukov YP, Levin YK. Magnetic field sensors based on amorphous ribbons. Sens Acta A 1991;25–27:759–62.

[206] Sartorelli ML, Knobel M, Schoenmaker J, Gutierrez J, Barandiarán JM. Giant magneto-impedance and its relaxation in Co–Fe–Si–B amorphous ribbons. Appl Phys Lett 1997;71:2208–10.

[207] Knobel M, Sartorelli ML, Schoenmaker J. Magnetoimpedance aftereffect in a soft magnetic amorphous wire. Phys Rev B 1997;55:3362–5.

[208] Sartorelli ML, Knobel M, Sinnecker JP. Magneto-impedance relaxation in amorphous wires and ribbons. J Magn Magn Mater 1998;177–181:121–2.

[209] Raposo V, Flores AG, Zazo M, Iniguez JI. Magnetic aftereffect of giant magnetoimpedance in amorphous wires. J Magn Magn Mater 2003;254–255:204–6.

[210] Raposo V, Montero O, Flores AG, Zazo M, Iniguez JI. Magnetic aftereffect of the giant magnetoimpedance in Cobalt-based amorphous wires. J Magn Magn Mater 2004;272–276:1844–5.

[211] Lee HB, Kim YS, Yu SC. Supergiant magnetoimpedance effect of a LC-resonator using a glass-coated amorphous microwire. J Magn 2002;7:160–4.

[212] Paposo V, Vazquez M, Flores AG, Zazo M, Iniguez JI. Giant magnetoimpedance effect enhancement by circuit matching. Sens Acta A 2003;106:329–32.

[213] Kim YS, Yu SC, Le AT, Kim CO, Rhee JR, Vazquez M, et al. Supergiant magnetoimpedance effect in a glass-coated microwire LC resonator. J Appl Phys 2006;99:08C510:1–0:3.

[214] Le AT, Kim CO, Phan MH, Lee HB, Yu SC. Very large magnetoimpedance effect in a glass-coated microwire LC-resonator. Physica B 2007;395:88–92.

[215] Le AT, Phan MH, Kim CO, Vazquez M, Lee HB, Hoa NQ, et al. Influences of annealing and wire geometry on the giant magnetoimpedance effect in a glass-coated microwire LC-resonator. J Phys D Appl Phys 2007;40:4582–5.

[216] Kim YS, Yu SC, Lu H, Lee JB, Lee HB. A class of micromachined magnetic resonator for high-frequency magnetic sensor applications. J Appl Phys 2006;99:08B309:1–9:3.

[217] Kim YS, Yu SC, Lee JB, Lee HB. A new class of LC-resonator for micro-magnetic sensor application. J Magn Magn Mater 2006;304:117–21.

[218] Kim SD, Shin KH, Kim JW, Hak Y, Lim SH, Gong GS. Magnetic field sensitivity of LC filter-type magnetoimpedance sensors. J Magn Magn Mater 2006;304:e391–3.

[219] Chen DX, Pascual L, Hernando A. Comment on analysis of asymmetric giant magnetoimpedance in field-annealed Co-based amorphous ribbon. Appl Phys Lett 1999;75:2114;
Chen DX, Pascual L, Hernando A. Comment on analysis of asymmetric giant magnetoimpedance in field-annealed Co-based amorphous ribbon. Appl Phys Lett 2000;77:1727–9.

[220] Tejedor M, Hernando B, Sanchez ML, Prida VM, Kurlyandskaya GV, Garcia D, et al. Frequency dependence of hysteretic magneto-impedance in CoFeMoSiB amorphous ribbons. J Magn Magn Mater 2000;215–216:425–7.

[221] Kim CG, Jang KJ, Kim DY, Yoon SS. Response to comment on 'analysis of asymmetric giant magnetoimpedance in field-annealed Co-based amorphous ribbon. Appl Phys Lett 2000;77:1727;
Kim CG, Jang KJ, Kim DY, Yoon SS. Response to comment on 'analysis of asymmetric giant magnetoimpedance in field-annealed Co-based amorphous ribbon. Appl Phys Lett 2000;77:1731.

[222] Makhnovskiy DP, Panina LV, Mapps DJ. Surface impedance tensor in amorphous wires with helical anisotropy: magnetic hysteresis and asymmetry. J Appl Phys 2001;89:7224–6.

[223] Rheem YW, Kim CG, Kim CO, Yoon SS. Current sensor application of asymmetric giant magnetoimpedance in amorphous materials. Sens Acta A 2003;106:19–21.

[224] Kitoh T, Mohri K, Uchiyama T. Asymmetrical magneto-impedance effect in twisted amorphous wires for sensitive magnetic sensors. IEEE Trans Magn 1995;31:3137–9.

[225] Machado FLA, Rodrigues AR, Puça AA, de Araújo AEP. Highly asymmetric giant magnetoimpedance. Forum Mater Sci Forum, TransTech Public 1999;302–303:202–10.

[226] Song SH, Kim KS, Yu SC, Kim CG, Vazquez M. Asymmetric GMI characteristics in current-biased amorphous $(Co_{0.94}Fe_{0.06})_{72.5}Si_{12.5}B_{15}$ wire. J Magn Magn Mater 2000;215–216:532–4.

[227] Song SH, Yu SC, Kim CG, Kim HC, Kim WY. Asymmetric giant magnetoimpedance in annealed amorphous $(Co_{0.94}Fe_{0.06})_{72.5}Si_{12.5}B_{15}$ wire under the circumferential field. J Appl Phys 2000;87: 5266–8.

[228] Byon KS, Yu SC, Kim CG, Yoon SS. Asymmetric characteristics of magnetoimpedance in amorphous $Fe_{77.5}Si_{7.5}B_{15}$ wire. J Magn Magn Mater 2001;226–230:718–20.

[229] Gomez-Polo C, Vazquez M, Knobel M. Rotational giant magnetoimpedance in soft magnetic wires: modelization through Fourier harmonic contribution. Appl Phys Lett 2001;78:246–8.

[230] Panina LV, Mohri K, Makhnovskiy DP. Mechanism of asymmetrical magnetoimpedance in amorphous wires. J Appl Phys 1999;85:5444–6.

[231] Phan MH, Yu SC, Kim CG, Vazquez M. Origin of asymmetrical magnetoimpedance in a Co-based amorphous microwire due to dc bias current. Appl Phys Lett 2003;83:2871–3.

[232] Gunji T, Panina LV, Mohri K. J Magn Soc Jpn 1997;21:793–8.

[233] Makhnovskiy DP, Panina LV, Mapps DJ. Asymmetrical magnetoimpedance in as-cast CoFeSiB amorphous wires due to ac bias. Appl Phys Lett 2000;77:121–3.

[234] Kim CG, Jang KJ, Kim HC, Yoon SS. Asymmetric giant magnetoimpedance in field-annealed Co-based amorphous ribbon. J Appl Phys 1999;85:5447–9.

[235] Kim KJ, Kim CG, Yoon SS, Yu SC. Effect of annealing field on asymmetric giant magnetoimpedance profile in Co-based amorphous ribbon. J Magn Magn Mater 2000;215–216:488–91.

[236] Kim CG, Rheem YW, Kim CO, Yoon SS, Ganshina EA, Kochneva MY, et al. High-temperature dependence of asymmetric giant magnetoimpedance and magnetostatic properties in Co-based amorphous ribbon. J Magn Magn Mater 2003;258–259:170–3.

[237] Park DG, Moon EJ, Rheem YW, Kim CG, Hong JH. The GMI profiles of surface-removed amorphous ribbon. Physica B 2003;327:357–9.

[238] Buznikov NA, Kim CG, Kim CO, Yoon SS. A model for asymmetric giant magnetoimpedance in field-annealed amorphous ribbons. Appl Phys Lett 2004;85:3507–9.

[239] Buznikov NA, Kim CG, Kim CO, Yoon SS. Modeling of asymmetric giant magnetoimpedance in amorphous ribbons with a surface crystalline layer. J Magn Magn Mater 2005;388:130–6.

[240] Phan MH, Peng HX, Yu SC, Chau N. Valve behavior of giant magnetoimpedance in field-annealed $Co_{70}Fe_5Si_{15}Nb_{2.2}Cu_{0.8}B_7$ amorphous ribbon. J Appl Phys 2005;97:10M108:1–8:3.

[241] Ha ND, Thanh NT, Kim HB, Kim CG, Kim CO, Shina EG, et al. Near-surface magnetic properties of CoFeAlO thin films. Solid State Commun 2005;135:721–4.

[242] Vazquez M, Knobel M, Sanchez ML, Valenzuela R, Zhukov AP. Giant magneto-impedance effect in soft magnetic wires for sensor applications. Sens Acta A 1997;59:20–9.

[243] Vinai F, Coisson M, Tiberto P. High-frequency magneto-impedance in metastable metallic materials: an overview. J Magn Magn Mater 2006;300:e82–7.

[244] Takemura Y, Tokuda H. IEEE Trans Magn 1996;32:4947–9.

[245] Li YF, Vaquez M, Chen DX. GMI effect of $Fe_{73.5-x}Cr_xCu_1Nb_3Si_{13.5}B_9$ amorphous and nanocrystalline soft wires. J Magn Magn Mater 2002;249:342–5.

[246] Usov N, Antonov A, Granovsky A. Theory of giant magntoimpedance effect in composite amorphous wire. J Magn Magn Mater 1997;171:64–8.

[247] Phan MH, Peng HX, Wisnom MR, Tung MT, Dung NV, Nghi NH. Optimized GMI effect in electrodeposited CoP/Cu composite wires. J Magn Magn Mater 2007;316:244–7.

[248] Kurlyandskays GV, Garcia-Arribas A, Barandiaran JM. Advantages of nonlinear giant magnetoimpedance for sensor applications. Sens Acta A 2003;106:234–9.

[249] Li XP, Seet HL, Fran J, Yi JB. Electrodeposition and characteristics of $Ni_{80}Fe_{20}$/Cu composite wires. J Magn Magn Mater 2006;304:111–6.

[250] Buznikov NA, Antonov AS, Granovsky AB, Kim CG, Kim CO, Li XP, et al. Giant magnetoimpedance in composite wires with insulator layer between non-magnetic core and soft magnetic shell. J Magn Magn Mater 2006;300:e63–6.

[251] Hu J, Zhou SX, Zhang LH, Wang HX. Giant magnetoimpedance in the amorphous ribbon $Fe_{8.0}Co_{62.4}Mn_{0.5}Mo_{0.6}Ni_{0.5}Si_{14.7}B_{13.3}$. Mater Sci Eng B 1999;68:63–6.

[252] Byon KS, Yu SC, Kim CG. Permeability and giant magnetoimpedance in $Co_{69}Fe_{4.5}X_{1.5}Si_{10}B_{15}$ ($X = Cr$, Mn, Ni) amorphous ribbons. J Appl Phys 2001;89:7218–20.

[253] Goncalves LAP, Soares JM, Machado FLA, de Azevedo WM. GMI effect in the low magnetostrictive $Co_{70}Fe_5Si_{15}B_{10}$ alloys. Physica B 2006;384:152–4.

[254] Phan MH, Peng HX, Yu SC, Vazquez M. Optimized giant magnetoimpedance effect in amorphous and nanocrystalline materials. J Appl Phys 2006;99:08C505:1–5:3.

[255] Tejedor M, Hernando B, Sanchez ML, Prida VM, Gorria P. Magnetic domains and magnetoimpedance effect during the nanocrystalization of $Fe_{73.5}Cu_1Nb_3Si_{16.5}B_6$ ribbons. J Non-cryst Solid 2001;287:396–400.

[256] Franco V, Conde A. Magnetic anisotropy distribution and giant magnetoimpedance in $Fe_{73.5}Si_xB_{22.5-x}$-Cu_1Nb_3 ($x = 9$, 16) alloys. Mater Lett 2001;49:256–61.

[257] Hu J, Jiang MH, Qin HW, Li B, Kronmuler H. Magnetic properties of as-quenched Fe–Cu–Mo–Si–B nanocrystalline ribbons. Mater Sci Eng A 2007;449–451:371–4.

[258] Hu J, Qin HW, Zhou SX, Wang YH, Wang ZX. Giant magnetoimpedance effect in $Fe_{79.5}P_{12}C_6Mo_{0.5}$-$Cu_{0.5}Si_{1.5}$ nanocrystalline ribbons. Mater Sci Eng B 2001;83:24–8.

[259] Tho ND, Chau N, Yu SC, Lee HB, The ND, Tuan LA. Annealing effect on soft magnetic properties and magnetoimpedance of finemet $Fe_{73.5}Si_{13.5}B_9Nb_3Au_1$ alloy. J Magn Magn Mater 2006;304:e195–7.

[260] Phan MH, Peng HX, Tho ND, Chau N, Yu SC. Enhanced GMI effect in $Fe_{73.5-x}Mn_xSi_{13.5}B_9Nb_3Cu_1$ ($x = 1$, 3, 5) nanocomposites due to Mn substitution for Fe. Proc SPIE Int Soc Opt Eng 2006;6170:61700Q:1–Q:8.

[261] Tho ND, Chau N, Yu SC, Lee HB, Tuan LA, Hoa NQ. Soft magnetic behavior in amorphous and nanocrystalline $Fe_{73.5-x}Mn_xSi_{13.5}B_9Nb_3Cu_1$ ($x = 1$, 3, 5) alloys. J Magn Magn Mater 2006;304:e868–70.

[262] Tho ND, Chau N, Yu SC, Lee HB, The ND, Hoa NQ. A systematic study of giant magnetoimpedance of Cr-substituted $Fe_{73.5-x}Cr_xSi_{13.5}B_9Nb_3Au_1$ ($x = 1$, 2, 3, 4, 5) alloys. J Magn Magn Mater 2006;304:e871–3.

[263] Shahri F, Beitollahi A, Shabestari SG, Ghanaatshoar M, Tehranchi MM. Structural characterization and magnetoimpedance effect in amorphous and nanocrystalline AlGe-substituted FeSiBNbCu ribbons. J Magn Magn Mater 2007;312:35–42.

[264] Knobel M, Schoenmaker J, Sinnecker JP, Turtelli RS, Grossinger R, Hofstetter W, et al. Giant magnetoimpedance in nanocrystalline $Fe_{73.5}Cu_1Nb_3Si_{13.5}B_9$ and $Fe_{86}Zr_7B_6Cu_1$ ribbons. Mater Eng A 1997;226–228:546–9.

[265] Chiriac H, Ovari TO, Marinescu CS. Giant magnetoimpedance effect in nanocrystalline ribbons. Nanostruc Mater 1999;12:775–8.

[266] Lee HB, Kim YK, Kim TK, Kim TK, Yu SC. Magnetoimpedance effect in nanocrystalline $Fe_{91-x}Zr_7B_xCu_1Al_1$ ($x = 2$, 4, 6, 8) alloys. J Magn Magn Mater 2000;215–216:307–9.

[267] Hernando B, Alvarez P, Santos JD, Gorria P, Sanchez ML, Olivera J, et al. Magnetoimpedance effect in Nanoperm alloys. J Magn Magn Mater 2006;300:e59–62.

[268] Hu J, Li B, Qi HW, Jiang MH. Giant magnetoimpedance in nanocrystalline $Fe_{90.3-x}Zr_7B_{2.7}Cu_x$ $(0.5 < x < 1.5)$ as-spun ribbons. Mater Letter 2005;59:3069–72.

[269] Zhang K, Lv Z, Yao B, Wang D. Boron content dependence of magnetoimpedance in $Fe_{91-x}Zr_5B_xNb_4$ alloys. J Non-cryst Solid 2006;352:78–83.

[270] Kim KS, Yu SC, Lee HB, Kim YK. Magnetization behavior and magnetoimpedance effect in melt-spun $Fe_{75-x}Co_xZr_8Nb_2B_{15}$ $(x = 5, 10, 15)$ alloys. J Magn Magn Mater 2002;239:560–3.

[271] Hu J, Zhou SX, Chen W, Wang Y. Giant magnetoimpedance effect in Fe–Nb–B. Solid State Commun 1999;109:661–4.

[272] Qin H, Hu J, Chen J, Jiang M. Giant magnetoimpedance and permeability in nanocrystalline Fe–Nb–B ribbons. Mater Sci Eng A 2007;449–451:456–9.

[273] Hu J, Qin H, Chen J. Magnetoimpedance effect in $Nd_3Fe_{77}B_{20}$ amorphous ribbon. J Magn Magn Mater 2002;251:38–41.

[274] Sommer RL, Chien CL. Longitudinal and transverse magneto-impedance in amorphous $Fe_{73.5}Cu_1Nb_3$-$Si_{13.5}B_9$ films. Appl Phys Lett 1995;67:3346–8.

[275] Xiao SQ, Liu YH, Yan SS, Dai YY, Zhang L, Mei LM. Giant magnetoimpedance and domain structure in FeCuNbSiB films and sandwiched films. Phys Rev B 2000;61:5734–9.

[276] Viegas ADC, de Andrade AMH, Sommer RL, Jiang JS, Chien CL. Magnetoimpedance in $Fe_{73.5}Cu_1Nb_3$-$Si_{13.5}B_9$ amorphous films at microwave frequencies. J Magn Magn Mater 2001;226–230:707–8.

[277] Wang WJ, Xiao SQ, Jiang S, Yuan HM, Wu ZY, Ji G, et al. Influence of magnetic induced anisotropy on giant magnetoimpedance effects in FeCuNbSiB films. Thin Solid Films 2005;484:299–302.

[278] da Siva RB, Viegas ADC, Correa MA, de Andrade AMH, Sommer RL. Complex high-frequency magnetization dynamics and magnetoimpedance in thin films. Physica B 2006;384:172–4.

[279] Garcia D, Munoz JI, Kurlyandskaya G, Vazquez M, Ali M, Gibbs MRJ. Induced anisotropy, magnetic domain structure and magnetoimpedance effect in CoFeB amorphous thin films. J Magn Magn Mater 1999;191:339–44.

[280] Nakai T, Abe H, Yabukami S, Arai KI. Impedance property of thin film GMI sensor with controlled inclined angle of stripe magnetic domain. J Magn Magn Mater 2005;290–291:1355–8.

[281] Correa MA, Viegas ADC, da Silva RB, de Andrade AMH, Sommer RL. Magnetoimpedance in amorphous/metal/amorphous sandwiched films at GHz frequencies. Physica B 2006;384:155–7.

[282] Makhnovskiy DP, Fry N, Panina LV, Mapps J. Effect of induced anisotropy on magnetoimpedance characteristics in NiFe/Au/NiFe sandwich thin films. J Appl Phys 2004;96:2150–8.

[283] Makhnovskiy DP, Panina LV, Fry N, Mapps J. Magnetoimpedance in NiFe/Au/NiFe sandwich films with different types of anisotropy. J Magn Magn Mater 2004;272–276:1866–7.

[284] Makhnovskiy DP, Panina LV, Mapps DJ. Asymmetrical magneto-impedance in a sandwich film with a transverse anisotropy using an AC bias. J Magn Magn Mater 2000;215–216:629–33.

[285] Delooze P, Panina LV, Mapps DJ, Ueno K, Sano H. CoFeB–Cu layered film with crossed anisotropy for asymmetrical magnetoimpedance. IEEE Trans Magn 2003;39:3307–9.

[286] Morikawa T, Nishibe Y, Yamadera H, Nonomura Y, Takeuchi M, Sakata J, et al. Enhancement of giant magneto-impedance in layered film by insulator separation. IEEE Trans Magn 1996;32:4965–7.

[287] Morikawa T, Nishibe Y, Yamadera H. Giant magnetoimpedance effect in layered thin films. IEEE Trans Magn 1997;33:4367–72.

[288] Nishibe Y, Yamadera H, Ohta N, Tsukada K, Nonomura Y. Thin film magnetic field sensors utilizing magnetoimpedance effect. Sens Acta A 2000;82:155–60.

[289] Mao XH, Zhou Y, Chen JA, Yu JQ, Cai BC. Giant magnetoimpedance and stress-impedance effects in multilayered FeSiB/Cu/FeSiB films with a meander structure. J Mater Res 2003;18:868–71.

[290] de Andrade AMH, da Silva RB, Correa MA, Viegas ADC, Severino AM, Sommer RL. Magnetoimpedance of NiFe/Ag multilayers in the 100 kHz to 1.8 GHz range. J Magn Magn Mater 2004;272–276:1846–7.

[291] Kurlyandskaya GV, Elbaile L, Alves F, Ahamada B, Barrue R, Svalov AV, et al. Domain structure and magnetization process of a giant magnetoimpedance geometry FeNi/Cu/FeNi(Cu)FeNi/Cu/FeNi sensitive element. J Phys: Conden Mat 2004;16:6561–8.

[292] de Cos D, Garcia-Arribas A, Barandiaran JM. Ferromagnetic resonance in gigahertz magneto-impedance of multilayer systems. J Magn Magn Mater 2006;304:218–21.

[293] de Cos D, Fry N, Orue I, Panina PV, Garcia-Arribas A, Barandiaran JM. Very large magnetoimpedance (MI) in FeNi/Au multilayer film systems. Sens Acta A 2006;129:256–9.

[294] Li XD, Yuan WZ, Zhao ZJ, Ruan JZ, Yang XL. The GMI effect in nanocrystalline FeCuNbSib multilayered films with a SiO_2 outer layer. J Phys D: Appl Phys 2005;38:1351–4.

[295] Correa MA, Viegas ADC, da Silva RB, de Andrade AMH, Sommer RL. GMI in FeCuNbSiB\Cu multilayers. Physica B 2006;384:162–4.

[296] Schelp LF, Rosa EL, Maurice JL, Petroff F, Vaures A. Tunnel magnetoimpedance in cobalt discontinuous films. J Magn Magn Mater 1999;205:170–6.

[297] Cho WS, Yoon TS, Lee HB, Kim CO. Annealing effect on the longitudinal and transverse incremental permeability in FeSmO thin films. J Magn Magn Mater 2000;215–216:680–3.

[298] Granovsky A, Kozlov A, Nedukh S, Tarapov S. High-frequency spin-dependent tunneling in magnetic nanocomposites: Magnetorefractive effect and magnetoimpedance. J Magn Magn Mater 2005;294:117–21.

[299] Yurasov A, Granovsky A, Tarapov S, Clerc JP. High-frequency magnetoimpedance in nanocomposites. J Magn Magn Mater 2006;300:e52–4.

[300] Tuan LA, Ha ND, Kim CO, Rhee JR, Lee HB. Thickness dependence of the magnetic properties and magnetoimpedance effect in CoFeAl thin films. J Magn Magn Mater 2006;304:e53–5.

[301] Phan MH, Peng HX, Ha ND, Tuan LA, Kim CO, Nhat HN. Tunnel magnetoimpedance effect in Co–Fe–Hf–O nanocomposite films [unpublished].

[302] Tokura Y, editor. Colossal magnetoresistive oxides. Advances in condensed materials science, vol. 2. Gordon and Breach Science Publishers; 2000.

[303] Phan MH, Yu SC. Review of the magnetocaloric effect in manganite materials. J Magn Magn Mater 2007;308:325–40.

[304] Fu CM, Hsu KS, Lin ML, Wen ZH. Giant magnetoimpedance effects in sintered $La_{1-x}Ca_xMnO_3$ oxides. J Magn Magn Mater 2000;209:151–3.

[305] Hu J, Qin HW. Magnetoimpedance effect at various temperatures for manganite $La_{0.7}Ca_{0.3}MnO_{3-\sigma}$. Mater Sci Eng B 2003;100:304–6.

[306] Castro GMB, Rodrigues AR, Machado FLA, de Araujo AEP, Jardim RF, Nigam AK. Magnetoimpedance measurements in bulk samples of $La_{0.7}Ca_{0.3}MnO_3$ and $La_{0.6}Y_{0.1}Ca_{0.3}MnO_3$. J Alloy Compd 2004;369:108–11.

[307] Hu J, Qin HW. Magnetoimpedance effect in $La_{0.7}Sr_{0.3}MnO_3$. J Magn Magn Mater 2001;234:419–22.

[308] Hu J, Qin HW. Giant magnetoimpedance effect in $La_{0.65}Sr_{0.35}MnO_3$ under low dc magnetic fields. Mater Sci Eng B 2001;79:186–9.

[309] Hu J, Qin HW. Magnetoimpedance effect in semiconducting $La_{0.4}Sr_{0.6}MnO_3$. Mater Sci Eng B 2002;88:18–21.

[310] Patanjali PV, Theule P, Zhai Z, Hakim N, Sridhar S, Suryanarayanan R, et al. High-frequency magnetoimpedance of double perovskite $La_{1.2}Sr_{1.8}Mn_2O_7$: secondary transitions at high temperatures. Phys Rev B 1999;60:9268–71.

[311] Hu J, Qin HW, Zhang Y. Giant magnetoimpedance effect in La–Ba–Mn–O oxide. Mater Sci Eng B 2000;77:280–1.

[312] Hu J, Qin HW. Magnetoimpedance effect in $La_{0.67}Ba_{0.33}MnO_3$ under low dc magnetic fields. Solid State Commun 2000;116:159–62.

[313] Hu J, Qin HW, Niu HD, Zhu L, Chen J, Xiao W, et al. Magnetoimpedance effect in manganite $La_{2/3}Ba_{1/3}MnO_3$ at various temperatures. J Magn Magn Mater 2003;261:105–11.

[314] Fu CM, Hsu CY, Chao YC, Kim DS, Matsushita N, Abe M. Tunnel magnetoimpedance effect of the ZnNi-ferrite encapsulated NiFe micropsheres. J Magn Magn Mater 2004;272–276:e1839–41.

[315] Hu J, Qin H, Qi G, Jiang M. Giant magnetoimpedance in a MnZn ferrite. J Magn Magn Mater 2006;302:375–7.

[316] Carara M, Sommer RL. Giant magnetoimpedance in highly textured (110)[001] $FeSi_{3\%}$. J Appl Phys 1997;81:4107–9.

[317] Gomez-Polo C, Perez-Landazabal JI, Recarte V, Ciurzynska W. Effect of the ordering on the magnetic and magnetoimpedance properties of Fe-6.5% Si alloy. J Magn Magn Mater 2003;254–255:88–90.

[318] Jantaratana P, Sirisathitkul C. Giant magnetoimpedance in silicon steels. J Magn Magn Mater 2004;281:399–404.

[319] Hu J, Qin H. Magnetoimpedance effect in Fe flakes. J Magn Magn Mater 2002;246:375–8.

[320] Soares JM, de Araujo JH, Cabral FAO, Dumelow T, Machado FLA, de Araujo AEP. Giant magnetoimpedance in FeAg granular alloys. Appl Phys Lett 2002;80:2532–4.

[321] Nie HB, Pakhomov AB, Yan X, Zhang XX, Knobel M. Giant magnetoimpedance in crystalline Mumetal. Solid State Commun 1999;112:285–9.

[322] Fraga GLF, Pureur P, Brandao DE. Spontaneous magnetoimpedance in the Heusler compounds Pd_2MnSn and Pd_2MnSb near the Curie temperature. Solid State Commun 2002;124:7–10.

[323] Mohri K, Uchiyama T, Panina PV. Recent advances of micro magnetic sensors and sensing application. Sens Acta A 1997;59:1–8.

[324] Atkinson D, Squire PT, Maylin MG, Gore J. An integrating magnetic sensor based on the giant magneto-impedance effect. Sens Acta A 2000;81:82–5.

[325] Nishibe Y, Ohta N. Thin film magnetic field sensor utilizing magnetoimpedance effect. R&D Rev Toyota CRDL 2000;35:1–6.

[326] Kurlyandskaya GV, Garcia-Arribas A, Barabdiaran JM, Kisker E. Giant magnetoimpedance strip and coil sensors. Sens Acta A 2001;91:116–9.

[327] Mohri K, Uchiyama T, Shen LP, Cai CM, Panina PV, Honkura Y, et al. Amorphous wire and CMOS IC-based sensitive micromagnetic sensors utilizing magnetoimpedance (MI) and stress-impedance (SI) effects. IEEE Trans magn 2002;38:3063–8.

[328] Honkura Y. Development of amorphous wire type MI sensors for automobile use. J Magn Magn Mater 2002;249:375–7.

[329] Yabukami S, Mawatari H, Horikoshi N, Murayama Y, Ozawa T, Ishiyama K, et al. A design of highly sensitive GMI sensor. J Magn Magn Mater 2005;290–291:1318–21.

[330] Nesteruk K, Kuzminski M, Lachowicz HK. Novel magnetic field meter based on giant magnetoimpedance (GMI) effect. Sen Trans Mag 2006;65:515–20.

[331] Giouroudi I, Hauser H, Musiejovsky L, Steurer J. Giant magnetoimpedance sensor integrated in an oscillator system. J Appl Phys 2006;99:08D906:1–6:3.

[332] Alves F, Bensalah AD. New 1D-2D magnetic sensors for applied electromagnetic engineering. J Mater Proc Tech 2007;181:194–8.

[333] Hauser H, Steindl R, Hausleitner C, Pohl A, Nicolics J. Wirelessly interrogable magnetic field sensor utilizing giant magnetoimpedance effect and surface acoustic wave devices. IEEE Instrum Meas 2000;49:648–52.

[334] Pohl A. A review of wireless SAW sensors. IEEE Trans Ultrason Ferroelectr Frequency Control 2000;47:317–32.

[335] Valensuela R, Freijo JJ, Salcedo A, Vazquez M, Hernando A. A miniature dc current sensor based on magnetoimpedance. J Appl Phys 1997;81:4301–3.

[336] Malátek M, Ripka P, Kraus L. Double-core GMI current sensor. IEEE Trans Magn 2005;41:3703–5.

[337] Phan MH, Peng HX, Dung NV, Nghi NH. A new class of GMI current sensor for ac and dc measurements [unpublished].

[338] Tejedor M, Hernando B, Sanchez ML, Prida VM, Vazquez M. Magneto-impedance effect in amorphous ribbons for stress sensor application. Sens Acta A 2001;81:98–101.

[339] Bowles A, Gore J, Tomka G. A new, low-cost, stress sensor for battery-free wireless sensor applications. Proc SPIE Int Soc Opt Eng 2005;5765:1104–11.

[340] Valensuela R, Vazquez M, Hernando A. A position sensor based on magnetoimpedance. J Appl Phys 1996;79:6549–91.

[341] http://www.snpc.org.cn.

[342] http://www.aichi-mi.com/.

[343] Delooze P, Panina LV, Mapps DJ, Ueno K, Sano H. Effect of transverse magnetic field on thin film magnetoimpedance and application to magnetic recording. J Magn Magn Mater 2004;272–276:2266–8.

[344] Uchiyawa T, Mohri K, Itho H, Nakashima K, Ohuchi J, Sudo Y. Car traffic monitoring system using MI sensor built-in disk set on the road. IEEE Trans Magn 2000;36:3670–2.

[345] Kim DJ, Park DA, Hong JH. Nondestructive evaluation of reactor pressure vessel steels using the giant magnetoimpedance sensor. J Appl Phys 2002;91:7421–3.

[346] Kurlyandskaya GV, Sanchez ML, Hernando B, Prida VM, Gorria P, Tejedor M. Giant-magnetoimpedance-based sensitive element as a model for biosensors. Appl Phys Lett 2003;82:3053–5.

[347] Kurlyandskaya GV, Miyar VF. Surface modified amorphous ribbon based magnetoimpedance biosensor. Biosensors Bioelectr 2007;22:2341–5.

[348] Totsu K, Haga Y, Esashi M. Three-axis magnetoimpedance effect sensor system for detecting position and orientation of catheter tip. Sens Acta A 2004;111:304–9.

[349] Chiriac H, Tibu M, Moga AE, Herea DD. Magnetic GMI sensor for detection of biomolecules. J Magn Magn Mater 2005;293:671–3.

[350] http://www.patentstorm.us/patents/6433533.html.

[351] Uchiyawa T, Meydan T. GMI torque sensor module with FM transmitter. J Optoelectr Adv Mater 2004;6:689–94.

[352] Shen LP, Mohri K, Uchiyawa T, Honkura Y. Sensitive acceleration sensor using amorphous wire SI element combined with CMOS IC multivibrator for environmental sensing. IEEE Trans Magn 2000;36:3667–9.

[353] Makhnovskiy DP, Panina LV, Mapps J, Sarychev AK. Effect of transition layers on the electromagnetic properties of composites containing conducting fibres. Phys Rev B 2001;64:134205:1–134205:12.

[354] Makhnovskiy DP, Panina LV. Field dependent permittivity of composite materials containing ferromagnetic wires. J Appl Phys 2003;93:4120–9.

[355] Panina LV, Sandacci SI, Makhnovskiy DP. Stress effect on magnetoimpedance in amorphous wires at gigahertz frequencies and application to stress-tunable microwave composite materials. J Appl Phys 2005;97:013701:1–1:6.

[356] Phan MH, Peng HX, Wisnom MR, Mellor PH. Optimizing the nanostructure of magnetic microwires for multifunctional macrocomposites, 48th AIAA/ASME/ASCE/AHS/ASC Structures, Structural Dynamics, and Materials Conference, 23–26 April 2007, Honolulu, Hawaii, AIAA 2007–2032:1–7.